

AD 725159

UNCLASSIFIED

DASA 2608

21 May 1971

# HOLOGRAPHIC STUDY OF WAVE PROPAGATION IN GRANITE

## FINAL REPORT

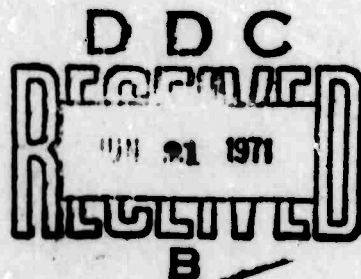
This work was supported by the Advanced Research Projects Agency  
under ARPA Order No. 1468

R. Aprahamian  
J. L. Jacoby  
J. D. O'Keefe  
T. J. Ahrens

Reproduced by  
NATIONAL TECHNICAL  
INFORMATION SERVICE  
Springfield, VA 22151

HEADQUARTERS  
DEFENSE ATOMIC SUPPORT AGENCY  
WASHINGTON, D.C. 20305

TRW Systems Group  
DASA 01-69-C-0152



Approved for public release; distribution unlimited

UNCLASSIFIED

132

**BEST  
AVAILABLE COPY**

## DOCUMENT CONTROL DATA - R &amp; D

Security classification of title, body of abstract and indexing annotation must be entered when the report is received.

SPONSORING ACTIVITY (Corporate author)

20. REPORT NUMBER (DA Form 101)

TRW Systems Group

Unclassified

One Space Park

21. GROUP

Redondo Beach, California 90278

REPORT TITLE

Holographic Study of Wave Propagation in Granite

4. EXTENT OF NOTES (Type of report and inclusive dates)

Final Report, 4 June 1969 ~ 31 December 1970

5. AUTHOR(S) (First name, middle initial, last name)

Robert Aprahamian

Thomas J. Ahrens

Jerold J. Jacoby

John D. O'Keefe

6. REPORT DATE

31 December 1970

7a. TOTAL NO. OF PAGES

131

31

7b. PROJECT OR GRANT NO.

DASA 01-69-C-0152

8. ORIGINATOR'S REPORT NUMBER

70-4341/386

9. PROJECTING NO.

9b. OTHER REPORT NUMBER (Any other numbers that may be associated with this report)

DASA 2608

Program Element Code: 62701D

10. APPROVAL STATEMENT

Approved for public release; distribution unlimited.

11. COMMENTARY NOTES

12. SPONSORING MILITARY ACTIVITY

Director

Defense Atomic Support Agency

Washington, D.C. 20305

Three techniques of holographic interferometry were developed to study the response of geological materials to propagating stress waves. Two of these techniques, laser-beam interferometry and double-exposure interferometry, were found effective when applied to studying small-amplitude wave propagation. The third technique, a form of time-average holographic interferometry, which produced fringes relating to velocities, was employed when studying higher stress levels (up to 30 kb). Low amplitude stress waves were generated by pendulum impacts; a gas gun was used to obtain higher stress levels. A complete description of each technique is given herein, together with a comparison of experimental results (using Westerly granite) and theoretical predictions.

Unclassified

Security Classification

14	KEY WORDS	LINK A		LINK B		LINK C	
		ROLE	WT	ROLE	WT	ROLE	WT
	Holography Holographic Interferometry Westerly Granite Equations of State Constitutive Relations						

Unclassified

Security Classification

UNCLASSIFIED

DASA 2608

21 May 1971

# HOLOGRAPHIC STUDY OF WAVE PROPAGATION IN GRANITE

## FINAL REPORT

This work was supported by the Advanced Research Projects Agency  
under ARPA Order No. 1468

R. Aprahamian  
J. L. Jacoby  
J. D. O'Keefe  
T. J. Ahrens

HEADQUARTERS  
DEFENSE ATOMIC SUPPORT AGENCY  
WASHINGTON, D.C. 20305

TRW Systems Group  
DASA 01-69-C-0152

Approved for public release; distribution unlimited

UNCLASSIFIED

# ABSTRACT

Three techniques of holographic interferometry were developed to study the response of geological materials to propagating stress waves. Two of these techniques, stored-beam interferometry and double-exposure interferometry, were found effective when applied to studying small-amplitude wave propagation. The third technique, a form of time-average holographic interferometry (which produces fringes relating to velocities), was employed when studying higher stress levels (up to 30 kb). Low amplitude stress waves were generated by pendulum impacts; a gas gun was used to obtain higher stress levels. A complete description of each technique is given herein, together with a comparison of experimental results (using Westerly granite) and theoretical predictions.

## FOREWORD

This report was prepared by the Applied Mechanics Laboratory of TRW Systems Group, Redondo Beach, California under Defense Atomic Support Agency Contract DASA-01-69-C-0152. Mr. C. B. McFarland served as the contract monitor for DASA. Program manager at TRW Systems was Mr. R. Aprahamian. Technical support was contributed by Mr. J. L. Jacoby, Mr. J. D. O'Keefe, Dr. D. A. Evensen and Mr. J. E. Wright. Dr. T. J. Ahrens of the California Institute of Technology served as consultant.

Initially the research carried out on this program was directed toward developing holographic instrumentation and techniques which could be used to measure the effects of cracks and porosity in geological materials on stress wave propagation. Several promising techniques were uncovered in the initial months of this investigation. As our work progressed and as a result of discussions with the DASA technical monitor, our research objectives developed toward applying our holographic instrumentation to measuring the constitutive properties of Westerly granite. This report summarizes the results of both the techniques development phase and the equation of state measurement phase of the present program.

# TABLE OF CONTENTS

	Page
ABSTRACT . . . . .	1
FOREWORD . . . . .	11
LIST OF ILLUSTRATIONS. . . . .	v
LIST OF TABLES . . . . .	viii
1.0 INTRODUCTION. . . . .	1
2.0 MATERIAL DESCRIPTION. . . . .	3
3.0 PHENOMENOLOGY OF IMPACTS. . . . .	5
3.1 <u>Mechanism of Impact</u> . . . . .	5
3.2 <u>Plane Stress Regime</u> . . . . .	9
3.3 <u>Plane Strain Regime</u> . . . . .	17
4.0 LOW AMPLITUDE ELASTIC WAVE PROPAGATION STUDIES IN THE PLANE STRESS REGIMES. . . . .	23
4.1 <u>Experiments Employing Double-Exposure Holographic Interferometry (Longitudinal Waves in a Rod</u> . . . . .	23
4.1.1 <u>Experimental Technique.</u> . . . . .	24
4.1.2 <u>Test Procedure and Results.</u> . . . . .	30
4.2 <u>Measurement of the Time-Dependent Displacement of the Free End of an Impacted Rod</u> . . . . .	38
4.2.1 <u>Experimental Technique.</u> . . . . .	39
4.2.2 <u>Longitudinal End Displacement (Theoretical Results).</u> . . . . .	42
4.2.3 <u>Experimental Results.</u> . . . . .	47
4.2.4 <u>Evaluation of Stored Beam Interferometry.</u> . . . .	50
5.0 LARGE AMPLITUDE STRESS WAVE PROPAGATION STUDY . . . . .	53
5.1 <u>Experimental Method</u> . . . . .	53
5.1.1 <u>Constraints of Wedge and Flyer Plate Geometries.</u> . . . . .	56
5.1.1.1 <u>Catch-up Waves.</u> . . . . .	56
5.1.1.2 <u>Lateral Release Waves</u> . . . . .	59
5.1.2 <u>Experimental Facilities</u> . . . . .	61
5.1.3 <u>Target Alignment.</u> . . . . .	63
5.1.4 <u>Instrumentation</u> . . . . .	67
5.1.5 <u>Holographic Technique</u> . . . . .	72
5.2 <u>Determination of the Shock Parameters from the Experimental Observables.</u> . . . . .	73
5.3 <u>Experimental Results.</u> . . . . .	81



5.4	<u>Determination of the Sonic Velocity in the Shocked Material by the Use of Lateral Release Waves. . . . .</u>	93
6.0	SUMMARY AND CONCLUSIONS . . . . .	96
7.0	REFERENCES. . . . .	99
	APPENDIX A . . . . .	102
	APPENDIX B . . . . .	117

# LIST OF ILLUSTRATIONS

	Page
1. Westerly granite specimens used in this investigation. . . .	4
2. Test setup to measure Poisson's ratio and Young's Modulus of Westerly granite. . . . .	5
3. Semi-infinite rod with an applied stress . . . . .	12
4. Longitudinal and radial displacements as a function of distance along the rod . . . . .	17
5. Evolution of a compressional stress pulse into a shock wave.	19
6. Schematic representation of a pulsed ruby laser. . . . .	26
7. Experimental setup used to make double-exposure holographic interferograms of a rod supporting a stress pulse. . . . .	30
8. Longitudinal and radial displacements as a function of distance along the rod . . . . .	32
9. Holographic interferogram of a stress pulse propagating in an aluminum rod . . . . .	34
10. Stress pulse measured by a manganin gauge (pendulum impact).	35
11. Double-exposure holograms showing stress waves in a granite rod. . . . .	38
12. Schematic of stored beam interferometry test set-up. . . . .	41
13. Granite cylinder and spherical ballistic pendulum used to develop the stored-beam interferometry technique . . . . .	42
14. Rectangular stress pulse . . . . .	43
15. Oscilloscope traces of photocell outputs during spherical pendulum-aluminum cylinder tests . . . . .	44
16. Superposition of two step functions. . . . .	43
17. Reflection of pulse at the right end of the bar. . . . .	46
18. End displacement, $\xi$ , for a rectangular compression pulse . .	47

19.	Oscilloscope record of spherical pendulum granite cylinder impact. . . . .	49
20.	Displacement time history of the free end of the granite cylinder as determined from the oscilloscope trace shown in Figure 19 . . . . .	49
21.	Oscilloscope record of spherical pendulum-granite cylinder impact. . . . .	52
22.	Displacement time history of the free end of the granite cylinder as determined from oscilloscope record shown in Figure 21 . . . . .	52
23.	Wedge configuration used to holographically determine a material's shock properties . . . . .	56
24.	X-T diagram of the impact of a flyer plate on a target halfspace . . . . .	58
25.	Geometric construction of the lateral release waves . . . . .	61
26.	Lexan projectile and granite impactor . . . . .	63
27a.	Gas gun and vacuum chamber. . . . .	64
27b.	Holographic apparatus . . . . .	65
28.	Wedge-shaped granite target . . . . .	67
29.	"Exploded" view of impact configuration . . . . .	68
30.	Capacitor discharge circuit used for trigger. . . . .	70
31.	Launch tube extension with four trigger stations. . . . .	70
32.	Alignment assembly for trigger stations . . . . .	72
33.	Tilt pin coding circuit . . . . .	72
34.	Wedge Geometry. . . . .	75
35.	Tilt pin configuration. . . . .	76
36.	Vertical section of wedge through point A . . . . .	76
37.	Horizontal section of wedge through point A . . . . .	79
38.	Geometry of projectile and shock front trajectories . . . . .	79

39.	Single-exposure hologram taken in experiment 13-2 showing a granite-on-granite impact. . . . .	85
40.	Reconstruction of a holographic image of an unstressed wedge. . . . .	85
41.	Side view (normal to wedge axis) of the wave positions in granite in experiment 13-2 . . . . .	87
42.	Hugoniot for Westerly granite. . . . .	89
43.	Interferogram of a stress pulse propagating in a granite wedge. . . . .	90
44.	Interferogram of a stress pulse propagating in a granite wedge. . . . .	91
45.	Shock and release wave positions in a stressed aluminum wedge. . . . .	95
A.1.	Typical experimental setup to make holograms of optically opaque objects . . . . .	102
A.2.	Photograph of a small area of a hologram magnified 1000 times original . . . . .	105
A.3.	Image retrieval process. . . . .	106
A.4.	Phase change of light due to the motion of the object. . . . .	108
A.5.	Three double-exposure holographic interferograms of a transverse wave propagating in a prismatic beam. . . . .	112
A.6.	Intensity of the holographically reconstructed image taken of a moving object . . . . .	116
B.1.	Changing the direction of a light beam with a Pockels cell - calcite prism combination. . . . .	118
B.2.	One possible arrangement to make two interferograms of an event in rapid succession. . . . .	118
B.3.	Reconstruction of two interferograms made on the same hologram . . . . .	119

LIST OF TABLES

	Page
I. Longitudinal deformation data. . . . .	33
II. Radial deformation data. . . . .	33
III. Results of granite impact experiments. . . . .	84
IV. Experimental parameters. . . . .	94

**BLANK PAGE**

## 1.0 INTRODUCTION

The equation of state of the geological material in which an underground explosion is detonated affects the stress wave which is propagated out to teleseismic distances. Knowledge of the equation of state of the medium permits theoretical calculation of stress wave profiles and is thus important in distinguishing underground tests from naturally occurring earthquakes. In addition to the discrimination problem, ultimate understanding of the interactive effects of the explosive configuration and various surrounding media will provide the quantitative basis for placing bounds on test parameters when events are monitored at teleseismic distances.

To properly describe the wave propagation phenomena, usually by means of finite difference techniques, the medium in which the waves propagate must be correctly modeled. Material models, or constitutive relations, for geological materials are difficult to obtain. For most geological materials, the combined effects of inhomogeneity, stress relaxation, phase changes, strain-rate effects and porosity give rise to a complex mechanical response. Even for the simplest geological materials, constructing a complete constitutive relation from  $10^{12}$  to  $1 \text{ dyne/cm}^2$  stress levels (12 orders of magnitude) presents a challenging problem. The present program has been concerned with developing and applying holographic techniques in obtaining equation of state data in the 0.1 to 30 kbar stress range.

When studying a material undergoing dynamic loading and subsequent unloading, the problem of describing the constitutive relation naturally divides itself into the following two phases:

- (1) describing the state achieved during what is usually the shock compression. (This often amounts to describing the material's Hugoniot curve.)

- (2) description of the state achieved during unloading which involves determining both the release adiabats, and most importantly, prescribing the rheological behavior, i.e., the relationship between principal stresses and strains, of the medium after it has undergone an initial finite, high-strain-rate deformation.

As in conventional shock wave experiments, states along the Hugoniot, in the 30 kbar range were obtained by measuring the shock velocity and particle velocity and applying the Rankine-Hugoniot jump conditions. This determines the thermodynamic state variables: pressure, density and specific internal energy. These experiments involved a form of time-average holography and are described in Section 5. The rarefaction wave or unloading velocity in Westerly granite was also studied in these experiments. Loading and unloading states in the 0.1 kbar range were measured by the relatively new methods of stored-beam and double-exposure holographic interferometry. The techniques and results are discussed in Section 4. Initially, 2024 aluminum and then Westerly granite were studied under this program. These materials were chosen so as to obtain results which would overlap with previous experimental work and hence establish the credibility of the data obtained with our new techniques.

The objective of this program was to develop instrumentation to record holographically the profiles of propagating stress waves in granite specimens. Three techniques of holographic interferometry were developed to meet this objective, viz., stored-beam, double-exposure and a form of time averaged interferometry (which produces fringes relating to velocities).



These techniques were successfully applied to obtain data, such as

- o The axial and radial deformation of a cylinder impacted at one end by a spherical pendulum
- o The displacement-time history of the free-end of a cylinder impacted at one end by a spherical pendulum
- o Hugoniot data points, and
- o Lateral release wave and catch-up wave velocities in dynamically stressed granite.

while still retaining the noncontacting advantage of the techniques. In each instance, the data obtained by these techniques compared favorably with data published in the literature.

In the course of this study it was found that data can be generated by the velocity interferometric technique which cannot be attained by any other method. For example, the catch-up wave and lateral release wave velocities can be measured for a given event allowing the sonic velocity in two different directions to be measured simultaneously. From these data, the anisotropy in the sonic velocity induced by the uniaxial straining of the shock wave can be determined. This is possible because of the full field recording capability of holography.

The development of the holographic techniques achieved a major objective of this phase of the study. Further work should be done to exploit the capabilities of these techniques and to generate more extensive and accurate data on geologic materials of interest.

## 2.0 MATERIAL DESCRIPTION

Westerly granite was chosen as the material used in this study because some of its properties are relatively well known. Data published in the literature serves as a useful guide in evaluating the new holographic techniques. Specimens of granite which were mined from a quarry in Westerly, Rhode Island, were obtained from the Bottinelli Granite Company, New London, Connecticut. Forty cylinders measuring 2" in diameter with a minimum length of 10" were received in a rough core cut state (Figure 1). Cutting and centerless grinding of the specimens was later performed by Blanchard Masters Grinding Corporation of Hawthorne, California.



Figure 1: Westerly granite specimens used in this investigation

Before using the granite in experiments, a number of tests were made to determine its static properties. After machining, a representative sample of granite was measured geometrically and weighed. The density,  $\rho$ ,

was found to be  $2.616 \text{ gm/cm}^3$ . Poisson's ratio,  $\nu$ , and Young's Modulus,  $E$ , of a representative sample was measured using a uniaxial compression test. Foil strain gauges (Figure 2) were used to measure longitudinal and traverse strain produced upon compressing the sample in a Baldwin Universal Testing Machine. The stress was obtained from the force gauge on the machine and is known to a precision of  $\pm 0.33\%$ . For the sample tested, it was found that the average elastic constants over the longitudinal stress range from 0 to 1 kbar were:

$$\nu = 0.23 \pm .005$$

$$E = 5.0 \pm .02 \times 10^{11} \text{ dyne/cm}^2$$

Corresponding values tabulated from the Handbook of Physical Constants<sup>1</sup> vary from .065 to .271 for Poisson's ratio and from  $3.99 \times 10^{11}$  to  $7.05 \times 10^{11}$  dynes/cm<sup>2</sup> for Young's Modulus.



Figure 2: Test setup to measure Poisson's ratio and Young's Modulus of Westerly granite

### 3.0 PHENOMENOLOGY OF IMPACTS

Wave propagation in cylindrical bars is a long standing problem of both academic and great practical interest. The first analytical solutions to the problem of elastic wave propagation in an infinite bar were obtained by Pochhammer<sup>2</sup> in 1876 and independently by Chree<sup>3</sup> in 1889. In 1941, Bancroft<sup>4</sup> obtained numerical values for the Pochhammer-Chree frequency equation. Work has continued up to the present time in obtaining solutions to the exact equations of motion.<sup>5,6</sup> The analytical solutions which were obtained by these early researchers are valid only asymptotically, i.e., on the order of ten bar diameters from point of impact, and are of little value for the determination of the initial impact pulse. Numerical codes have been developed which will integrate the exact equations of motion for both elastic and non-elastic media.<sup>7,8</sup> Few numerical solutions have been obtained because of the cost of long running times of multi-dimensional codes. In the following sections, the physics of impact of identical elastic, purely plastic and elastic-plastic bars will be presented and the derivation of constitutive relations will be discussed.

#### 3.1 Mechanism of Impact

The simplest case of impact is the symmetrical impact of two identical perfectly elastic cylinders.<sup>7</sup> Upon impact, two plane elastic shock waves propagate from the plane of impact into the two rods. (The shock front here is defined as a finite step in the stress magnitude). The shocked material is in a state of uniaxial strain in the axial direction, i.e., particle motion in the axial direction only, and triaxial stress. Since the surface of the cylinder is unconstrained, those particles near the

surface which have been engulfed by the shock front are accelerated in the radial direction (Poisson's effect). It is this lateral inertia which causes the complex spatial and temporal response of the rod to the simple step loading of the impact.<sup>9</sup> The release waves associated with this radial acceleration of particles will have both shear and dilatational components. The state of uniaxial strain in the elastic shock has a duration determined by the time it takes dilatational elastic waves excited by the passage of the shock across the surface to diminish the thickness of the shock front to infinitesimal proportions. This occurs at an axial position on the order of several bar diameters. From this point on, the wave evolves from the previous uniaxial strain state to a strain state characterizing a plane stress wave. Oscillations occur behind the stress wave front due to multiple reflections from the bar surface of waves that were excited by the initial passage of the shock. Elastic waves in bars propagate dispersively with the higher frequency waves propagating more slowly than the lower. This causes the sharp fronted elastic shock in the propagation to spread out and asymptotically approach to profile associated with the lowest order mode that can propagate.

The symmetrical impact of two identical, perfectly-plastic bars would be the next order of complexity. Here, as opposed to the elastic case, the velocity of propagation of the wave is not constant, but depends on the changing slope of the stress-strain curve. The greater the slope the higher the velocity of propagation.<sup>10</sup> The stress-strain curve for uniaxial strain is such that  $\partial^2 \sigma / \partial \epsilon^2 > 0$ . This means that higher velocities of propagation are associated with larger strains, and stable shock waves

will thus form. The stress-strain curve for uniaxial stress is such that  $\partial^2 \sigma / \partial \epsilon^2 < 0$ . Here the larger the strain, the lower the velocity of propagation, and hence the shock waves are not stable and spread out in time.

The case where the bars are elastic-perfectly plastic, as the name implies, combines some of the aspects of both the elastic and perfectly-plastic cases. However, there are considerable complications introduced by the interaction and coupling of the elastic and plastic wave systems.<sup>8,10</sup> The stress-strain curve for plane-stress is linear up to the yield point and from then on  $\partial^2 \sigma / \partial \epsilon^2 < 0$ . At the intersection point of the elastic and elastic-plastic regime, the slope of the stress-strain curve decreases discontinuously. This gives rise to both an elastic and plastic wave propagation for states at stresses above the intersection point. This implies that the elastic wave velocity is greater than the plastic wave velocity. The stress-strain curve for uniaxial strain is also linear up to the yield point but at higher stresses,  $\partial^2 \sigma / \partial \epsilon^2 > 0$ . At some point (Rayleigh Point) on the plastic portion of the plane strain curve, the slope of the line from the initial to final state will be equal to the slope of the elastic regime. Below this point, plastic waves will propagate with velocities less than the elastic waves and above that point plastic waves will propagate with velocities that are greater than the elastic waves. The condition that  $\partial^2 \sigma / \partial \epsilon^2 > 0$  satisfied by the stress-strain curve will allow the formation of stable plastic shocks; and an initially sharp fronted stress pulse can break up into an elastic and a plastic wave depending on the initial stress magnitudes. For very low

velocities of impact, the stresses will be elastic and the waves will propagate in the manner previously discussed. For very high velocities, the initial uniaxial plastic shock will propagate in a stable manner with a velocity exceeding the elastic longitudinal velocity. The uniaxial strain wave will propagate until release waves having both elastic and plastic components overtake and attenuate it. As the plastic wave is attenuated, a point will be reached where the elastic wave velocity exceeds the local plastic wave velocity and the wave will become unstable and break up into an elastic and plastic portion.

For propagation in a finite diameter rod, the plastic wave will deviate from a state of plane strain at an axial position on the order of one bar diameter, while the elastic portion of the wave will be in a state of plane strain for several bar diameters. For intermediate velocities of impact the initial uniaxial plastic shock will be unstable and break up into plastic and elastic waves. The attenuation of these waves will proceed as before. Both the elastic and plastic uniaxial strain waves will evolve into plane stress waves.

Some of the other major material properties that can complicate the bar response are strain rate effects, phase changes and porosity. One of the manifestations of strain rate is a variation in the amplitude of precursor elastic waves. Phase changes can cause the initial uniaxial shock to become unstable and break up into two or more shocks. This would be especially important in rocks whose mineralogical constituents may have high pressure polymorphs. Porosity can greatly effect the initial uniaxial shock and the partitioning of the thermal and lattice components of energy in the wave.

At this point it should be apparent that there are two spatial regimes in the bar in which the wave systems induced are simple enough that surface measurements can yield information as to the constitutive properties of the bar material. These are the plane strain regime near the impact end and the plane stress regime on the order of ten bar radii from the impact end.

### 3.2 Plane Stress Regime

The plane stress regime has long been used in the measure of material response. An enormous number of experiments have been performed on metals, simple materials and rocks.<sup>9,11,12,13</sup> Simultaneous measurement of any two of the following, axial strain, axial particle velocity, axial stress or wave velocity suffices to determine a point on the material's stress-strain curve. The planarity of the impact has little effect in the plane stress region. A non-planarity in the impact serves to excite higher modes of the rod. Since, however, the rod is dispersive and the higher modes have lower propagation velocities, the wave front is dominated by the lowest mode. The one-dimensional uniaxial stress non-linear wave propagation theory of G. I. Taylor, T. von Karman and K. A. Rakhatulin provides interrelationships between the above variables.<sup>11</sup> The explicit applications of one-dimensional stress propagation in an elastic rod to measuring constitutive properties is discussed below.

To understand longitudinal wave propagation in a rod, the simplest theory to apply is based upon the assumption of plane, elastic waves. This theory assumes that plane cross sections remain plane, and that only axial stresses are present, being uniformly distributed across the



cross-section. The equations comprising this theory are

$$\frac{\partial \sigma_x}{\partial x} = \rho \frac{\partial v_x}{\partial t} \quad \text{(Equation of motion)} \quad (1)$$

$$\frac{\partial v_x}{\partial x} = \frac{\partial \epsilon_x}{\partial t} \quad \text{(Equation of continuity)} \quad (2)$$

$$\sigma_x = E \epsilon_x \quad \text{(Constitutive behavior)} \quad (3)$$

In these equations, the following definitions apply:

- $\sigma_x$  = Axial Stress
- $\epsilon_x$  = Axial Strain,  $\epsilon_x = \frac{\partial u_x}{\partial x}$
- $u_x$  = Longitudinal Displacement
- $x$  = Axial Coordinate
- $v_x$  = Axial Particle Velocity
- $t$  = Time
- $E$  = Modulus of Elasticity
- $\rho$  = Mass Density

The preceding equations can be combined into single wave equations such as

$$\frac{\partial^2 \sigma_x}{\partial x^2} = \frac{1}{c_o^2} \frac{\partial^2 \sigma_x}{\partial t^2} \quad (4)$$

or

$$\frac{\partial^2 u_x}{\partial x^2} = \frac{1}{c_o^2} \frac{\partial^2 u_x}{\partial t^2} \quad (5)$$

where the wave speed,  $c_0 = \sqrt{\frac{E}{\rho}}$ , is the so-called "bar velocity". The limitations of this elementary theory have been discussed extensively by Davies (Ref. 9). Davies points out that the elementary theory is very nearly correct when the duration of the pulse is long compared with the time required for a wavefront to move across the diameter of the rod.

Consider a circular rod of radius  $a$ , which is subjected to a stress-time history

$$\sigma_x \begin{cases} = \sigma_{x_0} \sin \frac{\pi t}{T} & 0 \leq t \leq T \\ = 0 & T \leq t < \infty \end{cases} \tag{6}$$

at the end  $x = 0$ . (See Figure 3)

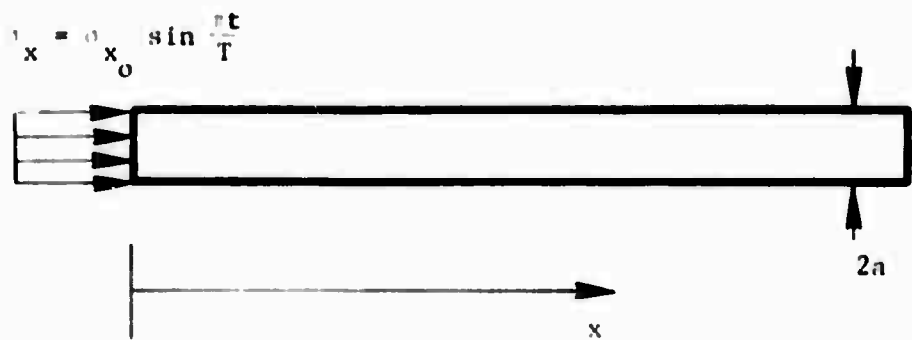


Figure 3: Semi-infinite rod with an applied stress

The general solution of equation (4) is of the form

$$\sigma_x(x,t) = F(x - c_0 t) + G(x + c_0 t) \quad (7)$$

which can be combined with (6) to give

$$\sigma_x(x,t) = \sigma_{x_0} \sin \frac{\pi}{L} (c_0 t - x) \quad (8)$$

$$\text{For } 0 \leq c_0 t - x \leq c_0 T$$

$$\sigma_x(x,t) = 0 \quad \text{For } \begin{cases} x \geq c_0 t \\ x \leq c_0 (t - T) \end{cases}$$

In equation (8), the pulse length is  $L = c_0 T$ , where  $T$  is the pulse duration

It should be noted that  $\sigma_{x_0}$  is the maximum value of the applied stress

and also is the maximum stress in the rod.

To compute the longitudinal displacements, we have

$$\epsilon_x = \frac{\partial u_x}{\partial x} = \frac{\sigma_x}{E} \quad (\text{From Hooke's Law})$$

or

$$\frac{\partial u_x}{\partial x} = \frac{\sigma_{x_0}}{E} \sin \frac{\pi}{L} (c_0 t - x) \quad (9)$$

By integration, we have

$$\int_x^{x=c_0 t} \frac{\partial u_x}{\partial x} dx = u_x \Big|_{x=c_0 t} - u_x(x,t) \quad (10)$$

where  $u_x = 0$ , at  $x = c_0 t$  (the wavefront)

Using equation (9) in (10) gives

$$u_x(x,t) = - \int_x^{x=c_0 t} \frac{\sigma_{x_0}}{E} \sin \frac{\pi}{L} (c_0 t - x) dx$$

$$u_x(x,t) = - \left( \frac{\sigma_{x_0}}{E} \right) \left( \frac{L}{\pi} \right) \cos \frac{\pi}{L} (c_0 t - x) \Big|_x^{x=c_0 t} \quad (11)$$

$$u_x(x,t) = - \left( \frac{\sigma_{x_0}}{E} \right) \left( \frac{L}{\pi} \right) \left[ \cos \frac{\pi}{L} (c_0 t - x) - 1 \right]$$

For  $0 \leq x - c_0 t \leq c_0 T$

At time  $t = T$ , (when the pulse has fully entered the rod) we have

$$u_x(x,t) = - \left( \frac{\sigma_{x_0}}{E} \right) \left( \frac{L}{\pi} \right) \left[ \cos \frac{\pi}{L} (c_0 t - x) - 1 \right] \quad (12)$$

Expanding equation (12) gives

$$u_x(x,t) = - \left( \frac{\sigma_{x_0}}{E} \right) \left( \frac{L}{\pi} \right) \left[ \cos \frac{\pi x}{L} + 1 \right] \quad (13)$$

which has a maximum value of

$$u_x(0,T) = - \left( \frac{\sigma_{x_0}}{E} \right) \left( \frac{2L}{\pi} \right), \text{ where } \sigma_{x_0} < 0$$

Similarly, the radial displacement on the surface can be calculated from:

$$u_r = \text{Radial Displacement} = - \nu \frac{\sigma_x}{E} a \quad (14)$$

where  $\nu$  is Poisson's ratio. At time  $t = T$ , we have

$$\begin{aligned} u_r &= -\nu a \left( \frac{\sigma_{x_0}}{E} \right) \sin \frac{\pi}{L} (c_0 T - x) \\ u_r &= -\nu a \left( \frac{\sigma_{x_0}}{E} \right) \sin \frac{\pi x}{L} \end{aligned} \quad (15)$$

where  $a$  is the radius of the circular rod. The maximum radial displacement is given by

$$(u_r)_{\max} = \nu a \left( \frac{\sigma_{x_0}}{E} \right), \text{ where } \sigma_{x_0} < 0$$

The ratio of the maximum radial displacement to the maximum longitudinal displacement is

$$R = \frac{\nu a}{L} \left( \frac{\pi}{2} \right) \text{ at time } t = T$$

As an example of these calculations, consider the case of an aluminum rod, with an input pulse of 60  $\mu\text{sec}$  duration and an amplitude of 1560 psi ( $1.08 \times 10^8 \text{ dyne/cm}^2$ ) (compression). Then we have

$$c_0 = \sqrt{\frac{E}{\rho}} = .1965 \text{ in}/\mu\text{sec} = 0.50 \text{ cm}/\mu\text{sec}$$

$$E = 9.3 \times 10^6 \text{ lb/in}^2 = 6.41 \times 10^{11} \text{ dynes/cm}^2, (\nu = 0.348)$$

$$L = c_0 T = .50 \text{ cm}/\mu\text{sec} \times 60 \mu\text{sec} = 30 \text{ cm}$$

$$a = 1 \text{ inch} = 2.54 \text{ cm (Bar Radius)}$$

$$u_x(x, T) = \left( \frac{1.08 \times 10^8}{6.41 \times 10^{11}} \right) \left( \frac{30 \text{ cm}}{\pi} \right) \left[ 1 + \cos \frac{\pi x}{30} \right]$$

For the longitudinal displacement

$$u_x(x,T) = (1.60 \times 10^{-3} \text{ cm}) (1 + \cos \frac{\pi x}{30}) \quad (16)$$

and the radial displacement is (from equation 15)

$$u_r(x,T) = (.348)(2.54) \left( \frac{1.08 \times 10^8}{6.41 \times 10^{11}} \right) \sin \frac{\pi x}{30} \quad (17)$$

$$u_r(x,T) = (.148 \times 10^{-3} \text{ cm}) (\sin \frac{\pi x}{30})$$

Equations (16) and (17) for the longitudinal and radial displacements as a function of  $x$  are shown graphically in Figure 4. The holographic measurement of the resultant strains from the impact at the end of a rod, such as described above, is discussed in the next section.

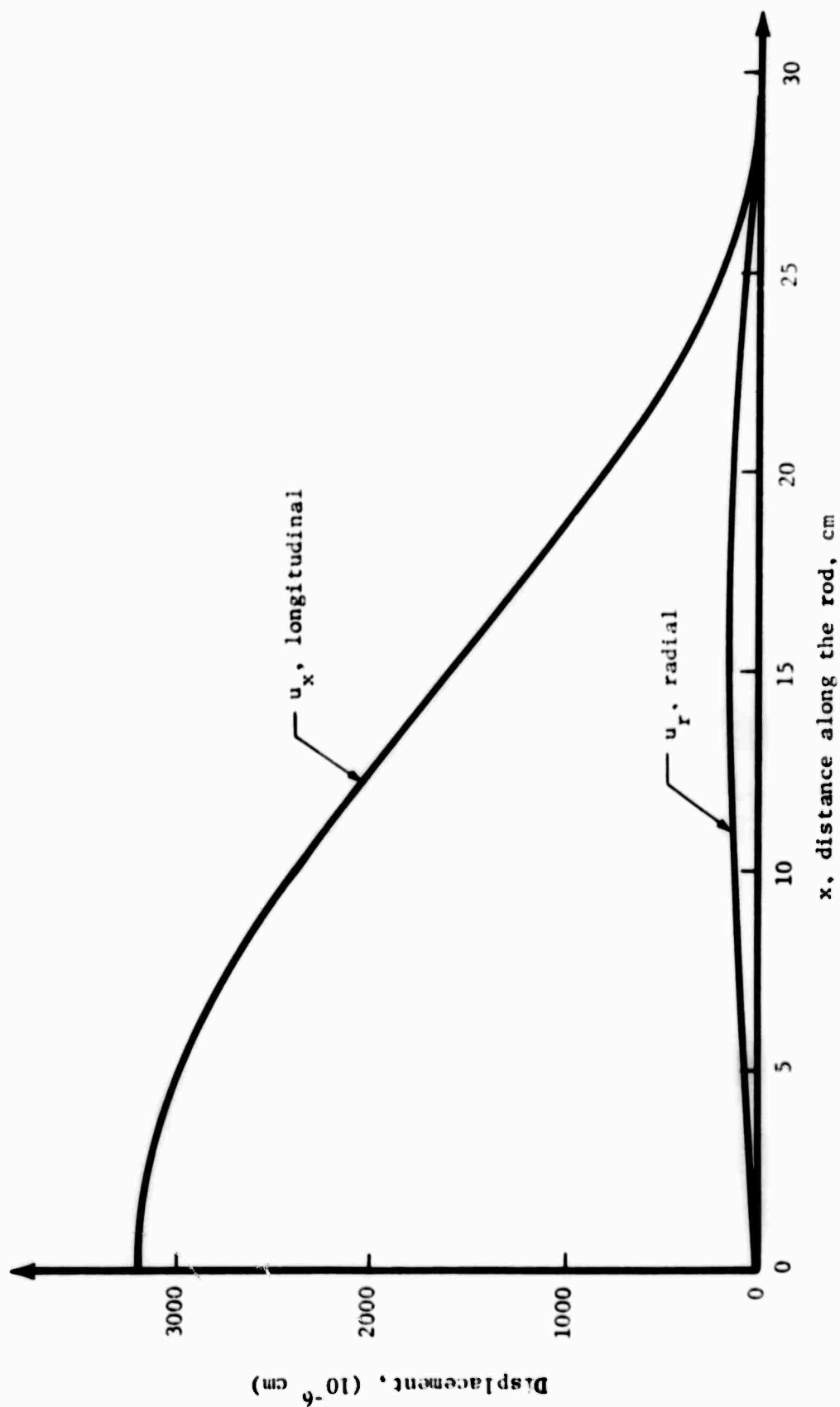


Figure 4: Longitudinal and radial displacements as a function of distance along the rod

### 3.3 Plane Strain Regime

Measurements in the plane strain regime are commonly made with impacts involving flat plates (i.e., length of bar much shorter than radius). Particle motions are measured on the surface opposite to that impacted. In this configuration, the shock wave is not affected by edge effects in the region of interest.

When a finite amplitude, one-dimensional strain wave propagates in a simple material, the wave form changes in time even in the absence of viscous or dissipative mechanisms.<sup>14</sup> This non-linear aspect of the wave propagation is a consequence of the increase of propagation velocity with stress wave amplitude. Thus, in a simple compressional pulse as illustrated in Figure 5, the high pressure elements of the wave propagate faster than the lower pressure elements so that the compression wave front steepens in time. Eventually these elements overtake one another and a discontinuity in a mathematical sense occurs. This discontinuity is called a shock wave. If viscous and dissipative effects are present, they are necessary but not sufficient to preclude the existence of the discontinuity.<sup>15</sup> The field equations<sup>16</sup>, a complicated set of non-linear partial differential equations along with appropriate constitutive functionals for the medium, describe the evolution of the stress wave. The occurrence of the shock wave, which appears as a multivalued region in state space, is predicted by the field equations, but its subsequent evolution must be described both by the field equations and the jump conditions.<sup>14</sup> The jump conditions for a normal discontinuity in the field variables yield the well known conservation of mass, momentum and energy.<sup>17</sup>



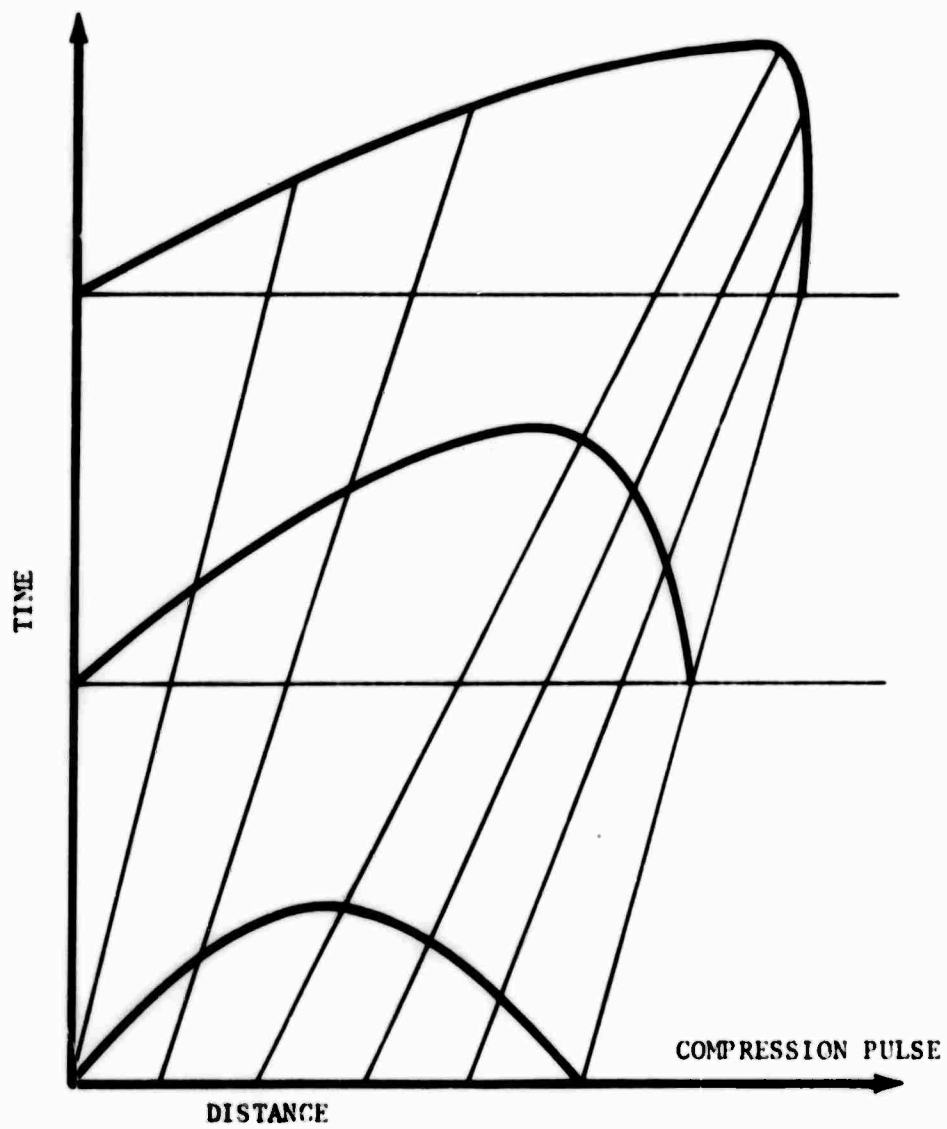


Figure 5: Evolution of a Compressional Stress Pulse into a Shock Wave

These are for a shock propagating into a medium at rest:

$$\rho(U - u) = \rho_0 U \quad (18)$$

$$P - P_0 = \rho_0 U^2 - \rho(U - u)^2 \quad (19)$$

$$1/2 \rho_0 U^3 + \rho_0 E_0 U + P_0 U = 1/2 \rho(U - u)^3 + \rho E(U - u) + P(U - u) \quad (20)$$

where  $\rho$ ,  $P$ ,  $E$ ,  $U$ , and  $u$  are the density, pressure, specific internal energy, shock velocity and particle velocity respectively on either side of the shock front. Using  $V = \frac{1}{\rho}$ , these equations can be manipulated to give the following,

$$P - P_0 = \rho_0 U u, \quad (21)$$

$$\frac{\rho_0}{\rho} = \frac{U - u}{U} \quad (22)$$

and

$$E - E_0 = \frac{1}{2}(P + P_0)(V_0 - V). \quad (23)$$

Equations (21), (22) and (23) are the Rankine-Hugoniot equations. In general, we concern ourselves with pressures  $P$  so large that the ambient pressure  $P_0$  can be ignored. Clearly then, equations (21) and (22) reveal that, for a material whose density  $\rho_0$  is known, measurements of the shock velocity,  $U$ , and the particle velocity,  $u$ , determine the peak pressure just behind the shock and the corresponding density,  $\rho$ . The curve generated by the corresponding values of  $P$  and  $V$  is by definition the Hugoniot or the Hugoniot equation of state for the solid. This curve then represents physically those states  $P$ ,  $V$  which can be obtained by shock compression from the initial state  $P_0$ ,  $V_0$ . Finally, equation (23)

can be used to calculate the internal energy difference,  $E - E_0$ , for the corresponding pairs of points  $P, V$ . The equation of state, along with certain of the specific heats, is sufficient for a complete thermodynamic description of a material.<sup>18</sup> The equation of state in  $P, V, E$  variables is a surface in  $P, V, E$  space. The Hugoniot with a given initial state  $P_0, V_0, E_0$ , describes a line on the equation of state surface. The initial states can be varied in order to map out the equation of state surface. One of the common techniques for this is to vary the porosity of the material. The porosity,  $m$ , is defined as the ratio of the normal density to the porous density. Besides using the Hugoniots to empirically determine the high pressure equation of state, they are used as reference states in many of the semi-analytical equations of state. Thus, the Hugoniot can be used in a series of reference states in the Mie-Gr nisen equation of state enabling states which are not on the Hugoniot to be described. For more complex responses in which elastic-plastic strain rate effects may be manifest, a constitutive model must be assumed and its parameters adjusted to characterize the observed response. One of the several codes available for accomplishing this is SWAP.<sup>19</sup>

For the experiments described in Section 5, it is important to minimize the tilt or the degree of non-planarity of impact. The reason for this is that measurements of the shock and particle velocities cannot be made locally but along various portions of the wave and therefore depend on the planarity and known orientation of the wave for their accuracy.

When a shock wave impinges upon a free surface, a rarefaction wave is generated upon reflection. A mass element which becomes encompassed

by such a rarefaction wave will undergo an adiabatic, although not necessarily isentropic, process taking the material from the shocked state to ambient pressures. Since the shock process takes the particles from the ambient state to the shock state in a non-equilibrium manner, only information about the final state can be obtained. In contrast, the release process, at least for non-pathological materials, is a continuous thermodynamic process and thus, in theory, information can be obtained about all the states along the adiabatic release path.<sup>20</sup>

In the case of geologic materials, the equation of state is complicated by the many high pressure polymorphs of the mineralogical constituents.<sup>21</sup> A phase change causes an initial step function shock to become unstable and break up into two shocks. By applying the jump conditions across the two shocks, the point of phase transition can be determined. Knowing the release adiabats in this case is especially important since it provides a continuous sampling of the states off of the Hugoniot. The retention of a strength or difference in principal stress in the high pressure shock state also plays a central role in the attenuation of strong shock waves. This is especially the case in rocks in the regime above a few kilobars and below the pressures at which phase transitions take place. When release waves, such as those emanating from free surfaces, propagate into shocked material, they travel at the local sonic velocity and overtake and reduce the magnitude of the shock front. Measurements of the release wave velocity are given in Section 5. The propagation characteristics of the release waves can be used to obtain information as to the state of the material behind the shock wave. Finite strength, phase changes and porosity strongly influence this velocity.

The above discussion has just touched upon some of the aspects of stress and shock propagation and their relation to the equation of state. For most geologic materials the combined effects of inhomogeneity, stress relaxation, phase changes, friction on crack surfaces, strain rate effects and porosity give rise to a complex mechanical response. Even for the simplest structural and geologic materials, we do not have a complete theoretical description of this response. It is with this realization that we turn to the techniques for experimentally obtaining these data.

In the following two sections, data obtained using the holographic techniques are compared with the analyses described above.

#### 4.0 LOW AMPLITUDE ELASTIC WAVE PROPAGATION STUDIES IN THE PLANE STRESS REGIMES

This section describes two holographic techniques to study low amplitude ( $\sim 0.1$  kbar), plane stress waves propagating in cylinders. The first technique, double-exposure interferometry, was developed allowing both the axial and radial deformation of a stressed cylinder to be measured simultaneously over the entire length of the rod. A comparison of experimental data with analytical predictions is also presented. Together with this technique, a method was developed allowing multiple holographic frames of a single event to be recorded. This technique permits a 1  $\mu$ sec time separation between frames which record the dynamic strain. This capability, however, has not yet been fully integrated into the holographic system. A description of this method is given in Appendix B.

The second technique, stored beam holographic interferometry, is applied to monitoring the axial motion of the end of a rod which has been impacted by a spherical pendulum. A comparison of the experimental results with the analytical predictions is given.

##### 4.1 Experiments Employing Double Exposure Holographic Interferometry (Longitudinal Waves in a Rod)

The application of double-exposure interferometry to dynamic events is made possible by the use of the pulsed ruby laser. The time duration of the laser pulses is short enough ( $\sim 50$  nanoseconds) to "stop" the motion of most events. This method involves making two holographic exposures in succession on the same piece of film. Typically, the first exposure is made of the undisturbed specimen. The second exposure is made a short

time after a disturbance has been introduced into the specimen. The result is two superimposed images (one formed by each exposure) which show a contour fringe pattern which is related to the deformation of the specimen between exposures. (A discussion of this technique is found in Appendix A.) The significance of this technique is that the spatial relationship of the deformation over the entire surface can be observed.

#### 4.1.1 Experimental Technique

The pulsed ruby laser which was used for this study has the unique capability of producing up to four, long-coherence, optical pulses (wavelength,  $\lambda = 6943\text{\AA}$ ) within one millisecond. The separation between pulses can be varied from one to 250 microseconds.

The main experimental problem which had to be overcome was that of synchronizing the laser with the wave propagation event. In order to understand how this timing problem was solved, it is first desirable to discuss the characteristics of the pulsed ruby laser.

The basic components of the ruby laser used in this experiment are two mirrors, a ruby rod, a flashlamp, and a Pockels cell. These are shown schematically in Figure 6. The two mirrors form opposite ends of the optical cavity. The ruby rod provides the optical energy (light) in a coherent, monochromatic form. The flashlamp "pumps" the ruby rod, making it ready to lase. The Pockels cell is situated between the mirrors and acts as a shutter for the cavity. When the proper voltage is applied to the Pockels cell, light is allowed to pass through it forming a complete optical cavity allowing the laser to lase. When there is no voltage applied, the Pockels cell isolates one mirror from the other and the optical cavity is no longer complete.

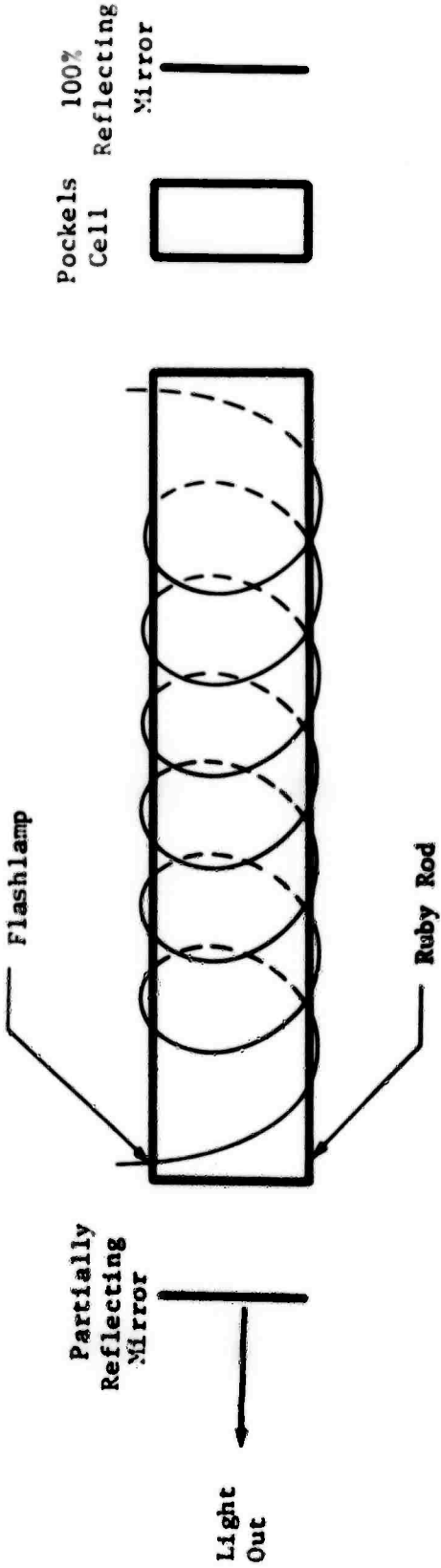


Figure 6. Schematic Representation of a Pulsed Ruby Laser



Precise timing is required for successful operation of the laser. The voltage to the Pockels cell must be applied from 800 to 900  $\mu\text{sec}$  after pumping the ruby rod by the flashlamp has begun. Only during this time period is the ruby rod sufficiently energized by the flashlamp for lasing.

In summary, the laser requires two separate commands, namely, one to trigger the flashlamp about 850  $\mu\text{sec}$  before lasing is to occur, and the second to activate the Pockels cell 800-900  $\mu\text{sec}$  after the flashlamp has been triggered. To meet these requirements for the proper operation of the pulsed ruby laser system, careful experimental procedures must be used. In effect, one must predict to within  $\pm 50$   $\mu\text{sec}$  when the light pulse from the laser is required and then supply proper triggering signals to the laser system. The experiments which we performed require that the Pockels cell be opened about 50  $\mu\text{sec}$  after rod impact by a pendulum. This means that the trigger signal to the flashlamp be supplied about 800  $\mu\text{sec}$  before impact. The flashlamp was triggered by means of a photocell and light beam arrangement. This light beam was interrupted by the spherical pendulum which was used to initiate the stress wave in the rod. When the light beam was broken, the pulse from the photocell was used to trigger a digital delay generator. This delay generator was set so that its output would trigger the laser flashlamp about 800  $\mu\text{sec}$  before impact.

The second triggering pulse (needed for the Pockels cell) was provided by the electrical contact between the steel pendulum ball and the rod specimen. (A thin coat of conductive paint was applied to the impacted face of the granite rod.) The signal from this contact was then applied to the Pockels cell control. This control could be set for a desired time

delay,  $\Delta t$ , before switching of the Pockels cell and subsequent lasing action. The time delay,  $\Delta t$ , together with the wave speed  $c_0$  can be used to calculate the position of the wavefront at the time the hologram was made.

With this timing arrangement, small fluctuations in the pendulum velocity ( $\Delta v$ , say) affect only the pumping time of the flashlamp but do not cause errors in the time delay of the Pockels cell,  $\Delta t$ . The actual time delay,  $\Delta t$ , was recorded on an oscilloscope and as such could be determined to within 0.5  $\mu\text{sec}$ .

The optics were arranged in such a manner that two holograms can be made of the stressed rod simultaneously. The positions of these holograms were chosen in accordance with the analyses given in Appendix A, Section A.2.2.1.

Referring to equation A.15, the displacement required to form a fringe on a double exposure hologram is given by

$$m = \frac{(2n-1)\lambda}{2(\cos\theta_1 + \cos\theta_2)} \quad (24)$$

where

$\lambda$  = wavelength of light being used (equals  $6943 \times 10^{-8}$  cm for a pulsed ruby laser)

$\theta_1$  = angle between the incident illuminating light and the displacement vector

$\theta_2$  = angle between the line of sight through the hologram and the displacement vector

$n$  = integer

One hologram, labeled film plane 1 in Figure 7, is arranged such that for the radial component of the displacement  $\theta_1 = \theta_2 = 0^\circ$  or

$$\begin{aligned} m_{\text{rad}} &= \frac{(2n-1)\lambda}{2(\cos 0^\circ + \cos 0^\circ)} \\ &= \frac{(2n-1)\lambda}{4} \end{aligned} \quad (25)$$

while for the axial component of displacement,  $\theta_1 = \theta_2 = 90^\circ$  or

$$\begin{aligned} m_{\text{axial}} &= \frac{(2n-1)\lambda}{2(\cos 90^\circ + \cos 90^\circ)} \\ &= \infty \end{aligned} \quad (26)$$

Interpretation of equations (25) and (26) is as follows. For this hologram a finite radial displacement [given by equation (25)] will cause a fringe to form. However, it takes an infinite axial displacement [equation (26)] to form a fringe on this hologram. That is to say, this hologram is sensitive to radial deformations only. The second hologram, labeled film plane 2 in Figure 7, is placed such that a line of sight through it forms a  $45^\circ$  angle with respect to the axis of the cylinder. This hologram is sensitive to both the axial and radial deformation. However, since the radial deformation is obtainable from the other hologram, it can be subtracted out to yield the axial deformation alone.

A schematic of the experimental apparatus is shown in Figure 7. Light emitted from the pulsed ruby laser is split into two parts by means of a beam splitter. The light transmitted through the beam splitter serves as the scene beam. A lens placed in the path of the light expands the beam. A second lens collimates the expanding beam. The collimated

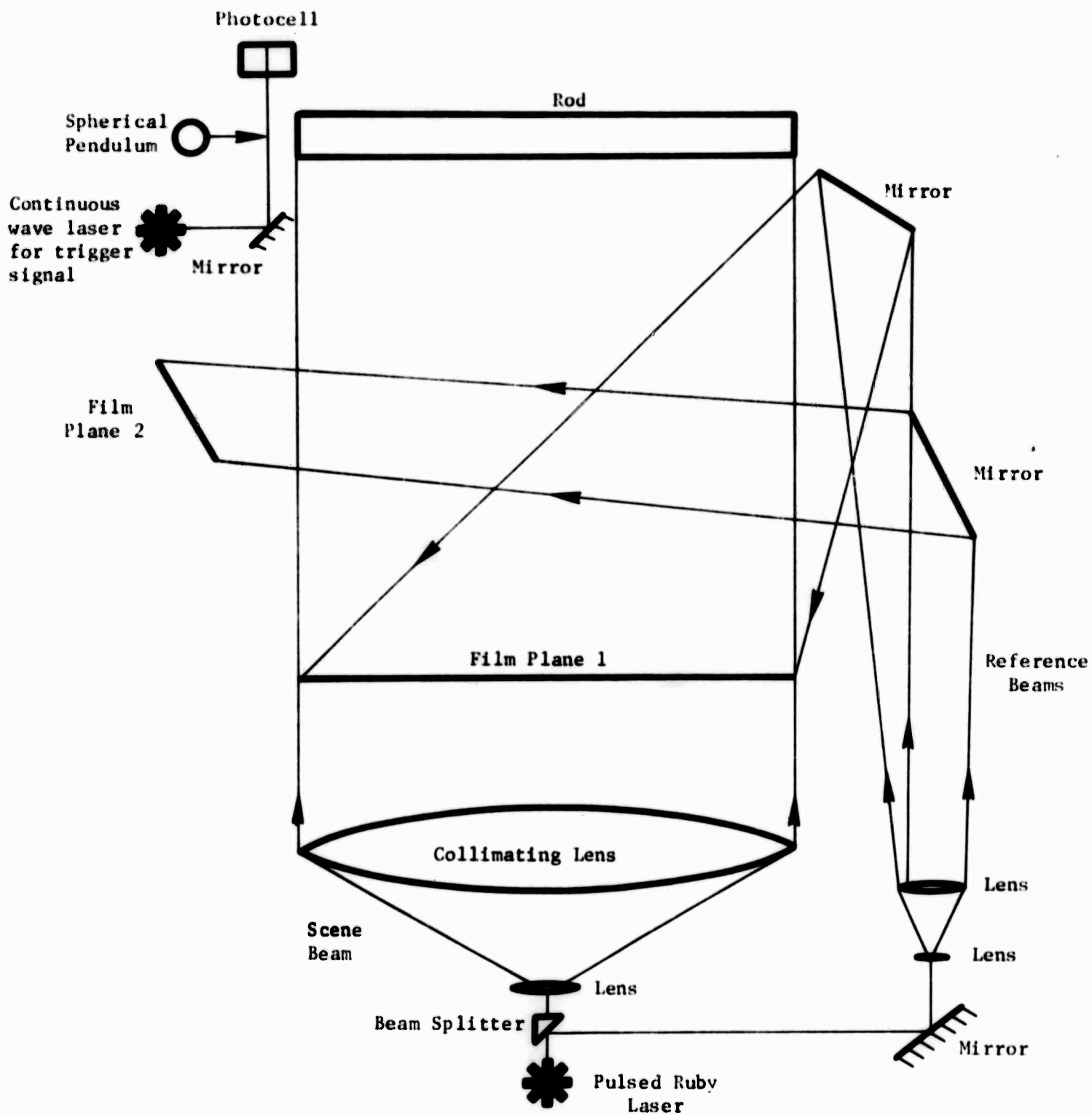


Figure 7: Experimental setup used to make double-exposure holographic interferograms of a rod supporting a stress pulse.

light then illuminates the cylinder. The light reflecting from the beam splitter serves as the reference beam. By means of a mirror this beam of light is directed through a lens where it becomes expanded. The expanding light is collimated by means of a second lens. The collimated light reflects from two mirrors (positioned in two different planes) and illuminates the holograms, i.e., film plane 1 and film plane 2. Film plane 1 consists of a 11-1/2" long strip of 35 mm film (with proper emulsions). This length was chosen so that the observer may view any part of the cylinder perpendicularly to its axis. Film plane 2 consists of a 4" x 5" plate of film.

#### 4.1.2 Test Procedure and Results

With the apparatus arranged as shown in Figure 7, double exposure holograms were made of a stressed aluminum rod (2024-T6). The rod measured 2" in diameter and was 11-3/4" long. The stress pulse was introduced into the rod by impacting one end with a spherical pendulum. The first exposure of the rod was made before impact. The second exposure was made 60  $\mu$ sec after impact. First the data contained on the radial sensitive hologram was reduced in a manner described in Section 4.1.1. This gave the radial component of the deformation which is shown by the lower set of data points in Figure 8. A photograph taken through this hologram is shown in Figure 9a. It should be noted that this photograph was taken through one part of the hologram and does not show the fringe pattern in the same way as the scanning analysis, i.e., line of sight always perpendicular to the axis of the rod. The wavefront is to the right in this photograph. The radial deformation reaches a maximum near the position where the fringes form a hyperbola. The large number of fringes on the left of Figure 9a are believed due to the large longitudinal deformations in that area.

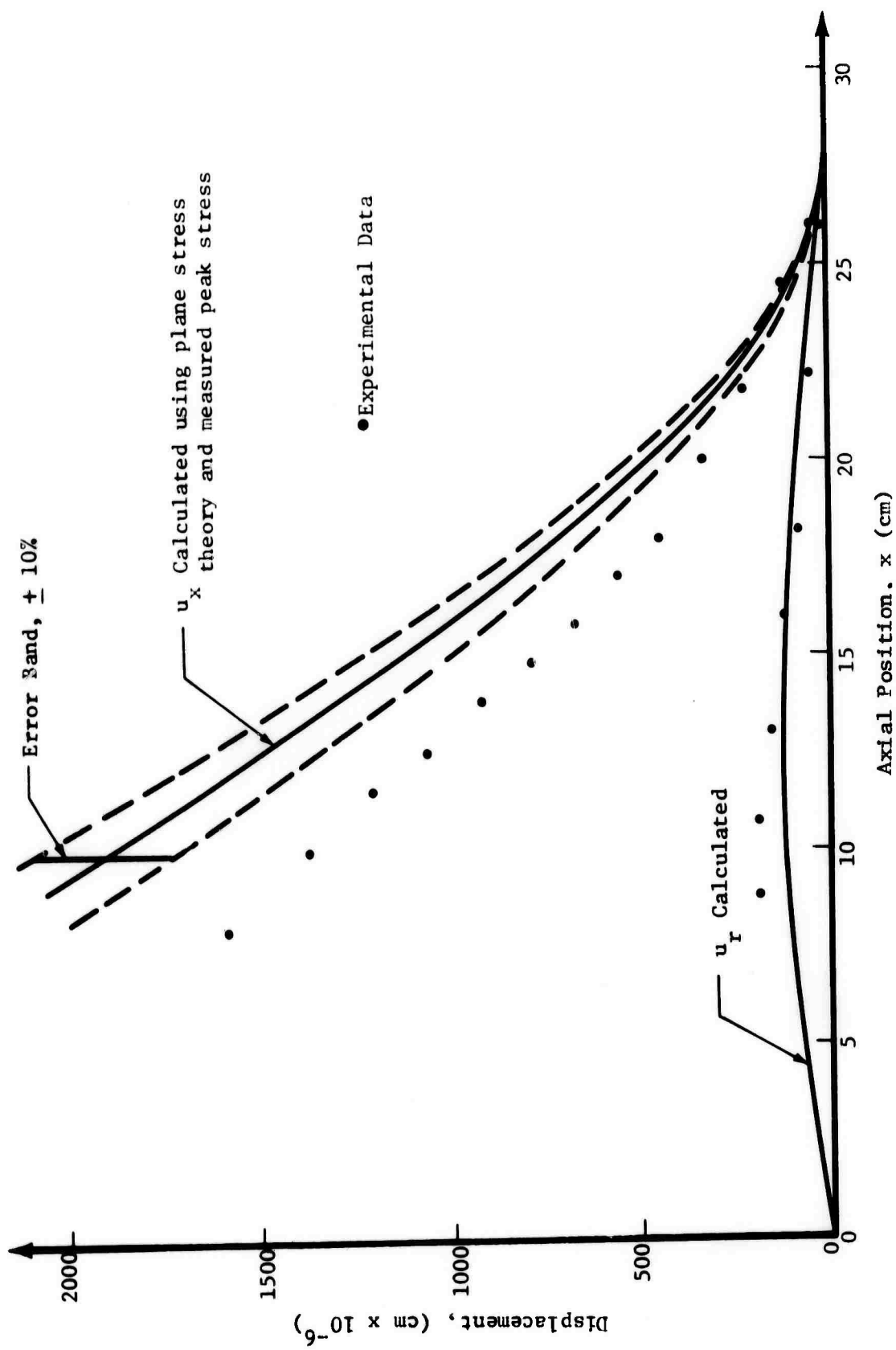


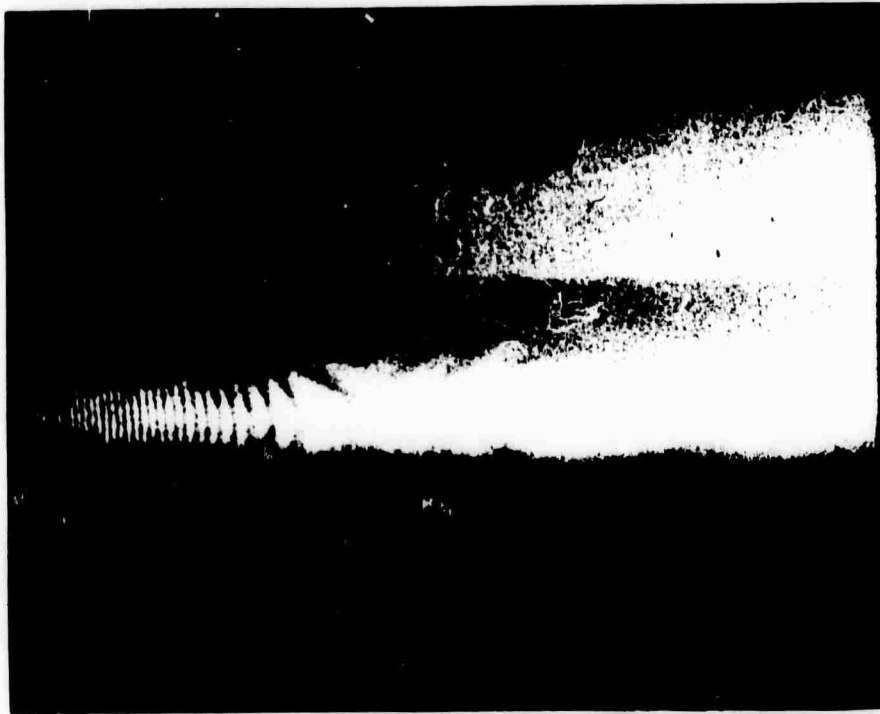
Figure 8. Longitudinal and Radial Displacements as a Function of Distance Along the Rod

TABLE I

LONGITUDINAL DEFORMATION DATA			
Fringe Order (n)	Position $x$ , cm	Deformation $u_x (10^{-6} \text{ cm})$	
1	26.0	39.7	
2	24.5	127	
3	21.8	225	
4	20.0	326	
5	18.0	441	
6	17.0	549	
7	15.8	668	
8	14.8	788	
9	13.8	916	
10	12.5	1059	
11	11.5	1203	
12	10.0	1372	
13	8.0	1588	

TABLE II

RADIAL DEFORMATION DATA			
Fringe Order (n)	Position $x$ , cm	Deformation $u_r (10^{-6} \text{ cm})$	
1	26.00	17.36	
2	22.25	52.07	
3	18.15	86.80	
4	16.00	121.5	
5	12.90	156.2	
6	10.75	190.9	
6	8.80	190.9	



(a)



(b)

Figure 9. Holographic Interferogram of a Stress Pulse Propagating in an Aluminum Rod.

- (a) Interferogram sensitive to radial displacements
- (b) Interferogram sensitive to both axial and radial displacements



The longitudinal deformation was determined from the second hologram of the same event, i.e., film plane 2. In this case the hologram is sensitive to both the radial and longitudinal components. The radial component, having already been determined separately, can be subtracted out yielding the longitudinal component. The resulting curve of longitudinal displacement vs position on rod is shown in Figure 8 (data tabulated in Tables I & II). A photograph taken through this hologram is shown in Figure 9b. Again the hyperbola in the fringe pattern is related to a maximum in the radial displacement; it was not readily apparent how to interpret the fringes to the left of the hyperbola.

Also shown in Figure 8 are the calculated axial and radial displacements, based upon elementary plane wave theory discussed in Section 2.2. These calculations are in good agreement with the experimental data. The analysis assumed a stress pulse having a half-sine wave shape.

This theoretical stress pulse was a close approximation to the actual stress pulse in the rod, which was measured using the well-known manganin gauge technique. The shape of the measured stress pulse is shown in Figure 10.

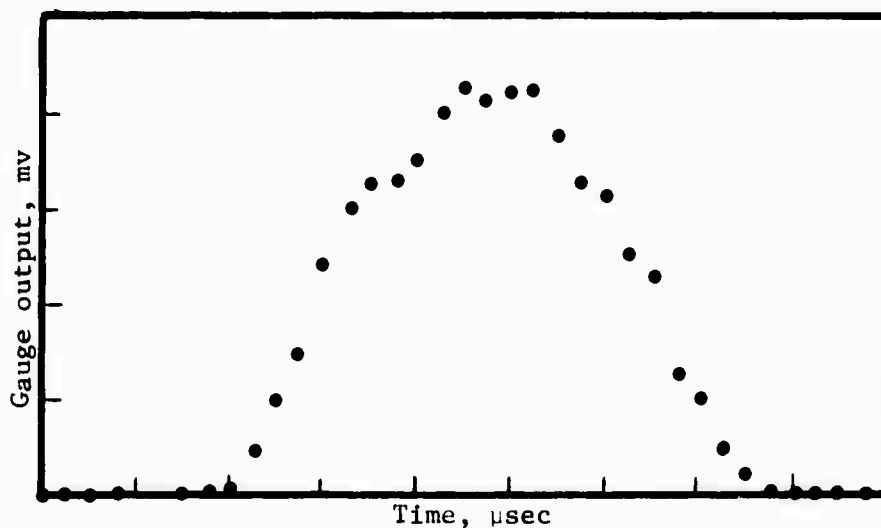


Figure 10. Stress Pulse Measured by a Manganin Gauge (Pendulum Impact)

From the measured values of longitudinal displacement ( $u_x$ ) and radial displacement ( $u_r$ ), it is possible to compute the dynamic Poisson's ratio. For example, in the middle section of the rod ( $x = 10$  to  $16$  cm in Figure 8) we have

$$\epsilon_x = \frac{\Delta u_x}{\Delta x} = \frac{1203 - 668}{11.5 - 15.8} \times 10^{-6}$$

$$\epsilon_x = -124.5 \times 10^{-6} \text{ (compression)}$$

$$\epsilon_r = \frac{u_r}{a} = \frac{156.2 \times 10^{-6} \text{ cm}}{2.54 \text{ cm}} = 61.5 \times 10^{-6}$$

$$\epsilon_r = 61.5 \times 10^{-6}$$

Finally, we have

$$\nu = -\frac{\epsilon_r}{\epsilon_x} = \frac{61.5}{124.5} = .494 \text{ for Poisson's Ratio}$$

This calculation assumes that the rod behaves according to elementary plane stress theory. The calculated value of  $\nu \cong .5$  strongly suggests that the waves are not plane at the station  $x = 13$  cm. This suspected non-planar behavior results from the central, point impact which the steel pendulum ball imparts to the rod.

A similar calculation between the stations  $x = 22$  cm and  $x = 26$  cm gives

$$\epsilon_x = \frac{225 - 39.7}{21.8 - 26} \times 10^{-6} = -44.0 \times 10^{-6}$$

$$\epsilon_r = \frac{52.07 \times 10^{-6}}{2.54} = 20.5 \times 10^{-6}$$

$$\nu = -\frac{\epsilon_r}{\epsilon_x} = \frac{20.5}{44.0} = .466 \text{ for Poisson's Ratio}$$

The value of  $\nu = .466$  for 2024 aluminum is high compared to the value of  $\nu = .348$  given in Reference 22. This result again suggests that the elementary theory does not apply to our impact problem. It is suspected that the wavefronts are non-planar, because of the point load at  $x = 0$ .

Once this double-exposure technique had been demonstrated on the aluminum rod, similar holographic experiments were done using granite rods. The results of the experiments are shown in Figure 11, which shows four interferograms made at various time delays,  $\Delta t$ . Shortly after these photos were obtained, the experimental program was redirected toward obtaining higher stress levels. The latter experiments are discussed in Section 5.

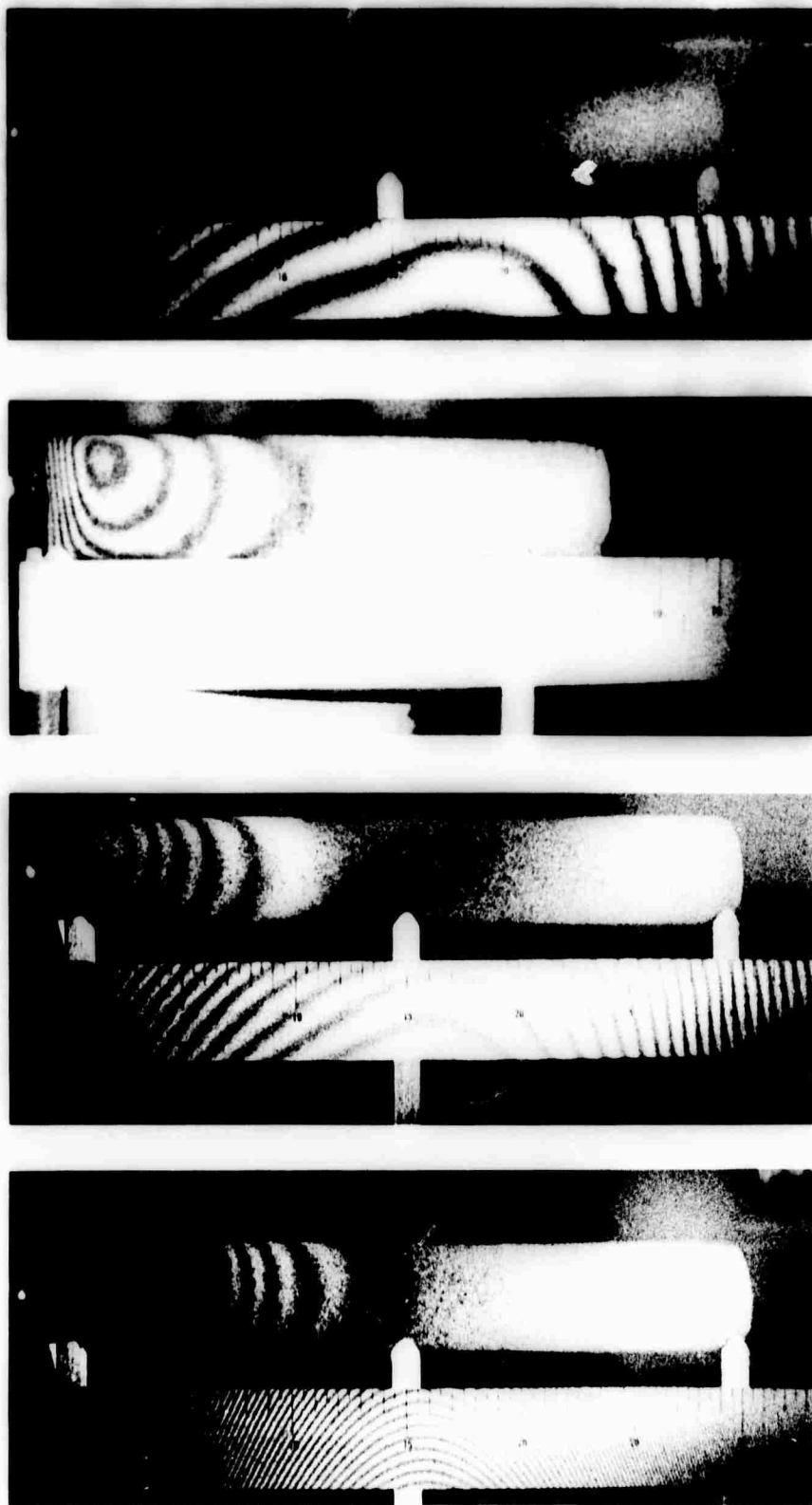


Figure 11. Double-Exposure Holograms Showing Stress Waves in a Granite Rod

#### 4.2 Measurement of the Time-Dependent Displacement of the Free End of an Impacted Rod

The experiment described here was originally designed to assess effects of cracks and porosity on wave propagation in rods of geological materials. Most conventional techniques for dynamic stress and strain measurements, such as foil gauges, accelerometers, etc., monitor the deformation of the specimen at discrete locations as a function of time. On the other hand, double exposure holographic interferometry can measure deformations over a large area, but only at discrete times. It was decided to investigate a holographic technique which could be used to measure deformations continuously in granite and aluminum rods. For this purpose, a stored beam interferometry technique was developed which can measure the axial and radial deformation of the surface of a specimen on a real-time basis.

A stored beam interferogram is made by superimposing the virtual holographic image taken of an object before stresses are applied onto the actual object (see Appendix A for a discussion of this technique). This is accomplished by viewing the object through the hologram which has been repositioned into the exact position it assumed during its exposure. If the surface of the object is then deformed, an interferometric fringe pattern is observed in real-time. The fringes which form due to deformations caused by dynamic impact events of interest for this study occur too rapidly to be observed with the unaided eye, or even a high speed motion picture camera. For this reason, it was necessary to develop a photocell readout technique to monitor the displacement fringes. This imposes the restriction of observing discrete locations on the surface of the specimen. One point of particular interest in an experiment involving a stress wave

traveling down a cylindrical rod is the center of the end of the rod opposite to the struck end. Thus, a stored beam system was constructed to monitor the axial deformation at the end of a struck granite rod. These data may then be used to calculate the dynamic modulus and attenuation for one-dimensional stress waves in the material.

#### 4.2.1 Experimental Technique

The stored beam interferometry system was set-up on an 8000-lb granite table to insure the stability of all components during the tests. A 15 milliwatt HeNe laser (wavelength  $6328\overset{\circ}{\text{\AA}}$ , Spectra Physics Model 124A) was used to make a hologram of the end of a cylindrical specimen. A schematic of the holographic setup is shown in Figure 12. A photograph of the actual laboratory setup is shown in Figure 13.

The light constituting the scene beam illuminated only a small area at the center of the rod. The hologram was placed in a holder which allowed it to be precisely repositioned after its development. Using a lens placed behind the hologram, the interferometric fringe pattern was focused onto the face of a photocell. The output of the photocell was then displayed on an oscilloscope where it was photographed.

Tests were made using a 2" diameter granite rod. The granite rod was supported by two v-shaped holders as shown in Figure 13. Because of the diffuse scattering of the light from the granite surface, it was necessary to use a highly sensitive photo pickup device. A photomultiplier tube (RCA type 7265) with a high sensitivity at  $6328\overset{\circ}{\text{\AA}}$  was employed. The output was read onto a dual beam oscilloscope (Tektronix #556) so that it could be recorded for a longer time.

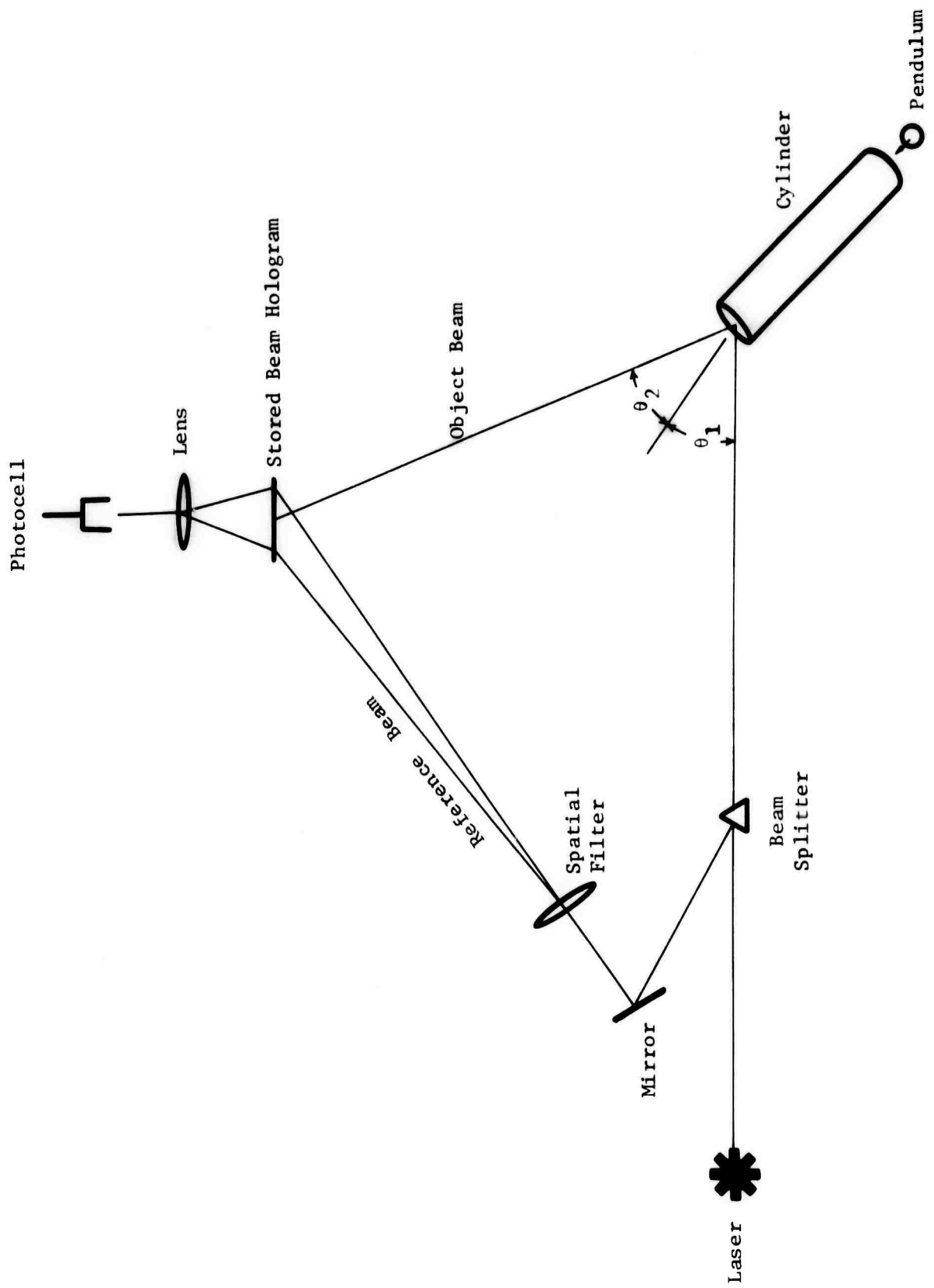


Figure 12: Schematic of Stored Beam Interferometry Test Set-up

A thin metal foil was attached to the impacted end of the granite rod. The electrical contact between this foil and the pendulum was used to trigger the scope. Certain discrepancies in the initial delays of the fringes can be attributed to poor contact of the foil with the granite.

As the end of the rod is deformed outward, the photocell reads alternatively light and dark corresponding to the change in path length of the light. One fringe (dark) will form whenever the displacement of the end of the rod meets the condition imposed by equation A.15:

$$m = \frac{(2n - 1)}{2(\cos\theta_1 + \cos\theta_2)} \lambda \quad (27)$$

The sensitivity of this measure can be adjusted by varying  $\theta_1$  and  $\theta_2$ .



Figure 13: Granite Cylinder and Spherical Ballistic Pendulum Used to Develop the Stored-Beam Interferometry Technique



An elastic stress wave was introduced into the rod by impacting one end with a pendulum. The oscilloscope traces of two such events are shown in Figure 14. In both cases, the oscilloscope was triggered by the impact. The trace in the upper photograph is traveling at 50  $\mu\text{sec}/\text{cm}$ . The initial stress pulse only produced four fringes indicating that the cylinder was not struck very hard. The cylinder was hit much harder for the event in the lower photograph as evidenced by the 21 fringes produced by the initial stress pulse. (Here the trace has been delayed by 40  $\mu\text{sec}$  after impact and sweeps at 10  $\mu\text{sec}/\text{cm}$ .) In these photographs, each succeeding fringe can be interpreted as a displacement of  $k \lambda/2$ , where  $k$  is found by inserting the proper angles into equation 27. The theory of the wave propagation in a rod, as it pertains to these experiments and the resulting data analyses are presented in the next two sections.

#### 4.2.2 Longitudinal End Displacement (Theoretical Results)

The stress wave profiles induced by ball impacts are, in general, not simple analytic functions. It is useful, however, to consider a rectangular pulse propagating to the right along a rod, as analyzed by elementary theory. The pulse height is  $\sigma_0$  and its width is  $\Delta$  (sec.), Figure 15.

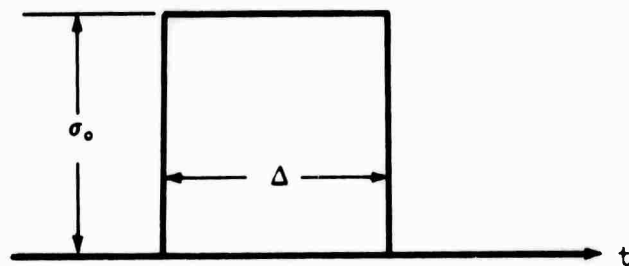
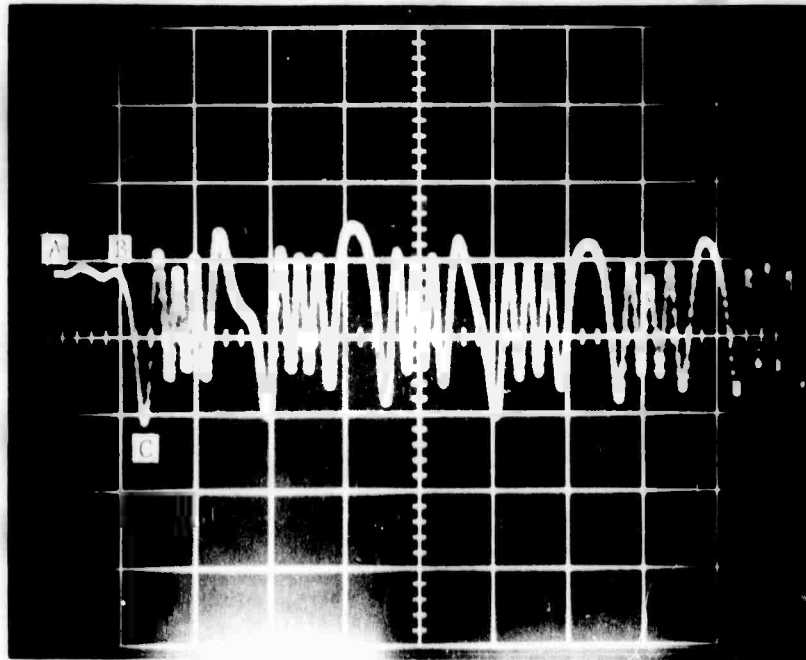
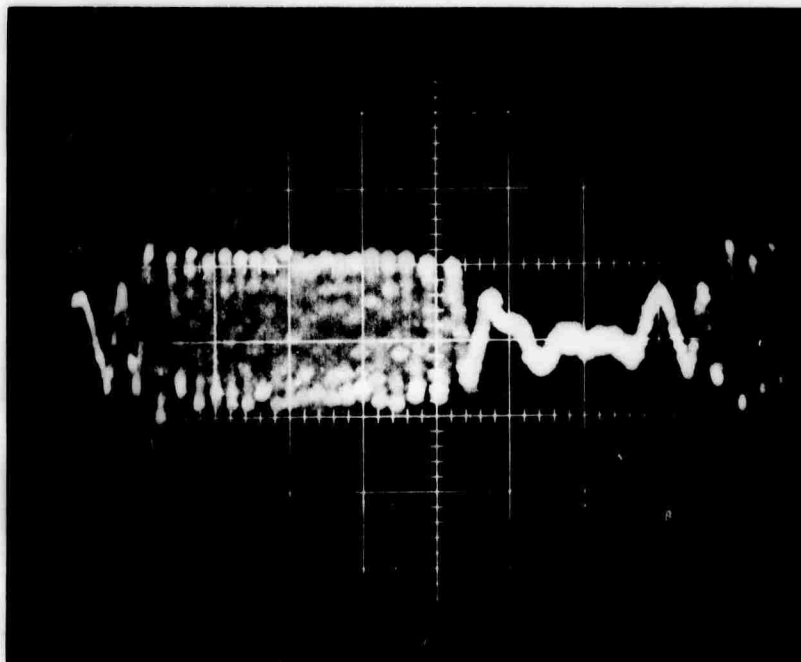


Figure 15: Rectangular Stress Pulse



Time Axis: 50  $\mu\text{sec}/\text{cm}$

- A) time equals zero - impact occurs
- B) first fringe begins to form
- C) first fringe is fully formed



Time Axis: 10  $\mu\text{sec}/\text{cm}$ , delayed 40  $\mu\text{sec}$

Figure 14. Oscilloscope Traces of Photocell Outputs During Spherical Pendulum-Aluminum Fillet Tests

This rectangular pulse can be considered as the superposition of two step functions, separated in time by a delay,  $\Delta$ .

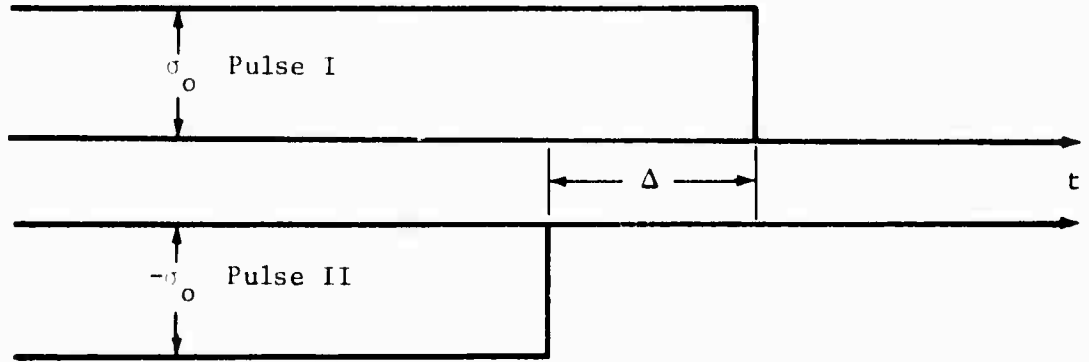


Figure 16: Superposition of Two Step Functions

When the first pulse (I) strikes the free end of the bar, the displacement starts from zero with a velocity given by

$$\dot{\xi}_I = \frac{2\sigma_0}{\rho c_0}$$

The corresponding end displacement is

$$\xi_I = \frac{2\sigma_0}{\rho c_0} \left( t - \frac{\ell}{c_0} \right) \quad \text{for } 0 \leq t - \ell/c_0 \leq \Delta$$

where  $\ell/c_0$  is the time required for the pulse to travel the length of the rod. When the second pulse (II) arrives, it imparts a velocity given by

$$\dot{\xi}_{II} = -\frac{2\sigma_0}{\rho c_0}$$

since Pulse II is the negative of Pulse I. Superimposing the results from Pulse I and Pulse II, we have

$$\dot{\xi}_{\text{Total}} = \dot{\xi}_{\text{I}} + \dot{\xi}_{\text{II}}$$

$$\dot{\xi}_{\text{Total}} = \frac{2\sigma_o}{\rho c_o} \quad \text{for } 0 \leq t - l/c_o \leq \Delta$$

$$\dot{\xi}_{\text{Total}} = \frac{2\sigma_o}{\rho c_o} - \frac{2\sigma_o}{\rho c_o} = 0 \quad \text{for } \Delta \leq t - l/c_o$$

as long as no reflections from the left end of the bar occur. However, the original rectangular compression pulse (which started out moving to the right) reflects as a tension pulse moving to the left. (See Figure 17)

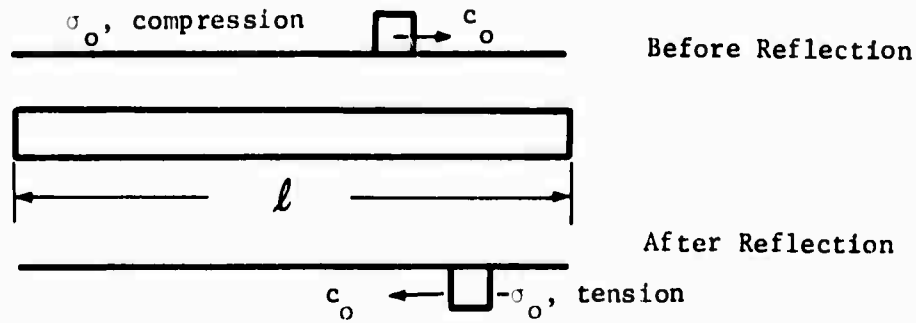


Figure 17: Reflection of Pulse at the Right End of the Bar

When the tensile pulse reaches the left end of the rod, it reflects as a compression pulse moving back to the right, since the left end is stress-free. This second compression pulse can be handled just like the original one, and the process is repeated. The second pulse arrives at the right end at a time  $2l/c_o$  after the first pulse. This is the time required for the pulse to travel once to the left and then back to the right along the rod. The resulting displacement-time history (at the right end of the rod) is shown in Figure 18 by the solid line.

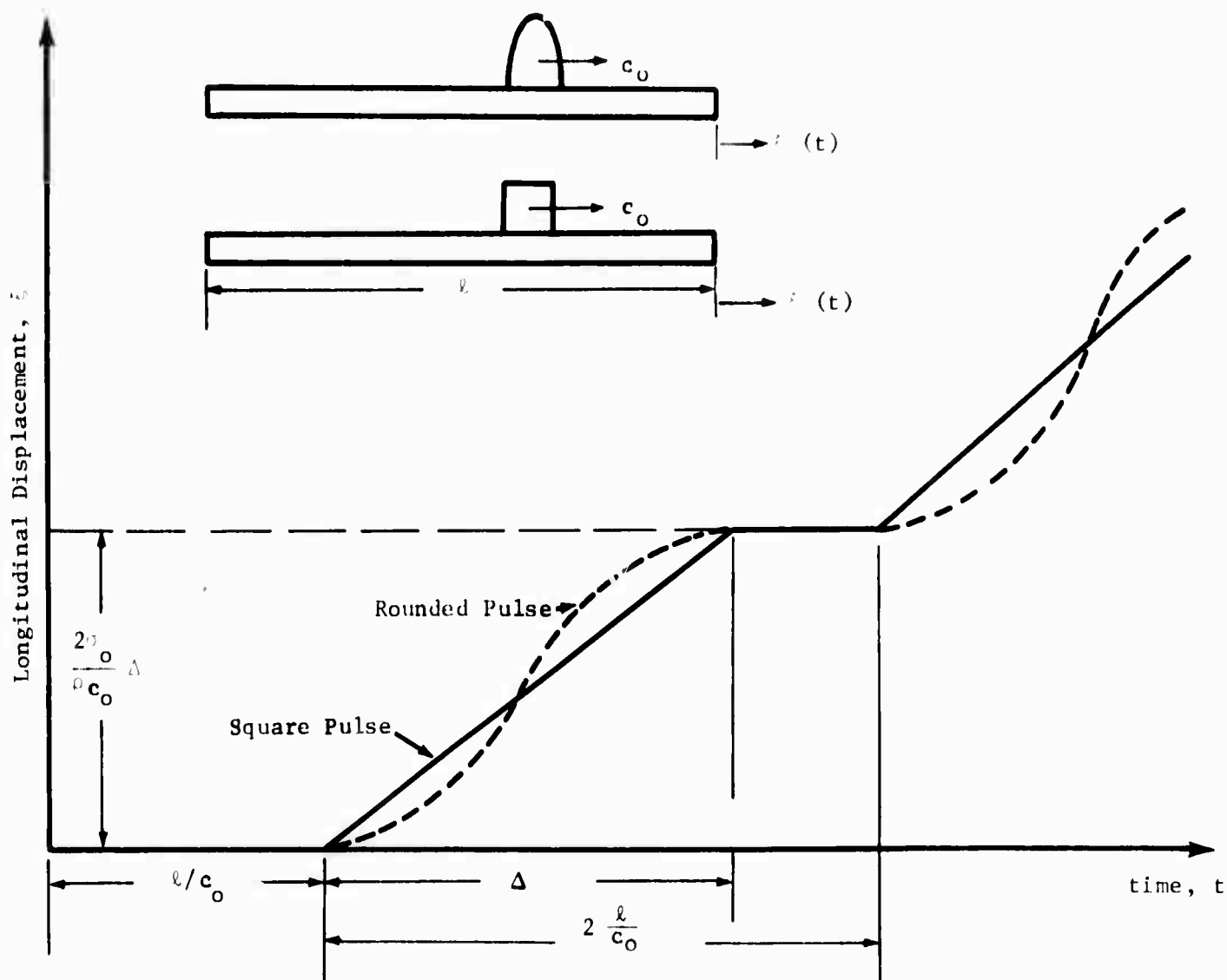


Figure 18. End Displacement,  $\xi$ , for a Rectangular Compression Pulse

In actual experiments, the pulse shape is not rectangular, but is rounded off at the corners. The effect of a rounded pulse is to alter the displacement-time history, as shown qualitatively by the dashed line in Figure 18.

#### 4.2.3 Experimental Results

Figure 19 shows the oscilloscope record of a spherical pendulum-granite cylinder impact. A dual-beam oscilloscope was used to extend the time span over which the record was taken. Both traces swept at 20  $\mu\text{sec}/\text{cm}$ . The upper trace was triggered by an electrical contact just prior to the impact. The lower trace has been delayed 180  $\mu\text{sec}$ , so that the total record extends for 380  $\mu\text{sec}$ . For these tests, the angles of incidence and reflection of the light off the granite cylinder were both  $18^\circ$ , therefore, from equation 27, each fringe represents a surface displacement of  $1.66 \times 10^{-5}$  cm.

The data from Figure 19 was interpreted to yield a time history of the free end displacement of the granite rod (Figure 20). The stress pulse due to the impact reached the free end of the bar at 80  $\mu\text{sec}$  after the scope was triggered. At this time, the surface was accelerated outward. An analysis of this curve can yield information on a number of material properties of the granite specimen.

The stress pulse had a duration of  $\sim 90$   $\mu\text{sec}$ . Differentiating this curve would yield its magnitude and time history. Upon reaching the free end of the rod, the stress pulse is reflected, travels back down the rod and is eventually reflected back to the free end at 208  $\mu\text{sec}$ . At this time the free surface is again accelerated. The sound velocity of the rod can be calculated from this round trip transit time of 128  $\mu\text{sec}$ . The length of the granite rod is 11-1/4 inches yielding a velocity of .45 cm/ $\mu\text{sec}$ .

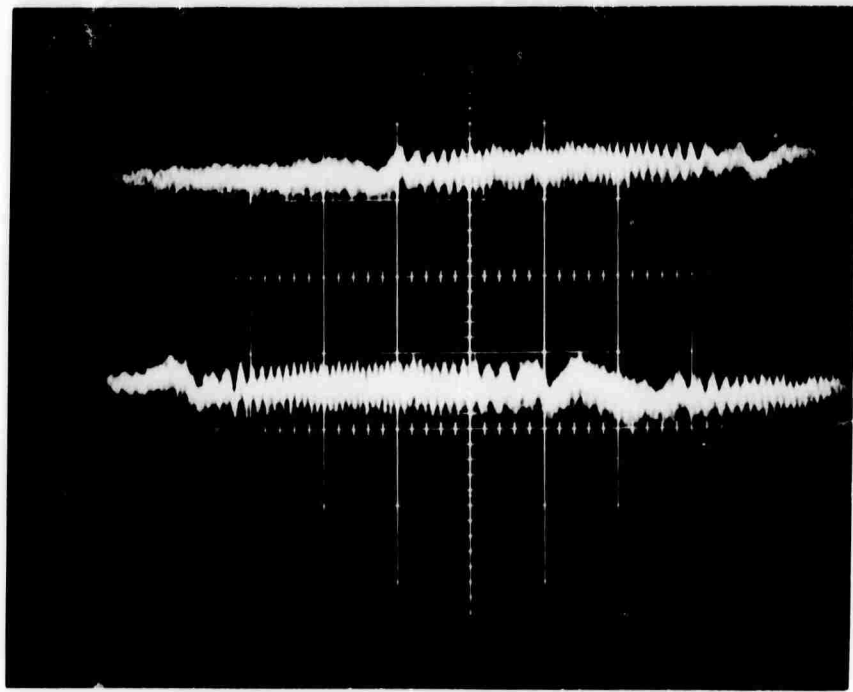


Figure 19 Oscilloscope record of spherical pendulum granite cylinder impact. Time scale is 20  $\mu\text{sec}/\text{cm}$ . Lower trace is delayed by 180  $\mu\text{sec}$ .

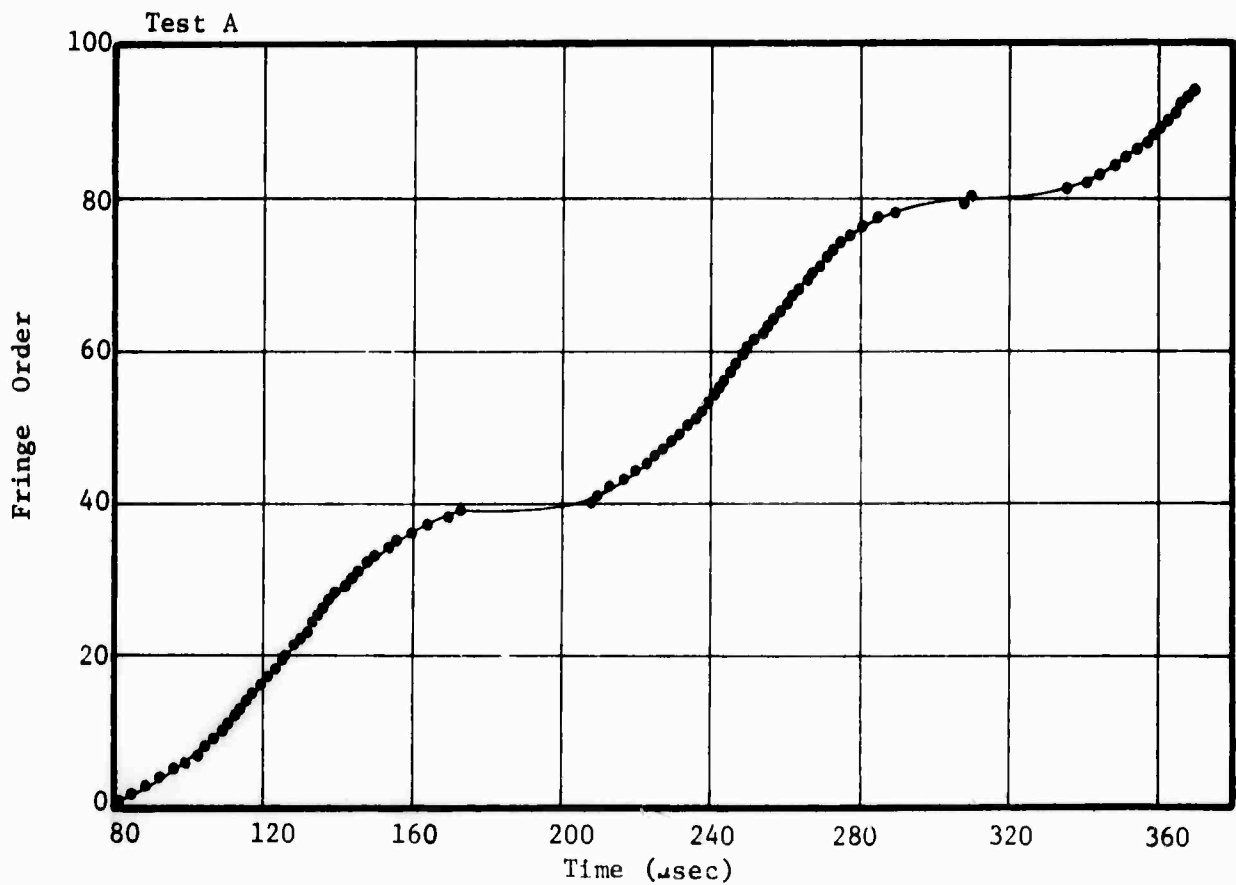


Figure 20 : Displacement time history of the free end of the granite cylinder as determined from the oscilloscope trace shown in Figure 19.

(Each fringe corresponds to a displacement of  $1.66 \times 10^{-5}$  cm)

Note that the time lag between the second and third pulses yields the same result:  $c_o = 0.45$  cm/ sec. The sound velocity can then be used to find Young's Modulus for the material:

$$E = c_o^2 \rho_o$$

$$= 5.3 \pm 0.1 \times 10^{11} \text{ dyne/cm}^2$$

We note that this stress pulse as a dynamic Young's Modulus which is 6% higher than that determined by the static compression test (section 2). The maximum free surface velocity can be found by taking the slope of the curve: 9.5 cm/sec. From these numbers, the stress, strain and rate of strain can be calculated:

$$\text{maximum stress} = \sigma_x = \frac{\dot{\epsilon}_{FS}}{2} \rho_o c \quad \text{where } \dot{\epsilon}_{FS} \text{ is the velocity of the free surface}$$

$$= 5.6 \times 10^6 \text{ dyne/cm}^2$$

$$\text{strain} = \epsilon_x = \frac{\sigma_x}{E}$$

$$= 1.1 \times 10^{-5}$$

$$\text{strain rate} = \dot{\epsilon}_x = \frac{\epsilon}{\frac{1}{2} \text{ pulse duration}}$$

$$= 0.24 \text{ sec}^{-1}$$

Attenuation effects in the specimen can be measured by comparing the stress pulses for successive reflections and noting the total displacement due to each pulse. The test shown in Figure 20 shows that both the first and second pulses produced a displacement of 39 fringes or  $6.5 \times 10^{-4}$  cm. Thus, the attenuation of the stress curve,  $\alpha$ , is measured to be less than



$2.62 \times 10^{-4}$  nepers/cm. One would expect that the attenuation constant could be measured to greater accuracy if the time history was recorded for longer times.

Figures 21 and 22 show a record of another granite impact test. Here, the rod was not impacted as hard as in the previous case as evidenced by less fringes per pulse (34 as compared to 39 previously). Analysis of these data yields results similar to those discussed above.

#### 4.2.4 Evaluation of Stored Beam Interferometry

The ability of this system to record dynamic events is limited by its high sensitivity. For fast events, too much data is acquired too fast to be handled by conventional recording equipment. The photomultiplier tube used in these tests had a rise time of 6 nanoseconds. Faster photo devices are available, however, the system is limited by other components. Most conventional recording instruments such as charts, tapes, disc or even on-line computer cannot record data as fast as it is processed by the photomultiplier tube. One practical method is an oscilloscope which, although it has the speed, is limited in the amount of data which can be recorded, i.e., only a finite number of data points can be resolved on a single trace. A dual-beam scope was used for this study to double the storage capacity. Other solutions could be to use a larger number of oscilloscope traces with consecutive time sweeps or to use a raster type of display. In any case, it appears that the type of recording instrumentation used will determine the limitations of system.

The recording of fringes at the rate of  $2 \times 10^8$  per second was attainable with instrumentation used for this study. If each fringe

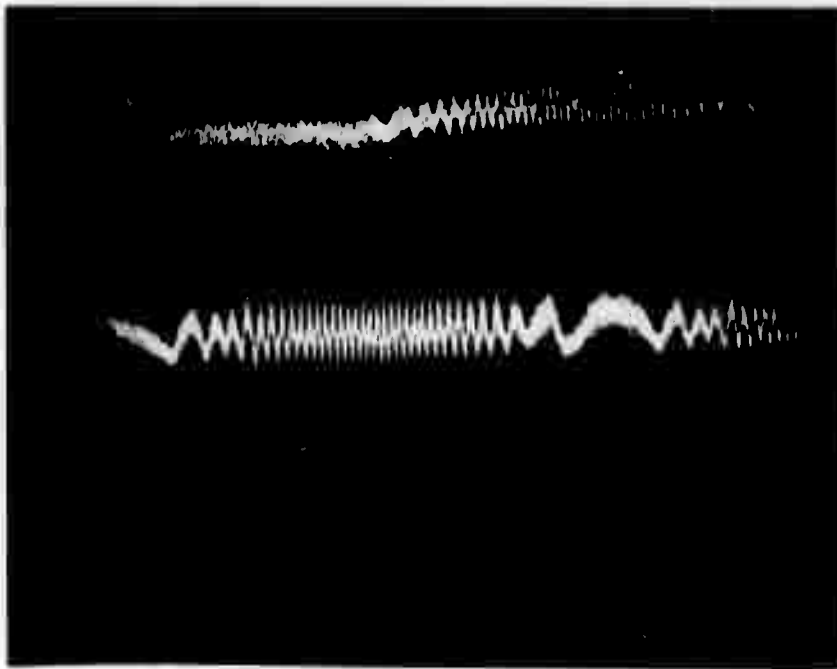


Figure 21: Oscilloscope record of spherical pendulum-granite cylinder impact. Time scale is 20  $\mu\text{sec}/\text{cm}$ . Lower trace is delayed by 180  $\mu\text{sec}$ .

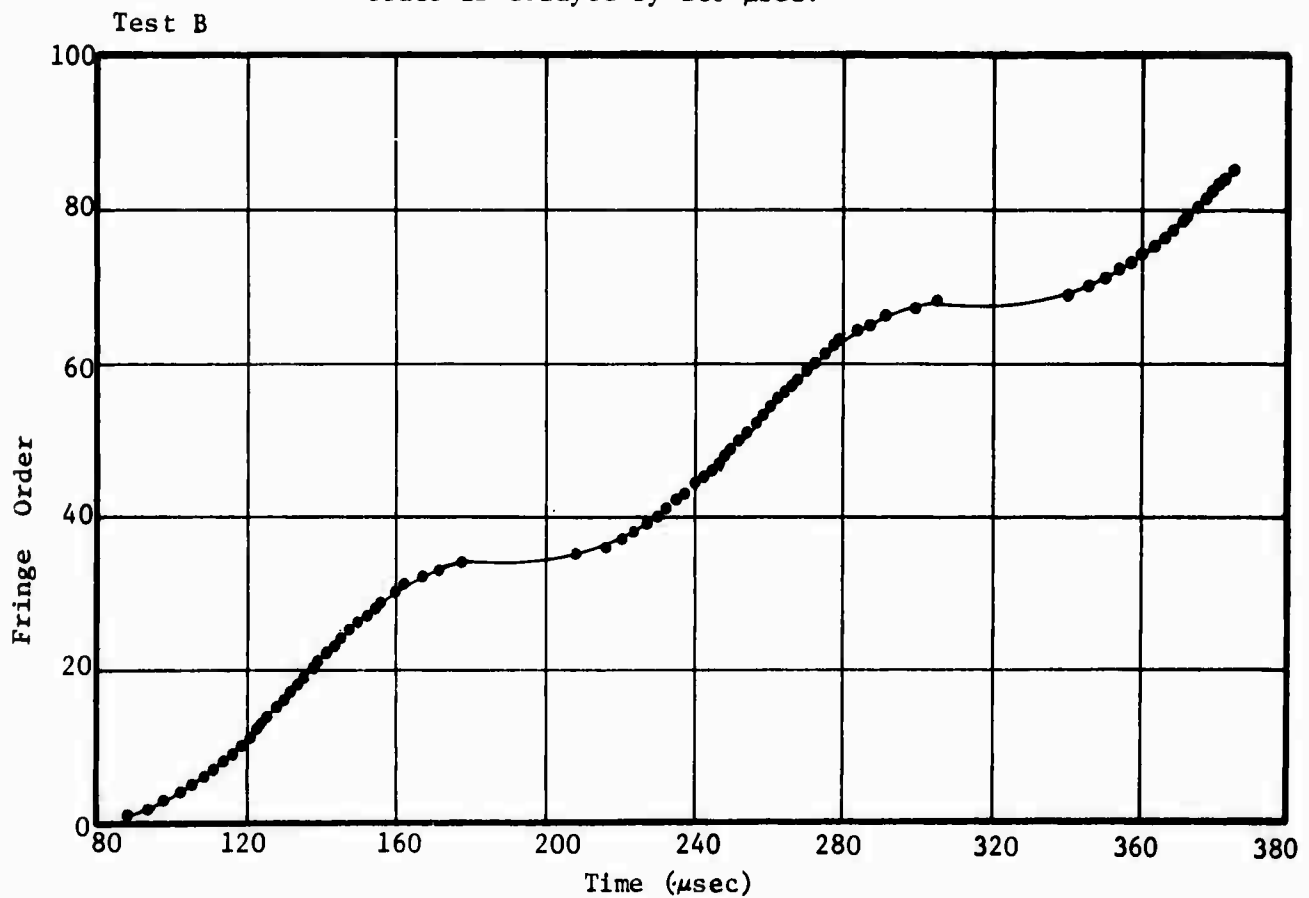


Figure 22: Displacement time history of the free end of the granite cylinder as determined from oscilloscope record shown in Fig. 21.  
(Each fringe corresponds to a displacement of  $1.66 \times 10^{-5} \text{ cm}$ )

represents a displacement of  $\lambda/2 = (3.164 \times 10^{-5} \text{ cm})$ , then this represents a surface velocity of  $6.328 \times 10^3 \text{ cm/sec}$ . From equation 27, it is apparent that the system can be de-sensitized by increasing  $\theta_1$  and  $\theta_2$ . In practice, this allows a maximum readable surface velocity to be increased by about a factor of 3 or in this case to  $1.9 \times 10^4 \text{ cm/sec}$ . While this is adequate for many experiments, it is too low for the high stress level experiments which were planned for the second part of this study.

## 5.0 LARGE AMPLITUDE STRESS WAVE PROPAGATION STUDY

The experiments described in the previous section were performed at relatively low stress levels. There, emphasis was placed on developing general holographic techniques which could be applied to study low amplitude elastic wave propagation in geological materials. This section describes efforts applied to developing holographic instrumentation to study large amplitude stress propagation in the plane strain regime. In this regime, very close to the point of impact, the stress wave has not yet been influenced by edge effects. In the sections which follow, a description of the experimental apparatus, experimental results and correlation with other published data is presented. The theoretical aspects of wave propagation in the plane strain regime are given in Section 3.3.

### 5.1 Experimental Method

A straightforward technique for producing plane shock waves in target materials is by impaction with a flat plate which has been accelerated to high velocity by means of a gas gun.<sup>23</sup> Upon impact of the plate with the target, plane shock waves are driven into both the target and impactor. Two of the many simple target geometries which can be used in such experiments, are a flat plate and a wedge. The flat plate target is the conventional configuration which has been used to obtain Hugoniot of materials. The shock wave velocity is obtained from the known thickness of the target, and the measured transit time of the shock. The particle velocity is either deduced from the target free surface velocity or from use of the impedance mismatch technique.<sup>18</sup> In the latter

case, the projectile velocity must be measured. From the previous discussions it should be apparent that these two measurements are sufficient to define a state on the material's Hugoniot. Holography could, in principle, be used here to obtain either the surface displacement or velocity at specific times. This configuration, however, does not exploit the unique capability that holography offers; that is, the determination of the three-dimensional displacement or velocity field at specific times. By inclining the surface opposite the impacted surface at some angle, the whole temporal history of the wave interaction with the free surface can be determined from a single hologram. Figure 23 is an illustration of a wedge configuration of granite, in which a flyer plate of granite impacts and drives a shock into the wedge. The geometrical constraints on the flyer plate's thickness and wedge angle are to be discussed in Section 5.1.1. The shock wave, upon reflection, accelerates and deforms the free surface. The displacement of the free surface at various times, or in the case of a wedge, at various shock propagation path lengths, provides information on the states achieved by the material during the shock and subsequent adiabatic release processes. If the material were elastic-plastic, the positions at which changes in the free surface velocities take place reflect the positions of the various shock and release waves. Also, values of the resultant free surface velocities reflect the amplitudes of these waves. In the case where a material exhibits a phase change, this would manifest itself in a variation in the gradient of the displacement along the wedge surface. If the material work hardens, then the displacements and velocities between the elastic and plastic waves would not have a

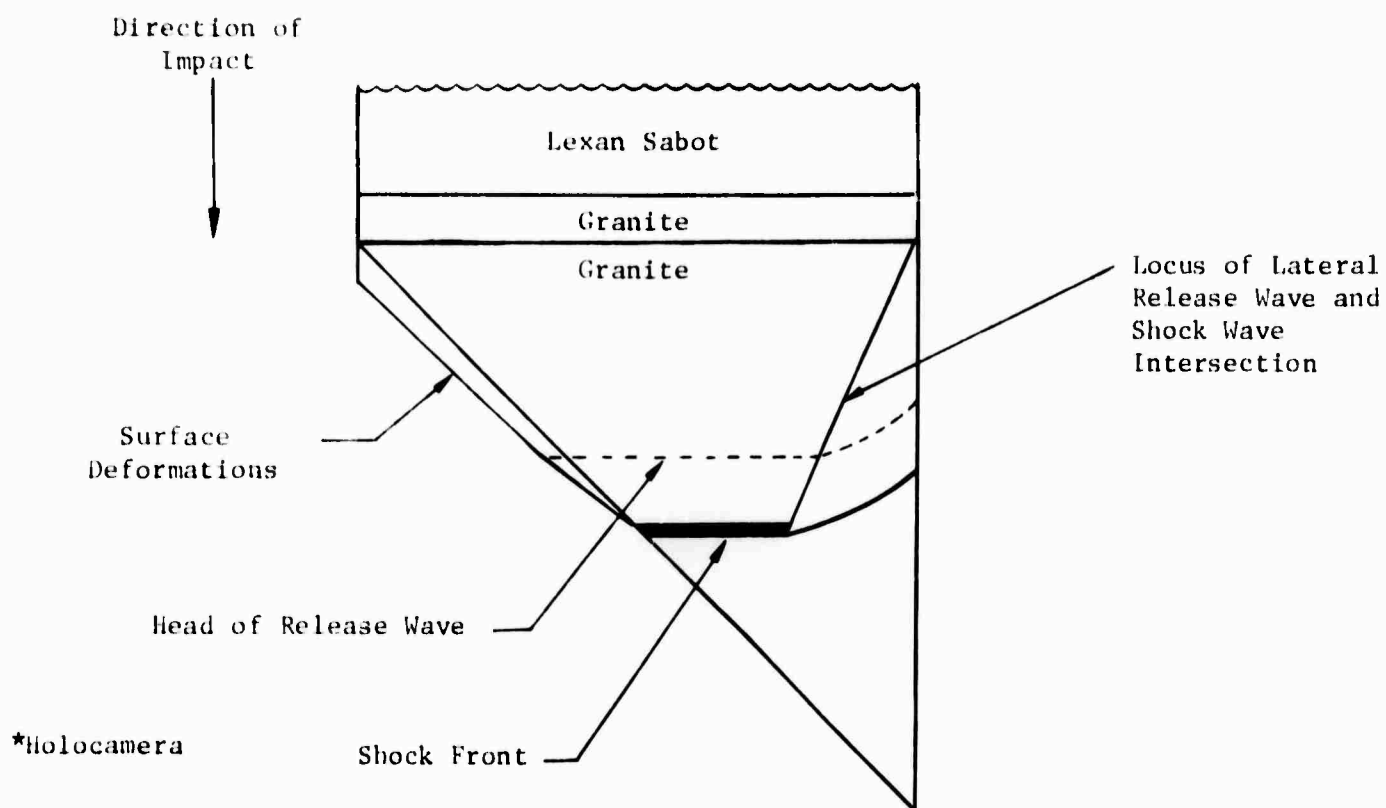


FIGURE 23 WEDGE CONFIGURATION USED TO HOLOGRAPHICALLY  
DETERMINE A MATERIAL'S SHOCK PROPERTIES

constant gradient. Release wave positions and the subsequent expansion can also be determined from changes in the displacements and from the free surface velocities. Therefore, an examination of the morphology of the holographically determined displacement or velocity field would quickly determine the material class of the target.

It will be demonstrated in the following sections how, using holography and wedge shaped targets, release wave velocities can be obtained. Further refinements within the state-of-the-art should enable the whole velocity or displacement history of the release to be determined. But just the knowledge of the release wave velocity is an important and hitherto very difficult property to measure.

#### 5.1.1 Constraints of Wedge and Flyer Plate Geometries

In designing experiments in which plane shock waves are desired, the effects of release waves generated from the boundaries must be considered. There are two main classes of wave systems, catch-up and lateral release. Catch-up wave systems are a result of the flyer plate having a finite thickness and lateral release wave system are a result of the target having finite lateral dimensions.

##### 5.1.1.1 Catch-up Waves

When a flat flyer plate impacts a semi-infinite halfspace with a velocity  $V$ , two shock waves are generated.<sup>24</sup> See Figure 24. From the interface, a shock propagates into the target halfspace at a velocity  $U$  and another shock propagates into the flyer plate at a velocity  $-(U-V)$ , in the laboratory reference system. From the relations for the position

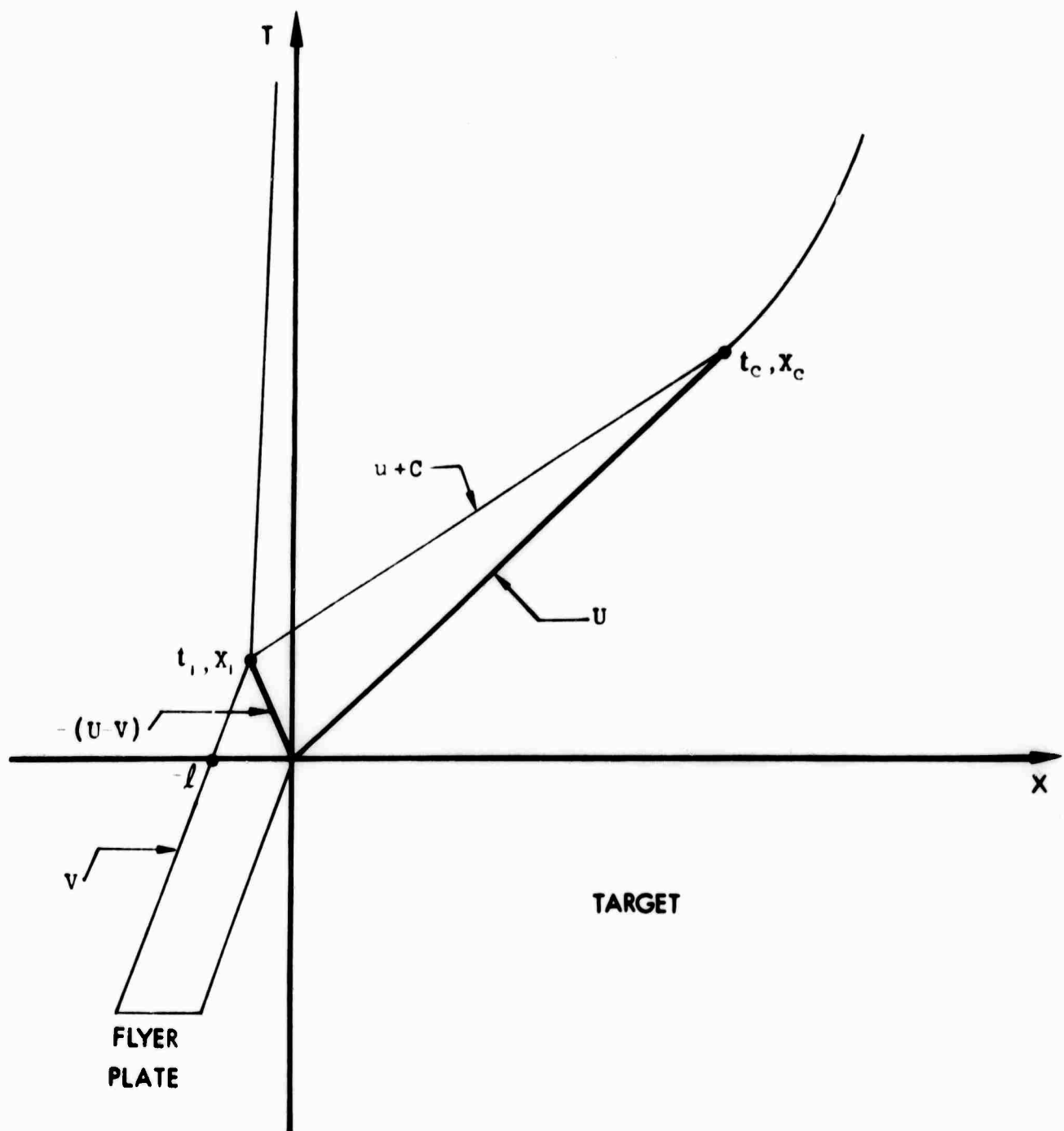


FIGURE 24 X-T DIAGRAM OF THE IMPACT OF A FLYER PLATE  
ON A TARGET HALFSpace



of the shock line and the rear of the flyer plate

$$X = -(U - V)t \quad (28,$$

$$\text{and} \quad X = Vt \quad (29)$$

we obtain the position and time of the shock when it reaches the rear of the flyer plate, they are

$$X_1 = -\left(\frac{U - V}{U}\right)\ell \quad (30)$$

$$\text{and} \quad t_1 = \frac{\ell}{U} \quad (31)$$

where  $\ell$  is the flyer plate thickness.

Upon reflection of this shock wave from the rear of the flyer plate, a rarefaction wave is generated. The head of this rarefaction wave propagates at a velocity  $u + c$  into the flyer plate and target halfspace. Since  $u + c$  is greater than  $U$ , this rarefaction release wave will overtake the shock wave and attenuate it. The equation of the release wave is

$$\frac{X - X_1}{t - t_1} = u + c \quad (32)$$

Substituting in expressions (30) and (31) we have for the position of the rarefaction wave

$$X_R = -\left(\frac{U - V}{U}\right)\ell + (u + c)\left(t - \frac{\ell}{U}\right) \quad (33)$$

If the properties of the material behind the shock wave are to be measured, it is important that measurements be made before the release wave overtakes the shock wave. The ratio of the point where this occurs to the flyer plate thickness or the ratio of target thickness to flyer plate thickness is given by

$$\frac{W}{\ell} = \frac{C+U-u}{C-U+u} \quad (34)$$

If the release wave position is known along with the shock and particle velocities, Equation (33) can be used to obtain the sonic velocity behind the shock. Solving for C we have,

$$C = \frac{X_R + \left( \frac{U-u}{U} \right) \ell}{\left( t - \frac{\ell}{U} \right)} - u \quad (35)$$

#### 5.1.1.2 Lateral Release Waves

The use of flyer plates of finite lateral dimensions places another constraint on the thickness and the geometry of the targets that can be used if plane unattenuated shock waves are desired. Consider the symmetrical impact of two semi-infinite bars, with one bar being initially at rest in the plane of impact. Two plane shock waves are generated upon impact and propagate in the axial direction along the bars. Because the surfaces of the bars are unconstrained, the passage of the shock waves generates release waves at the surfaces. The lateral release waves propagate at a velocity  $u + C$ . Because this is greater than the shock velocity  $U$ , they will gradually overtake more and more of the shock front and reduce the plane shock area. Following Al'tshuler, et.al.<sup>25</sup> the expression for the relaxation angle, which is defined as the locus of the intersection of the lateral release waves and the shock front, can be easily obtained from the triangle ABF in Figure 25. This angle is given by

$$\alpha = \tan^{-1} \frac{[C^2 - (U-u)^2]^{1/2}}{U} \quad (36)$$

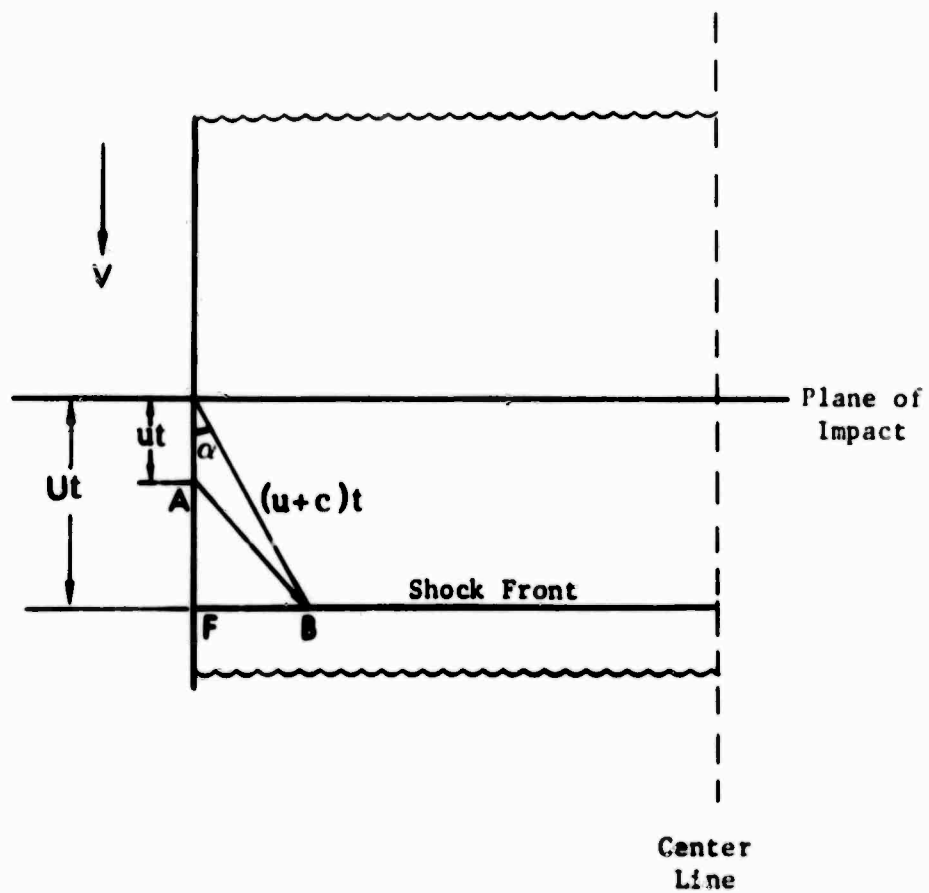


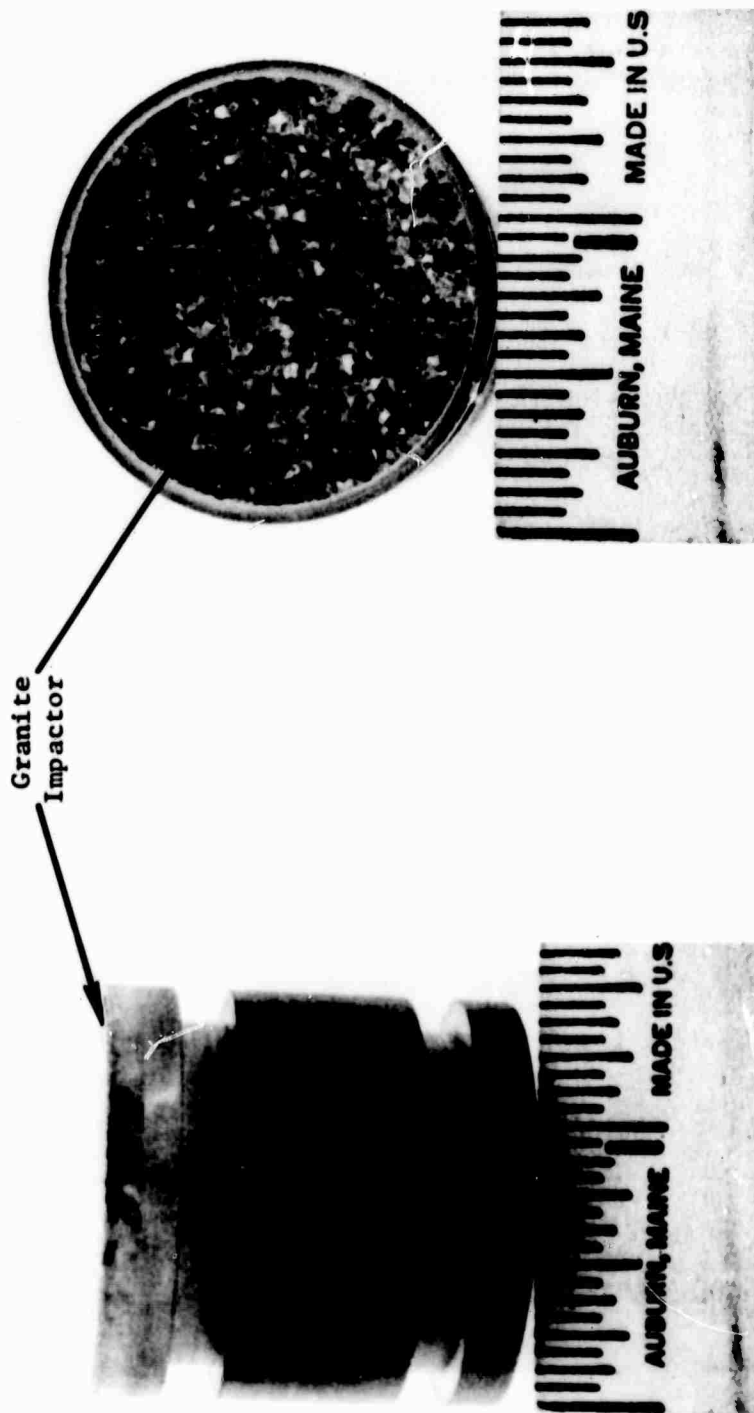
FIGURE 25 GEOMETRIC CONSTRUCTION OF THE  
LATERAL RELEASE WAVES

### 5.1.2 Experimental Facilities

TRW has two ballistic ranges which are used to support research in reentry physics, gun phenomena, and materials studies. One of these ballistic ranges provided the necessary impact facilities for this study. Ballistic Range B consists of a light gas gun. The gun is a two stage, accelerated reservoir device utilizing hydrogen to launch 1.5 inch diameter projectiles. The gun is designed to launch a 50 gram mass at 12,000 ft/sec. The gun is free to move axially in a rigid mount and is designed to launch a 1.5 inch diameter projectile such that the circular probable error at the instrumentation tank, about 40 feet from the muzzle, is less than 0.5 inch. Because of the lower projectile velocities desired for the present study, this gun was modified to serve as a pressurized air gun. The projectile was placed in the launch tube immediately in front of a mylar diaphragm. The chamber behind the diaphragm was pressurized with air. The air was fed in until the diaphragm bursts. The expanding gas accelerates the projectile down the launch tube.

The projectile consists of a 1-1/2" diameter lexan cylinder. It was designed with a cavity in front to support an impactor which served as the flat plate, (Figure 26). The cavity was designed to accommodate impactors of any desired thickness. For simplicity in analysis, the disc-shaped impactor is made out of the same material as the target thus eliminating impedance mismatch problems. O-rings are used to form a tight seal between the projectile and the launch tube.

The projectile exited the launch tube into a blast tank which was evacuated to about 1mm Hg. The projectile impacted the granite specimen inside the tank. The tank contained a large window through which the holograms could be made. All optics, with the exception of one or, in



(a) Side View

(b) Top View

Figure 26: Lexan Projectile and Granite Impactor

several of the experiments, two mirrors, remained outside the tank. A number of vacuum feed-through coaxial connectors permit electronic instrumentation of the specimen. The holographic apparatus rested on a table adjacent to the blast tank window and all other associated electronic equipment was located in this area. Figure 27 shows the gas gun, vacuum chamber and holographic apparatus.

### 5.1.3 Target Alignment

As in the pendulum experiments, the timing sequence of the pulsed ruby laser imposed constraints on the experimental technique. It is necessary to receive a fairly reliable trigger signal at least 850  $\mu$ sec before impact. The gun being used for these tests had no provisions for providing a trigger signal before the projectile left the launch tube. It was possible to instrument the mylar diaphragm, however, it was felt that the timing from this source would contain too much error. Thus, it was necessary to allow the projectile to travel approximately two feet in free flight prior to impact. This complicated the preparations necessary to insure a flat impact between the projectile and target.

The granite wedges were made by obliquely cutting a 1-1/2" diameter right cylinder of Westerly Granite (Figure 28). These wedges were then mounted on an aluminum V-block which was 7/8" long. The V-block (shown in Figure 28) was positioned and then glued to the top of a pedestal which was mounted to a positioning table. This apparatus, having adjustments about five degrees of freedom, allowed the wedge to be precisely orientated. Figure 29 shows the relative orientations of the pedestal, V-block, granite wedge with contact pins, lexan projectile and granite impactor in an "exploded" view.

The target wedge was positioned on axis with the launch tube with the impacted face perpendicular to its axis. For the short free flight

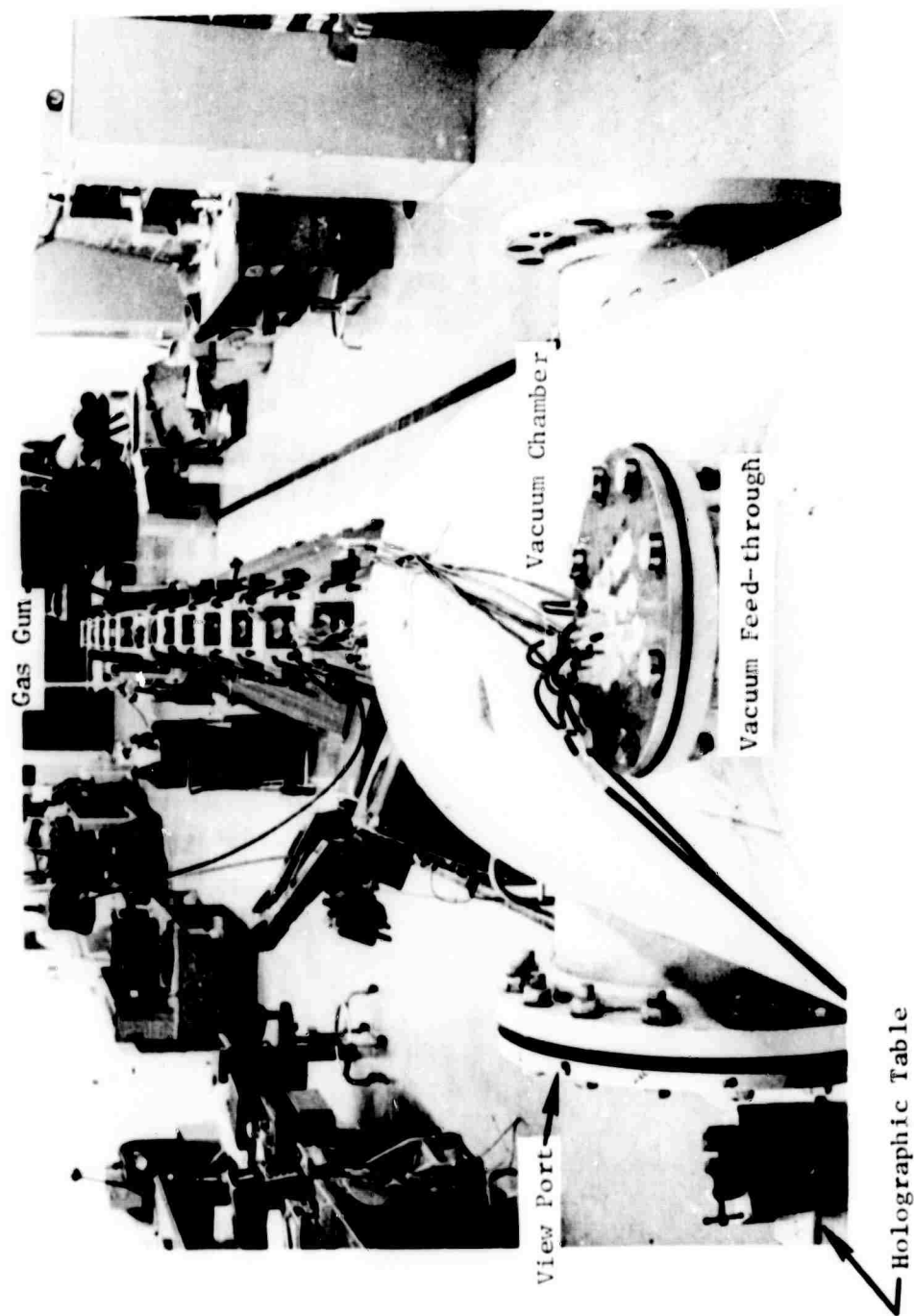


Figure 27a: Gas gun and vacuum chamber

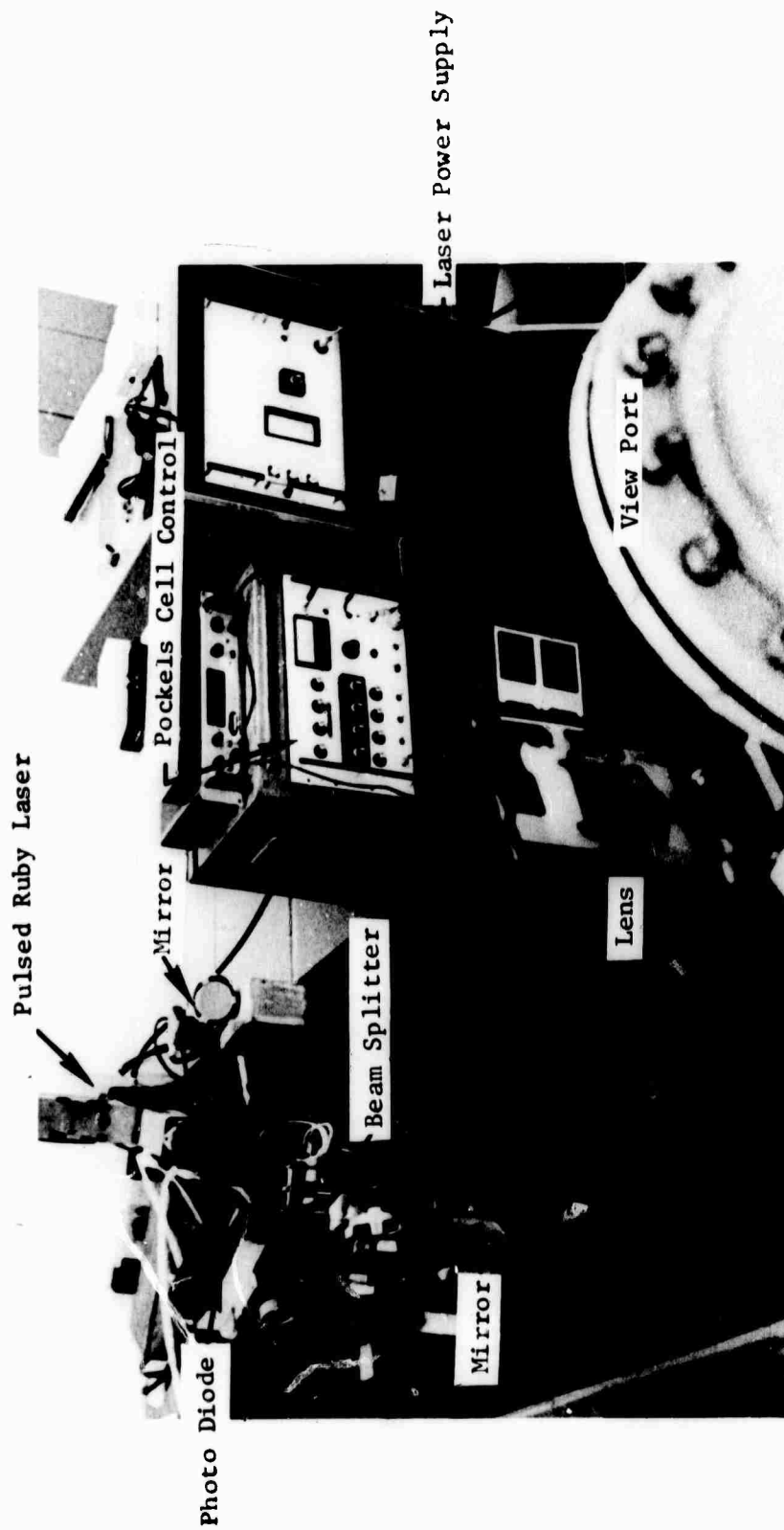
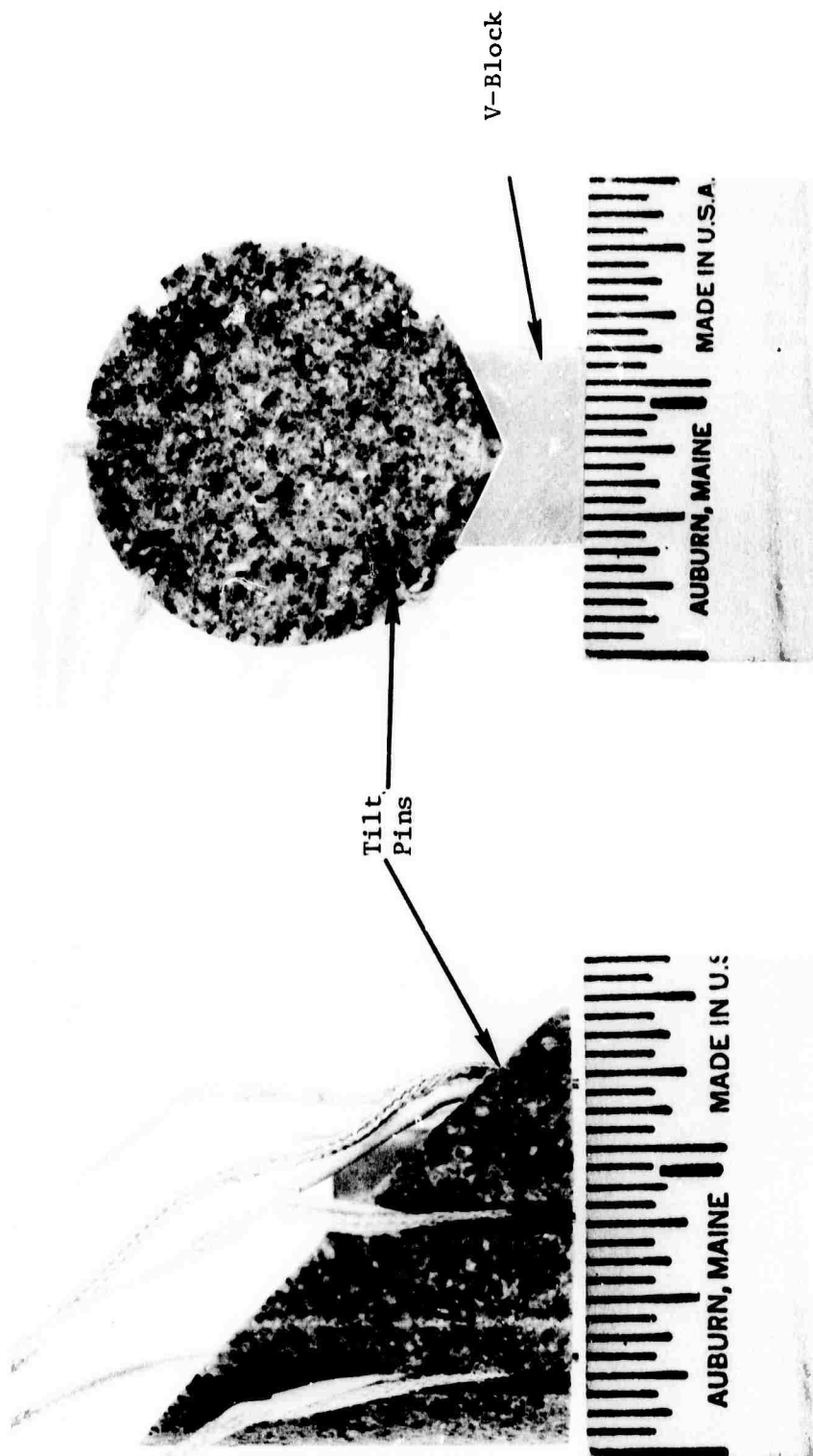


Figure 27b: Holographic apparatus





(b) End View

(a) Side View

Figure 28 Wedge-Shaped Granite Target

involved, the projectile stayed on axis and exhibited very little tilt. An alignment rod was inserted into the launch tube such that its end protruded into the blast tank and made physical contact with the target. This rod was precisely machined so that the perpendicularity of its end face to the tube axis was held to better than 2 minutes. The target was then positioned using this alignment rod. The support pedestal for the wedge was hinged so that the alignment rod could be removed. This did not affect the alignment.

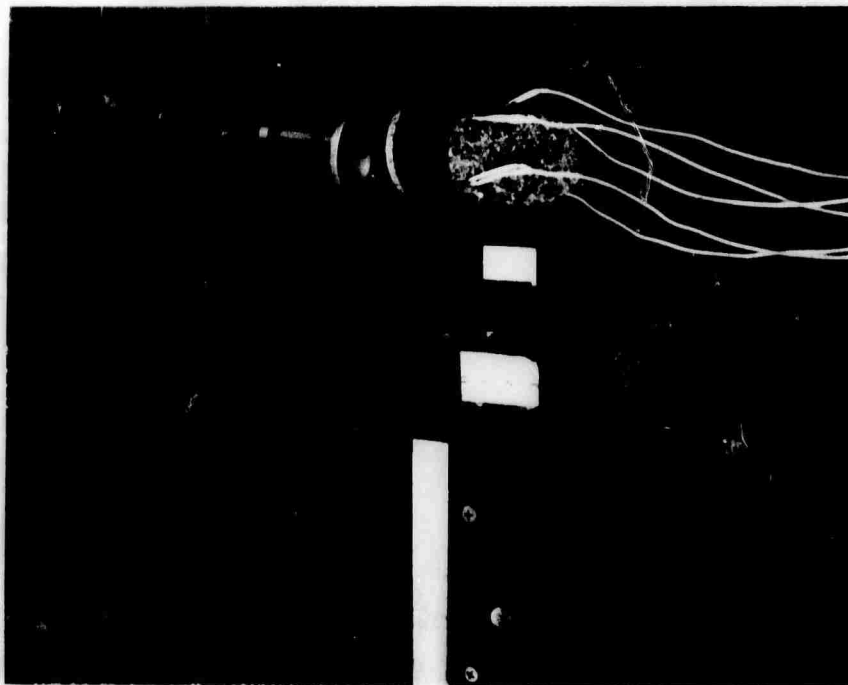


Figure 29. "Exploded" View of Impact Configuration

#### 5.1.4 Instrumentation

It was necessary to instrument the experiment to obtain the following data: projectile velocity, projectile tilt, laser pulse shape, and the time the laser pulse occurred. In addition, a signal was needed to trigger the laser flashlamp at the correct time. In order to trigger the flashlamp and to measure the projectile velocity it was

necessary to construct a device which could be triggered by the projectile in free flight. For this purpose, an open "extension" of the gun tube was constructed which provided for four trigger stations. At each trigger station, two .010" diameter wires were inserted into the path of the projectile. A thin coating of conductive paint was applied to the face of the projectile so that its contact would short circuit these wires. The wires were part of a capacitor discharge circuit (Figure 30) which provided a fast rise pulse into a 50 $\Omega$  coaxial line. The boxes containing these circuits were located inside the blast tank to minimize cable lengths.

Positioning of the wire pairs into the projectile path was facilitated by use of an alignment assembly. The launch tube extension (Figure 31) was removed from the gun and placed over the alignment assembly, (Figure 32), the base of which was machined to match the end of the gun. The center rod indicated the path of the projectile. The four rings which were situated on this rod could be moved into contact with the wire pairs and used for their alignment. The rings were locked in place when they made electrical contact with the wires. The alignment assembly was then removed with the rings still in place. When the extension was fitted to the gun, the wire pairs would protrude about 1/8" into the path of the projectile. The locations of these wires were determined by measuring the positions of the rings on the alignment assembly.

The signal from the first trigger station on the extension was made to trigger the laser flashlamp. The velocity of the projectile was estimated, and a digital delay generator used so the flashlamp would be fired  $\sim 850 \mu\text{sec}$  before impact. Signals from the other three trigger stations were used to measure the velocity and acceleration of the projectile. Two counters (with 0.1  $\mu\text{sec}$  resolution) were started by the second trigger. The third

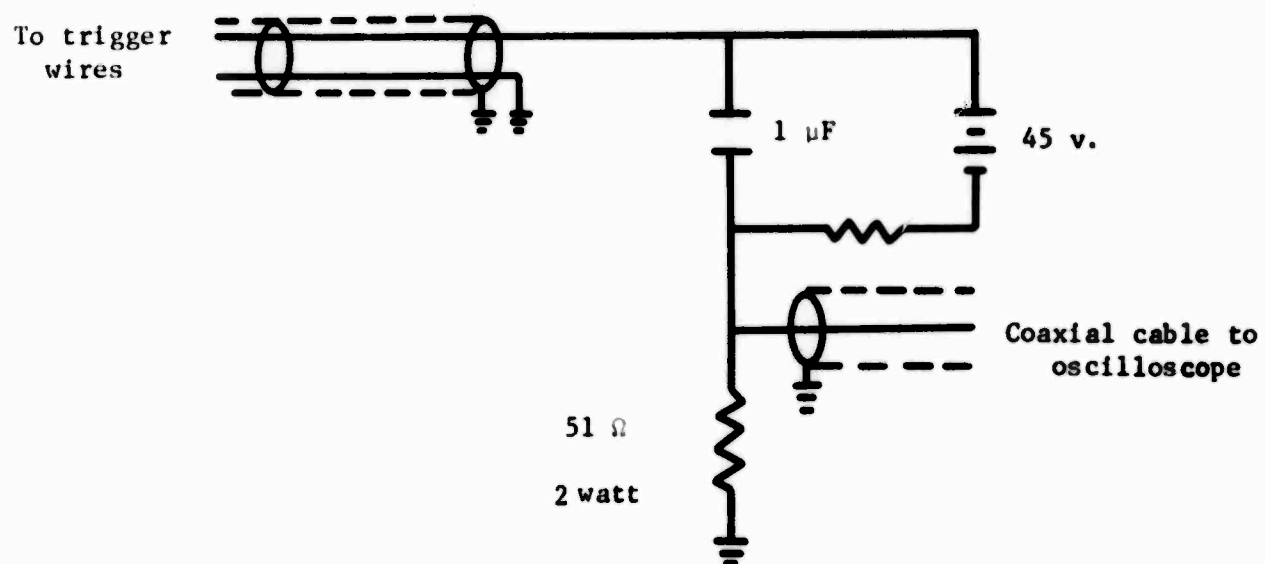


Figure 30: Capacitor discharge circuit used for trigger

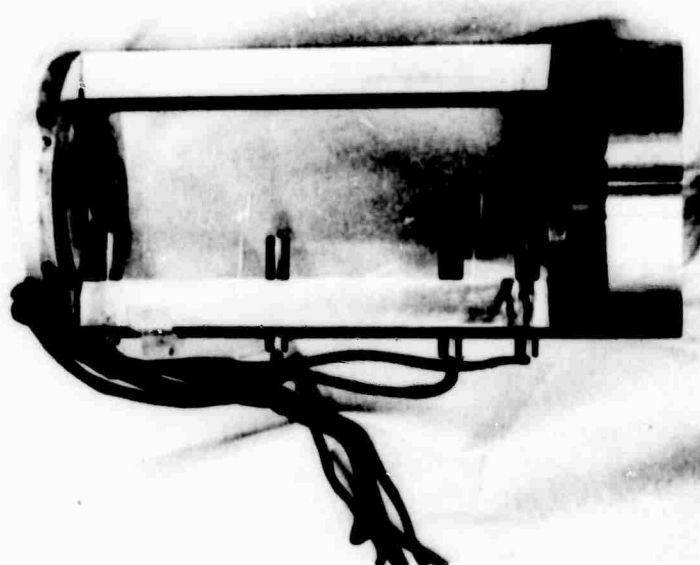


Figure 31: Lanuch tube extension with four trigger stations

and fourth triggers each stopped one of the counters, thus providing two independent measurements of the projectile's velocity. The trigger stations were spaced nominally at intervals of four inches, however, the alignment assembly made it possible to measure their positions to within one-thousandth of an inch. Thus, the velocity could be measured with 0.1% accuracy.

The tilt of the projectile was measured by means of five contact pins which were inserted into saw cuts about the circumference of the wedge, (Figure 28). E.G.&G. Inc. 32-mil ionization pins model CA-1040 were used. These pins act as a switch closure when contacted with the conductive face of the projectile. Four of these pins protruded  $\sim .025''$  (the exact positions of all pins were measured to  $.0001''$  after insertion) and their output coded to provide tilt information.<sup>26</sup> Each pin produced a different voltage signal so that it could be identified on the oscilloscope trace. The four outputs were then added and appeared on a single oscilloscope trace so that the relative times of contact for the four pins was obtained. Figure 33 shows the tilt pin coding circuit.

A fifth contact pin (labeled pin 0 in Figure 28) was located on the top of the wedge and was used to trigger the laser's Pockels cell. This pin protruded  $0.010''$  from the impacted surface and thus was contacted after the tilt pins. The delay between this trigger and the lasing was set so that the shock front would be at a predetermined position in the wedge when the hologram was made. The actual time interval between this trigger signal and the lasing was recorded on an oscilloscope. The timing of pin 0 with respect to the tilt pins was also recorded. Another oscilloscope was used to record the amplitude time-history of the laser output.

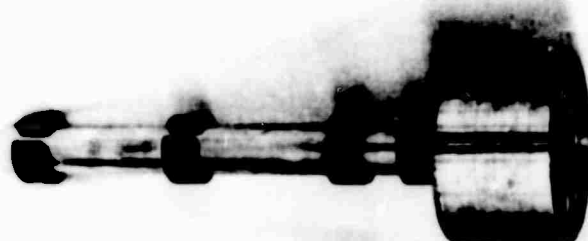


Figure 32: Alignment assembly for trigger stations

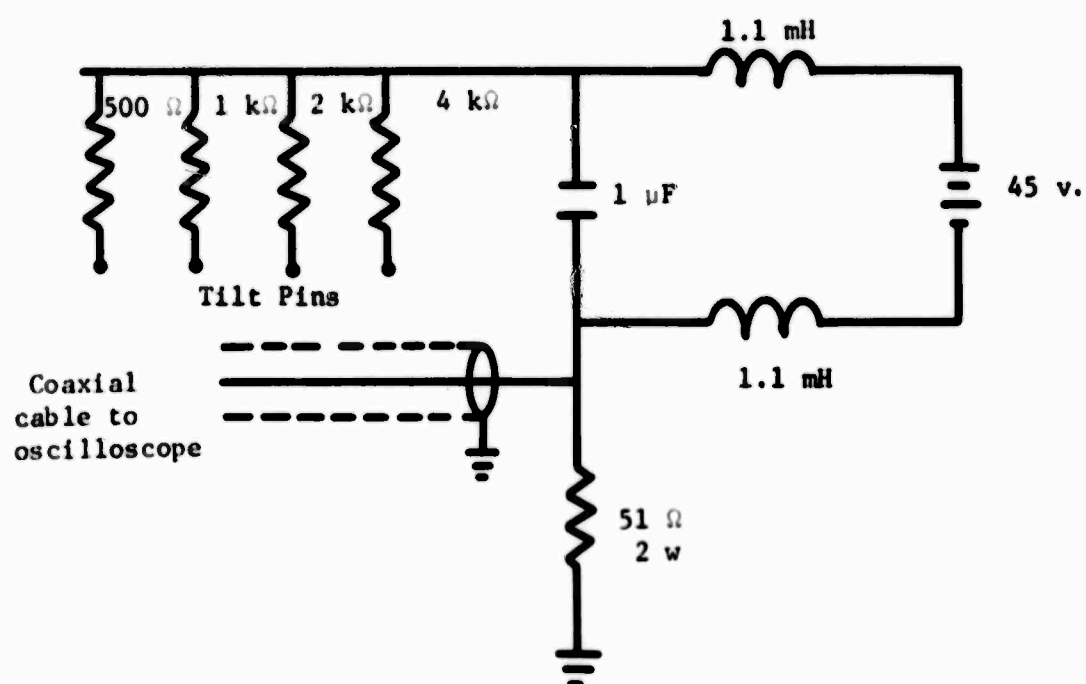


Figure 33: Tilt pin coding circuit

#### 5.1.5 Holographic Technique

The pulsed laser holographic system was set-up on a table adjacent to the blast tank which housed the impact, (Figure 27b). The holographic plate was on the table and captured the scene through the window. It was our original intent to use the double-exposure technique to record the displacement field of the wedge surface. It was discovered that the surface velocity was so high that the 50 nanosecond laser pulse was not short enough to "stop" the motion. Several holograms were made in this fashion, but upon reconstruction only the location of the shock front was discernible. Displacement information (i.e., fringes) behind the shock front was not too clear.

It was determined that the free surface velocity of the wedge was so large that the surface moved a significant distance during the 50 nanosecond exposure of the hologram and thus did not produce an image.

A second approach was adopted which takes advantage of this situation. In this case, the reference exposure is not made. The movement of the surface during the single exposure causes fringes to be formed which can be related directly to the free surface velocity of the wedge. This method is discussed in Appendix A. This single exposure technique was used for the remainder of the tests with satisfactory results.

## 5.2 Determination of the Shock Parameters from the Experimental Observables

Electronic instrumentation provides the following data: the times of flight of the projectile between known distances; and the relative time between closure of the tilt pins and the time of firing of the laser. From the photograph of the hologram, the position of the shock front and the catch-up, or following rarefaction waves are measured in the photograph coordinates. From these data and the geometry of the experiment, it is possible to determine the shock, particle and rarefaction wave velocities.

The determination of the projectile velocity and transformations from photograph to physical coordinates is straightforward and will not be discussed here. In the experiments that were performed, the projectile and target materials were identical so that the particle velocity was one half of the projectile velocity.

Figure 34 shows the wedge and the coordinate system used to describe the impact event. The shock front will appear as a straight line near the center, and will have some curvature near the edges due to release waves emanating from the free surface. Point A is defined as the intersection of the line at which the shock front intersects the wedge face and the plane formed by the horizontal axis along the center line of the wedge.  $X_s$  is the distance from the point A on the shock front to the impact surface as measured parallel to the center line of the wedge.  $X_m$  is distance from the center line of the wedge to the point A, in the horizontal plane.

The projectile tilt is measured using impact pins arranged as



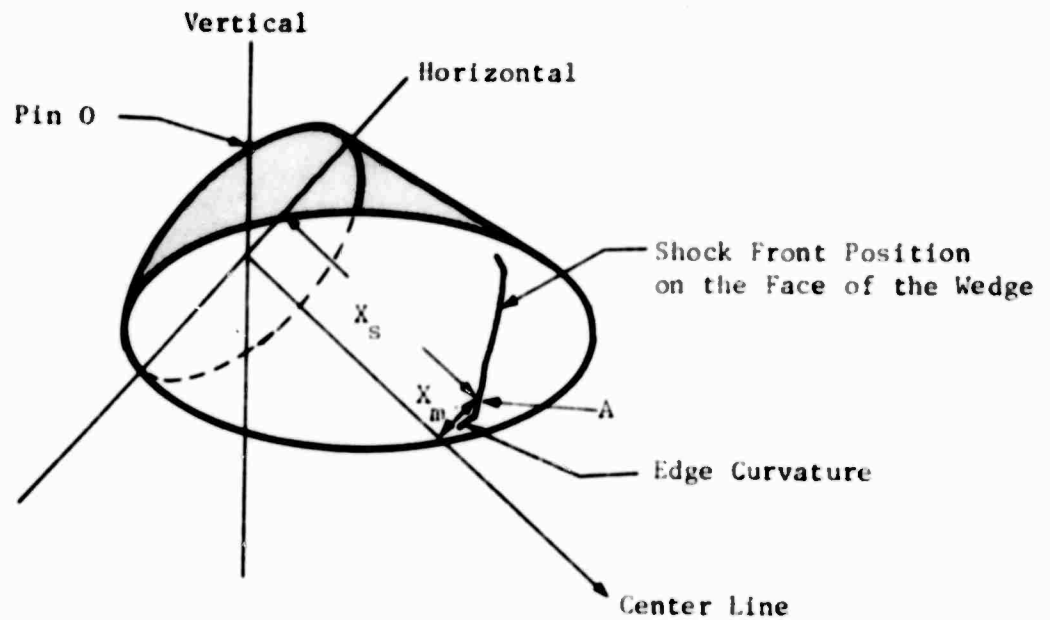


Figure 34: Wedge Geometry

shown in Figure 35. The tilt pins and the laser trigger pin are on the circumference of a circle of diameter  $d$ . The average time difference between pins A and B, and D and C is a measure of the vertical impact time difference,  $\bar{t}_v$ . The average time difference between pins A and D, and B and C is a measure of the horizontal impact time difference,  $\bar{t}_h$ . In practice, all of the pin heights are not the same so that corrections for actual pin positions, must be made in calculating these time averages. The projectile tilt is defined in terms of the vertical angle  $\theta_1$  and horizontal angle  $\theta_2$  between the normal to the projectile and the wedge center line. From figures 36 and 37 this angle is.

$$\theta_1 = \tan^{-1} \left( \bar{t}_v v / (.707d) \right) \quad (37)$$

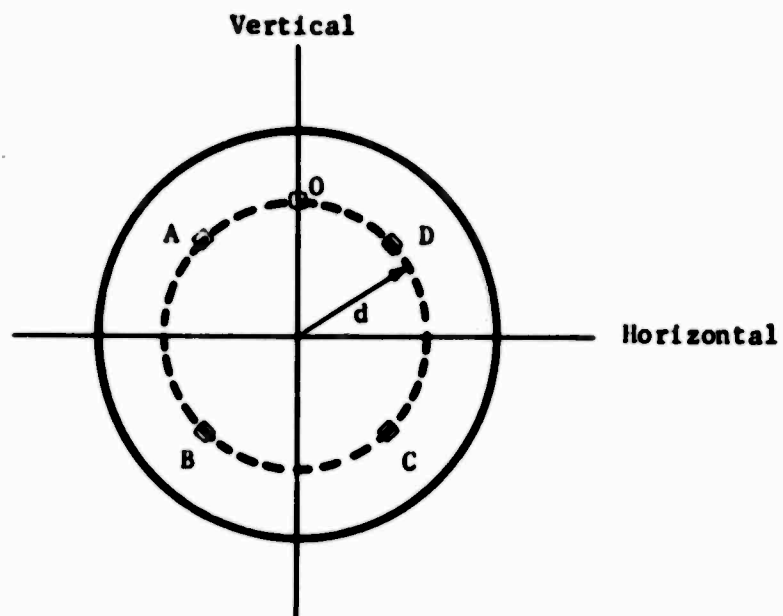


Figure 35. Tilt Pin Configuration

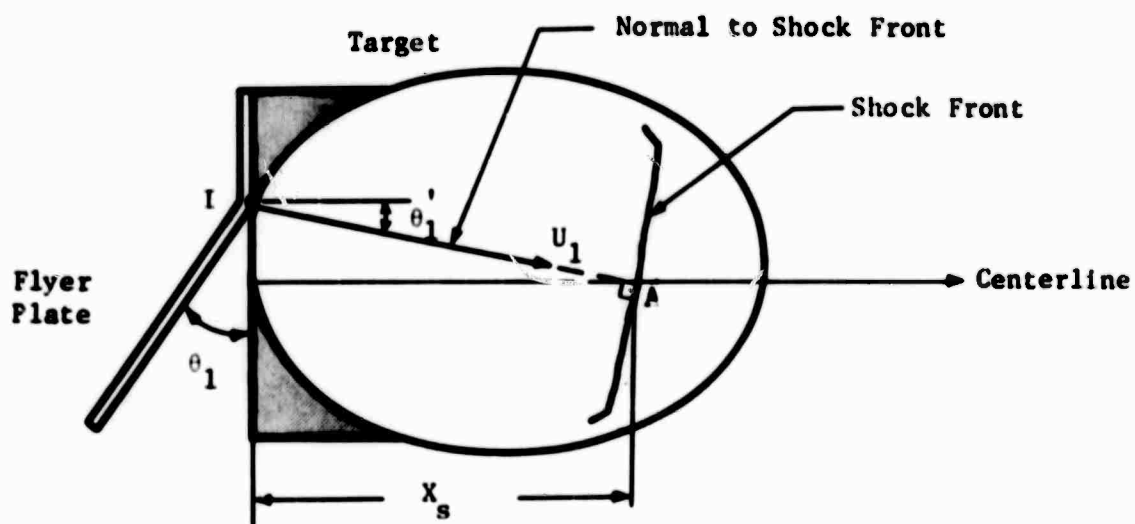


Figure 36. Vertical Section of Wedge Through Point A

and

$$\theta_2 = \tan^{-1} \left( \bar{c}_H V / (.707d) \right) \quad (38)$$

where  $V$  is the impacting projectile velocity.

The angles  $\theta_1$  and  $\theta_2$  given in equations (37) and (38) represent initial (i.e., incoming) angles of tilt. These tilt angles remain constant as the projectile impacts the target (see Figure 36), since the closure velocity of point I exceeds the sonic velocity of signals propagating in either the target or the projectile.

The index time,  $T_o$ , is taken as the time the projectile hits the target surface at the point of the location of pin "O".

$$T_o = T_m - \phi_c / V \quad (39)$$

where  $T_m$  is the time it takes for the holocamera to fire from the time that pin "O" is triggered, and  $\phi_c$  is the offset of pin "O" from the target surface.

The tilt of the shock wave will be defined in terms of the vertical angle  $\theta'_1$  and the horizontal angle  $\theta'_2$  between the normal to the shock front and the wedge centerline. Figure 36 is a vertical section of the wedge through the point A, parallel to the axis of the cylinder, and similarly, Figure 37 is a horizontal section through the point A.

The time for the shock to travel along the line I-A (see Figure 36), (where the point I is as yet not determined) is given by

$$T_1 = T_o + T_k + \frac{(X_s \tan \theta_1' \pm d/2)}{v} \tan \theta_1 \quad (40)$$

where the plus sign in the second term in the expression in parenthesis is used when the impact is on the side of the wedge opposite to pin "O" and the minus sign is used where the impact is on the tip of the wedge and

$$T_k = \pm X_m \tan \theta_2 / v \quad (41)$$

In this case the plus sign is used when the impact and the intersection of the shock front and wedge face are on the same side of the wedge centerline and the minus sign when they are on opposite sides.

The component of the shock velocity in the  $\theta_1'$  direction is given by

$$U_1 = X_s / (T_1 \cos \theta_1') \quad (42)$$

Using Figure 38, the following relation between the projectile velocity and shock velocity can be derived

$$\frac{U_1}{\sin \theta_1'} = \frac{v}{\tan \theta_1} \quad (43)$$

Eliminating the shock velocity in equations (42) and (43) we get a transcendental equation for  $\theta_1'$  in terms of measurable quantities

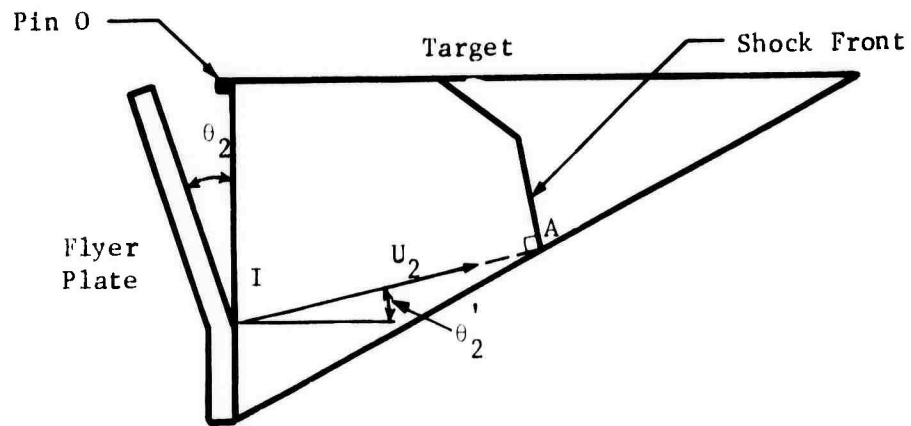


Figure 37. Horizontal Section of Wedge Through Point A

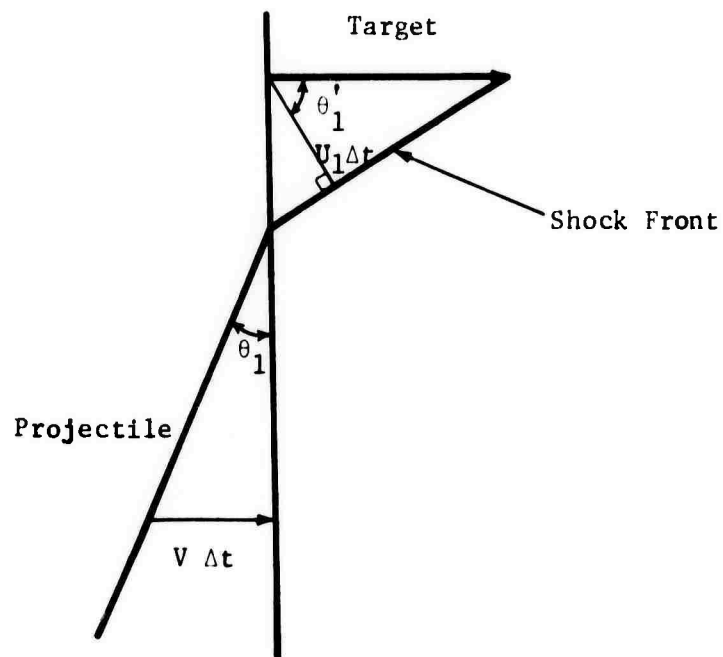


Figure 38. Geometry of Projectile and Shock Front Trajectories

$$\sin \theta'_1 = X_s \tan \theta_1 / [V \cos \theta'_1 \{T_o + T_k + (X_s \tan \theta'_1 \pm d/2) \tan \theta'_1 / V\}] \quad (44)$$

Having the value of  $\theta'_1$  one can then determine the horizontal component of the shock velocity from

$$U_1 = V \sin \theta'_1 / \tan \theta_1 \quad (45)$$

In a similar manner, the time corresponding to shock propagation along  $I' - A$  in the horizontal plane is given by

$$T_2 = T_o + T_k + \Delta T + DT_3 \quad (46)$$

where

$$DT_3 = X_s \tan^2 \theta'_2 \tan \theta_2 / V \quad (47)$$

and

$$\Delta T = \pm d \tan \theta_1 / V$$

where the plus sign is used when the projectile impacts opposite to the pin "O" and the minus sign when the impact and pin "O" are on the same side.

The  $\theta'_2$  component of the shock velocity relationship can be readily seen to be

$$\frac{U_2}{\sin \theta'_2} = \frac{V}{\tan \theta_2} \quad (48)$$

and the shock velocity in the horizontal plane

$$U_2 = X_s / (T_2 \cos \theta_2) \quad (49)$$

and again eliminating the shock velocity in expressions (48) and (49) we get a transcendental equation for  $\theta_2'$

$$\sin \theta_2' = \frac{X_s \tan \theta_2}{(V \cos \theta_2') \{T_o + T_k + (X_s \tan \theta_2' \pm d \tan \theta_1) \tan \theta_2 / V\}} \quad (50)$$

From the above solution for  $\theta_2'$  we can then obtain the  $\theta_2'$  component of the shock velocity

$$U_2 = \sin \theta_2' V / \tan \theta_2 \quad (51)$$

Combining the horizontal and vertical projections of the vectors  $U_1$  and  $U_2$  yields for the magnitude of the shock velocity

$$U = U_1 \left[ \frac{\cos^2 \theta_1'}{\cos^2 \theta_2'} + \sin^2 \theta_1' \right]^{1/2} \quad (52)$$

Once the shock velocity has been determined then the catch-up wave velocity can be calculated. Equation (35) can be used to obtain the catch-up wave velocity

$$C = \frac{X_R + \left( \frac{U - V}{U} \right) \ell}{(t_s - \frac{\ell}{U})} - u, \quad (53)$$

$X_R$  is the position of the catch-up wave and the time of travel of the shock wave is

$$t_s = X_s \left[ 1 + \tan^2 \theta_1' + \tan^2 \theta_2' \right]^{1/2} U^{-1} \quad (54)$$

If the shock wave is elastic then the particle motion with respect to normal of the wedge surface can be obtained from elasticity theory.<sup>27</sup>

This is given by

$$\cos \delta = 1 - \frac{2\nu - 1}{\nu - 1} \sin^2 \gamma \quad (55)$$

where  $\delta$  is the angle between the normal and the direction of particle motion,  $\nu$  is Poisson's ratio and  $\gamma$  is angle of incidence of the wave and the wedge face. The angle  $\delta$ , can in principle be determined holographically, and then, from equation (55), the dynamic Poisson's ratio could be determined. The free surface velocity is related to the particle velocity by

$$U_{fs} = U \frac{\sin 2\gamma}{\sin \delta \cos \gamma + \cos \delta \sin(\gamma - \delta)} \quad (56)$$

### 5.3 Experimental Results

A number of fully instrumented impact experiments were performed on 45° wedges of Westerly granite. Stress levels for these tests were in the 25-30 kilobar range. Several of these tests produced data which was amenable to complete analysis using the expressions derived in



Section 5.2. As indicated in Table III, a measurable shock tilt was observed in all our experiments. We have corrected for the shock tilt in calculating the shock and rarefaction velocities but have not taken the slight obliquity of impact into account in calculating the resulting particle velocity. The latter is extremely insensitive to small impact tilts. A summary of the results is given in Table III.

The reconstructed image of the hologram taken in experiment 13-2 is shown in Figure 39. For ease in identification, Figure 4D is included to show the reconstructed image of an unstressed wedge. Referring to Figure 39 there are four areas which can be interpreted in terms of the wave system that was propagating in the wedge. Three of the areas can be easily seen on this photograph, the fourth requires another view for maximum clarity. This fourth area is indicated on the figure. From the photograph in the figure, it is apparent that the shock wave has some tilt with respect to the centerline of the wedge. This shock tilt was measured with our impact tilt pins and found to be  $-5.42 \times 10^{-3}$  radians in the vertical direction and  $-5.85 \times 10^{-3}$  radians in the horizontal direction. The shock tilt measured by the pins in the vertical plane is consistent with that which may be seen in that plane in the photograph. Note also the curvature in the shock front at points off of the centerline of this wedge. This is due to the effects of the lateral release waves.

Starting from the tip of the wedge on the right side of the figure, the bright area is the unshocked region, the bright gray area is the region stressed by the shock wave, but not attenuated by release waves (catch-up waves) emanating from the rear of the flyer plate, the light gray area (indicated but not discernible in the reproduced interferogram)

# Results of Granite Impact Experiments

Experiment Number	13-2	14-1	17-1
Flyer Plate Thickness	.3175 cm	.3175 cm	.15875 cm
Projectile Velocity	.0353 cm/ $\mu$ sec	.0358 cm/ $\mu$ sec	.0364 cm/ $\mu$ sec
Projectile Tilt			
Vertical Tilt ( $\theta_1$ )	$-5.42 \times 10^{-3}$ radians	$-2.75 \times 10^{-2}$ radians	$2.92 \times 10^{-2}$ radians
Horizontal Tilt ( $\theta_2$ )	$-5.85 \times 10^{-3}$ "	$-9.43 \times 10^{-7}$ "	$-1.32 \times 10^{-2}$ "
Shock Position from Impacted Surface ( $X_s$ )	3.08 cm	3.80 cm	2.09 cm
Catch-up Wave Position from Impacted Surface ( $X_c$ )	2.68 cm	---	---
Lateral Release Wave			
Radial Position ( $Y_L$ )	---	---	.984 cm
Axial Position ( $X_L$ )	---	---	1.41 cm
Calculated Values			
Shock Velocity	.618 cm/ $\mu$ sec	.559 cm/ $\mu$ sec	(.559 cm/ $\mu$ sec)*
Particle Velocity	.0176 cm/ $\mu$ sec	.0179 cm/ $\mu$ sec	.0182 cm/ $\mu$ sec
Pressure	28.6 kilobars	26.2 kilobars	(26.5 kilobars)
Sonic Velocity from Catchup Wave Position	.641 cm/ $\mu$ sec	---	---
Sonic velocity from Lateral Release Wave Position	---	---	.66 cm/ $\mu$ sec
Density in Shock State	2.68 gm/cm <sup>3</sup>	2.69 gm/cm <sup>3</sup>	---
Change in Specific Internal Energy	1.55 $\times 10^8$ ergs/gm	1.59 $\times 10^8$ ergs/gm	---

\*This value was not measured but was used in calculating the lateral release wave velocity

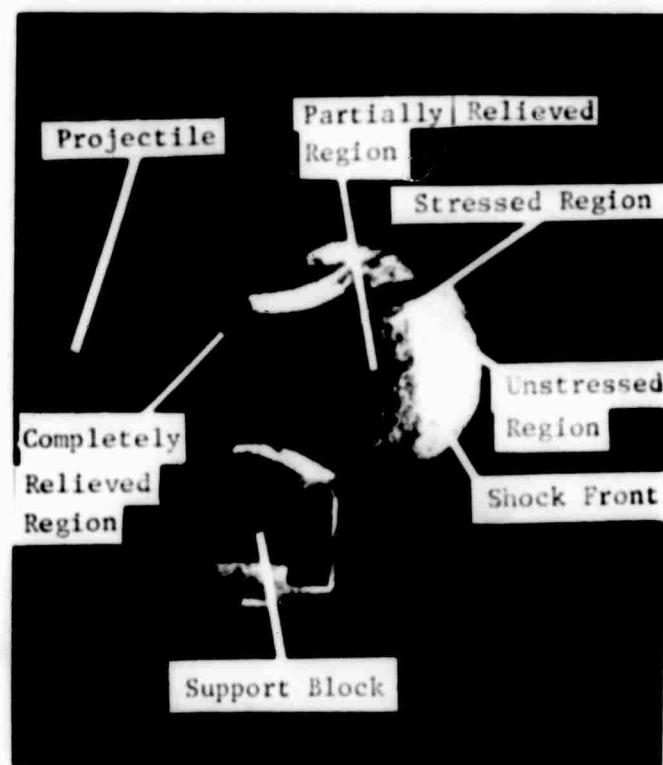


**Figure 39:** Single-exposure hologram taken in experiment 13-2 showing a granite-on-granite impact



**Figure 40:** Reconstruction of a holographic image of an unstressed wedge

is the region that has been stressed by the shock wave, but subsequent release waves emanating from the rear of the flyer plate have partially released this stress, and lastly the black area is the region that has been subjected to the shock wave and has released to very low stress levels.

Both the experimentally induced wave system and that which would be theoretically predicted are illustrated in Figure 41. The relaxation angle, which delineates the intersection of the release waves emanating from the periphery of the cylindrical surface shock front was calculated for these conditions to be  $28^\circ$ . This angle defines the region in which the shock front remains plane and unattenuated. The wedge angle in these experiments was chosen to be  $45^\circ$ , so that the closure velocity of the shock wave with the wedge surface exceeded the release wave velocity and therefore disturbances emanating from the intersection of the impact plane and the wedge face could not interact with the shock front.

The shock velocity was calculated from the position of the shock along the centerline and the time of fire of the laser system. The method of analysis was given in Section 5.2.

The shock velocity was found to be  $.618 \text{ cm}/\mu\text{sec}$ . Since both the flyer plate and target were granite, the particle velocity behind the shock wave was one-half of the impact velocity. Therefore the particle velocity was  $.0176 \text{ cm}/\mu\text{sec}$ . The stress in the shock wave using these values was computed and found to be 28.6 kilobars. The above values of particle velocity and stress compare favorably with the values of  $.01735 \text{ cm}/\mu\text{sec}$  for the particle velocity at 27.20 kilobars found by Jones and Froula<sup>28</sup>. For westerly granite this stress is less than the Hugoniot elastic limit; therefore, a single elastic shock would be expected to occur. This is

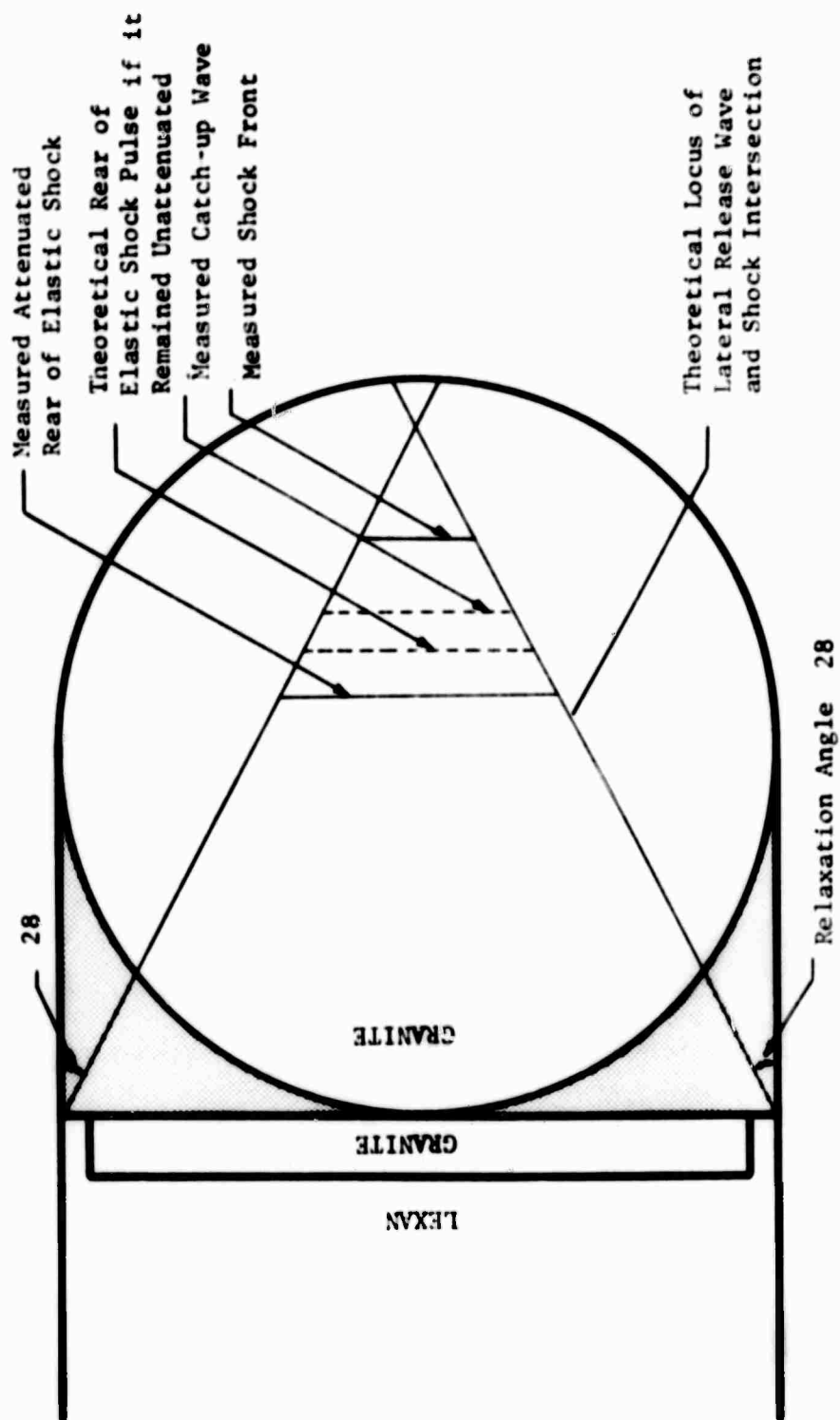


Figure 41. Side View (Normal to Wedge Axis) of the Wave Positions in Granite in Experiment 13-2

consistent with the photograph of the hologram. The Hugoniot data reported in these experiments compared closely with those reported by Jones and Froula.<sup>28</sup> (See Figure 42)

The flyer plate thickness in this experiment was chosen so that release waves emanating from the rear of the flyer plate would overtake a significant fraction of the shock pulse so that release wave position and velocity data could be obtained. This release wave position is indicated in the photograph of the hologram (Figure 39) and illustrated in Figure 41. Having knowledge of the shock and particle velocities and release wave position, one is able to calculate the sonic velocity behind the shock wave. (See Equation 53). Using the values of the shock parameters found in this experiment, the calculated value of the sonic velocity is .64 cm/ $\mu$ sec. Simmons and Brace<sup>29</sup> found the sonic velocity to be .6252 cm/ $\mu$ sec at a hydrostatic pressure of 10 kilobars. It appears from the work of Tocher<sup>30</sup> that the maximum compressional stress determines the measurable sonic velocity in rocks. Thus, although the principal stress configuration under one-dimensional compression differs from the hydrostatic case, the measured sonic velocities should be comparable. Taking the possible stress configuration differences into account, the measured value of .64 cm/ $\mu$ sec is commensurate with an equivalent hydrostatic pressure of 30 kilobars.

The reconstructed image of the hologram taken in experiment No. 14-1 is shown in Figure 43. In this event the position of the shock front is interpreted as having just reached the tip of the wedge when the laser fired. The catch-up wave position is not discernible in the photograph. The shock velocity was found to be .56 cm/ $\mu$ sec and the particle velocity .0179 cm/ $\mu$ sec. The pressure from these values was 26.2 kilobars. These

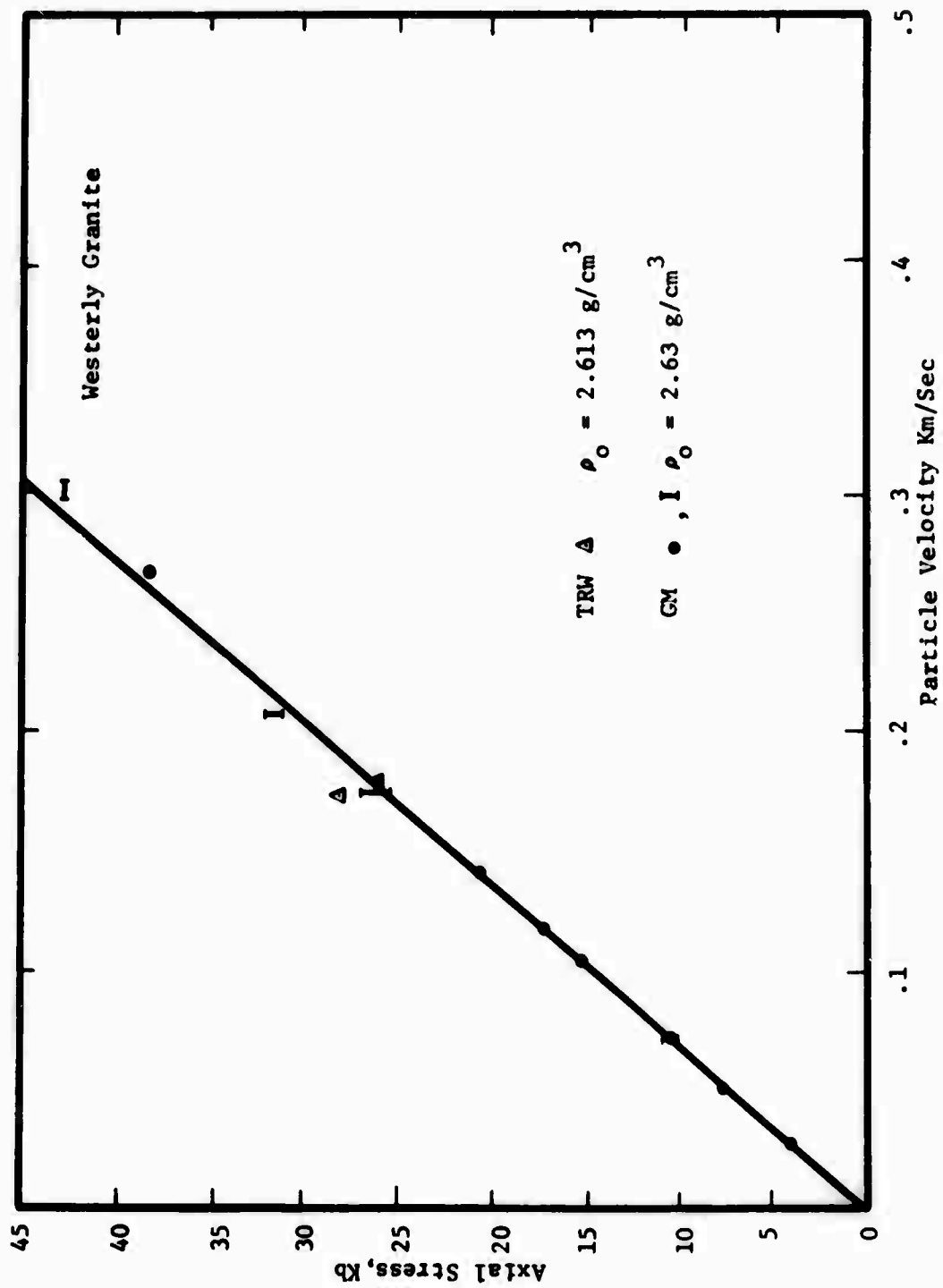


Figure 42: HUGONOT FOR WESTERLY GRANITE

values compare favorably with the values of .56 cm/ $\mu$ sec at 25.22 kilobars reported elsewhere<sup>28</sup>.



Figure 43: Interferogram of a stress pulse propagating in a Granite wedge (Exp. No. 14-1)

The reconstructed image of the hologram in the experiment No. 17-1 has several interesting features. (See Figure 44.) The shock wave clearly has a large tilt. The tilt was accurately predicted by the pin timing data. Another feature is the break in the shock front from the effects of lateral release waves. From the position of this break, the sonic velocity of material behind the shock wave can be calculated. Problems were encountered when the shock velocity for this case was calculated and a consistent value could not be obtained. By assuming the value of the



shock velocity in this experiment scaled with the value found in experiment No. 14-1, a sonic velocity from the lateral release wave position could be calculated. This value was found to be .66 cm/ $\mu$ sec.

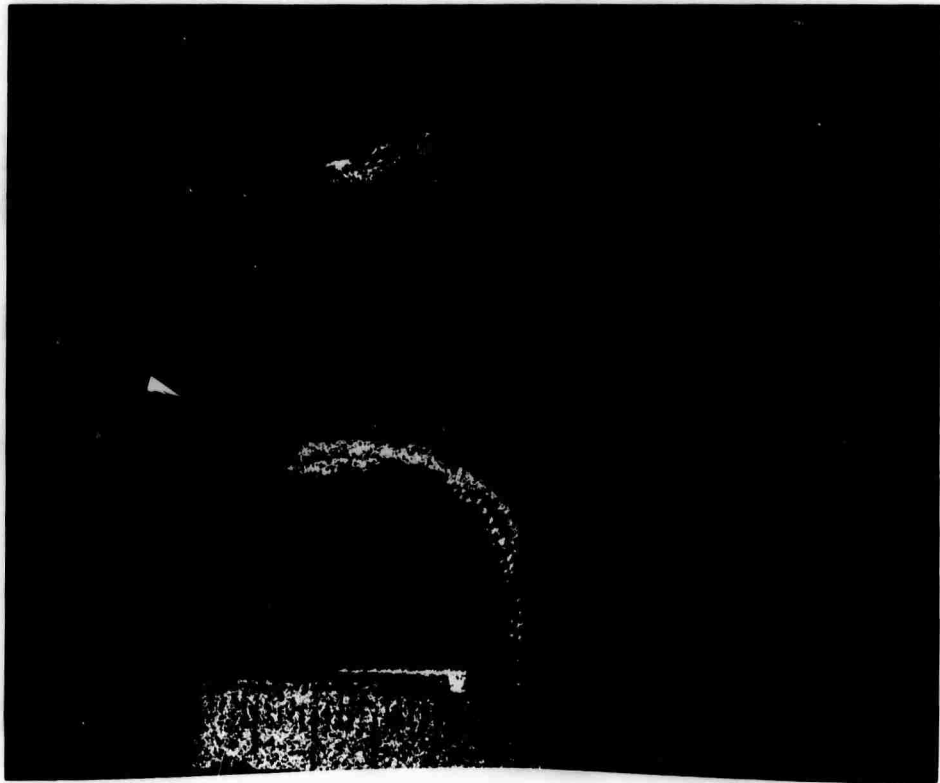


Figure 44: Interferogram of a stress pulse propagating in a Granite wedge (Exp. No. 17-1)

The above cases have demonstrated how time average holographic interferograms producing fringes relating to velocities can be used to obtain the shock, catch-up and lateral release wave positions. From

this information, the shock velocity and sonic velocities were calculated. In principle, the catch-up wave and lateral release wave velocities can be measured for a given event, therefore sonic velocity in two different directions can be measured simultaneously and the degree of anisotropy in the sonic velocity induced by the uniaxial straining of the shock wave can be determined. The full capability of the time averaged holographic interferometry technique has not been exploited. Besides the wave front positions, the complete three-dimensional velocity field can be, in principle, measured. Presently this is a difficult measurement, because the resulting fringe density was found to be a sensitive function of the holocamera viewing angle that was used. But this difficulty can be resolved by refinement of the technique. It was previously mentioned that the double-exposure holographic interferometry technique could not be used since the shock front and material particle movement was too large for the laser pulse widths of 50 nanoseconds. Subsequent to the performing of these experiments, we developed the capability of producing nanosecond laser pulses. With this capability, the double-exposure technique now appears to be a promising technique to measure the displacement field. Therefore, the holographic techniques mentioned have the capability of measuring either the displacement or the velocity fields directly.

#### 5.4 Determination of the Sonic Velocity in the Shocked Material by the Use of Lateral Release Waves

In designing experiments to measure shock wave parameters, configurations are usually chosen to minimize the effects of release waves, e.g. one-dimensional. However, measuring these effects can sometimes provide useful data. It was previously stated that release waves are primary in determining the attenuation rate of shock waves, but they also have another fundamental use in shock wave experiments. They provide a separate and important measure of the material properties in the shocked state. If the material behaves hydrodynamically, then the bulk sonic velocity, or the slope of the isentrope, in the shock state can be obtained. If the material exhibits finite strength, then besides the above information, the degree of rigidity can be determined. Materials which undergo phase changes may lose their initial rigidity upon transition. The release wave provides a measure of this effect. For porous or locking solids, the degree of rigidity in the collapse state can be determined. At low stress levels, friction on crack surfaces plays an important role in determining the release path and rate.

Previously an expression for the relaxation angle was derived, i.e., the locus of the intersection of the lateral release waves and the shock front. If this angle is measured along with the shock and particle velocities, then the sonic velocity behind the shock wave can be determined. From equation 36, we have for the sonic velocity

$$C_{LR} = [D^2 \tan^2 \alpha + (D - u)^2]^{1/2} \quad (57)$$

A preliminary experiment was carried out using aluminum to show the feasibility of the technique. A single exposure hologram was taken of the impact event. Figure 45 shows a photograph of the hologram and Table IV summarizes the conditions of the experiment.

TABLE IV  
Experimental Parameters

Type of Interferometry	Time Average
Target Material	Aluminum 2024 T6
Projectile Material	.125" Aluminum 2024 T6
Projectile Velocity	1175 ft/sec
Projectile Tilt	NA
Exposure Time	4.3 $\mu$ sec after impact
Pressure	29 kilobars

Referring to Figure 45, five distinct areas are evident, labeled a, b, c, d, and L. Area a corresponds to the part of the target ahead of the stress pulse; area b corresponds to the elastic precursor; area c corresponds to the plastic shock and d the area enveloped by the catch-up wave. The areas L are the regions encompassed by the lateral release waves. The positions of the heads of the lateral release waves are at the kinks in the fringes delineating regions c and d. These positions were measured and a relaxation angle was determined. The sonic velocity behind the shock wave from this value was  $.68 \pm .03$  cm/ $\mu$ sec. This value is in excellent agreement with the theoretical value of .68 cm/ $\mu$ sec at 29 kilobars calculated by Pastine and O'Keefe<sup>31</sup>.

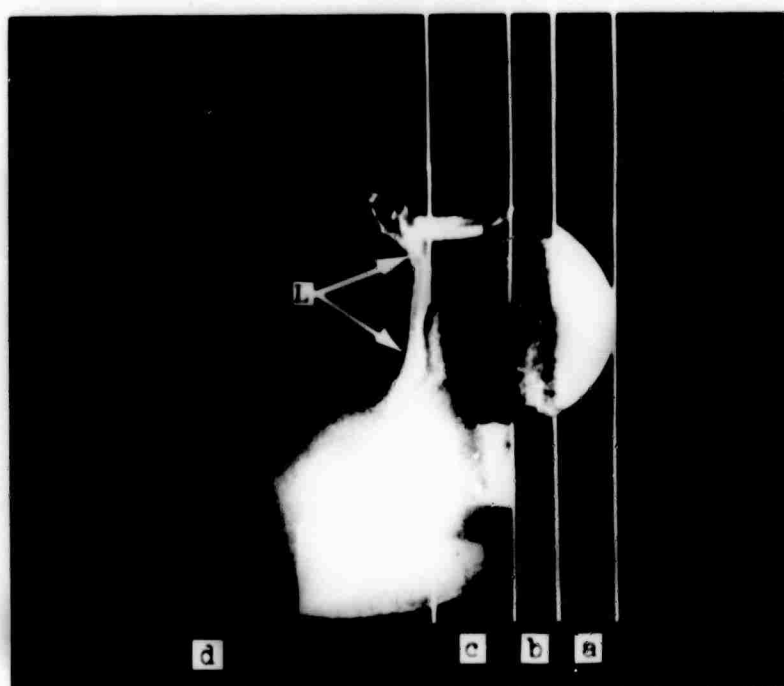


Figure 45: Shock and Release Wave Positions  
in a Stressed Aluminum Wedge

## 6.0 SUMMARY AND CONCLUSIONS

A series of stored-beam, double-exposure and time-average holographic interferometric techniques have been developed to carry out equation of state measurements on geologic materials. This development of holographic measurement techniques achieved a major objective of the study. Now that the feasibility of these methods has been demonstrated, similar measurements can be made in more extensive test programs. It should be recognized that these techniques are still in the early stages of development, moreover, they can be refined to yield much more extensive and accurate data than that presented herein.

Of particular significance from a holographic standpoint is the "holographic velocity interferogram" introduced herein for the high-pressure experiments. The velocity interferogram is a form of time-average holography where the average is taken over the pulse duration of the laser. Another holographic development was the simultaneous measurement of longitudinal (in-plane) and radial (out-of-plane) deformations by double-exposure holography. These new techniques can be applied to a wide variety of structural response problems and constitute the most significant contribution of this study.

The major advantage of this technique over conventional forms of interferometry is that it does not require that the specimen surface receive any special treatment or preparation. Other forms of interferometry require a specular reflection of light whereas holography actually works better with a rough surface which reflects diffusely. Another advantage is that holography is a noncontacting measuring technique. No sensor need be attached to the object which may actually alter the event being recorded.

Using the time average holographic interferometry technique, shock wave measurements were carried out initially on a series of 2024 aluminum, and later on a series of Westerly granite specimens using plane shock, one-dimensional compression techniques. Wedge-shaped samples permitted the observation of the shock, high pressure region and onset of the rarefaction wave in a single exposure hologram. A compressed gas gun was used to obtain shock pressure on the order of  $\sim 30$  kb in both materials. In the case of Westerly granite, Hugoniot states were obtained in the vicinity of 30 kb. These results indicate that this stress level is below the Hugoniot elastic limit for this material. The resulting data agree closely with those reported by Jones and Froula<sup>28</sup>. The velocity of the rarefaction waves propagating into the granite shocked to this pressure level could be measured in the same series of experiments. Three determinations of the release wave velocity, one obtained by the lateral relaxation method, gave unloading velocities of between .64 and .66 cm/ $\mu$ sec. These values indicate that the material is unloading as an elastic solid, rather than behaving hydrodynamically upon dynamic stress release. A velocity of .45 cm/ $\mu$ sec would be obtained if the latter rheological description were appropriate. A similar measurement of the lateral relaxation velocity in 2024 Al at a shock pressure of 29 kb gives a speed of  $.68 \pm .03$  cm/ $\mu$ sec. In this case the aluminum was shocked above the Hugoniot elastic limit into the deformation regime and this material was unloading as an elasto-plastic solid. This longitudinal elastic velocity also agrees closely with the theoretical results of Pastine and O'Keefe<sup>30</sup>.

A series of one-dimensional stress experiments on granite and aluminum rods carried out with double-exposure holographic interferometry permitted measurement of the spatial distribution of the dynamic longitudinal and transverse deformation induced by a projectile impact at one end of the rod. The experimental data were in qualitative agreement with elementary plane stress theory, and it is felt that three-dimensional effects (such as non-planar wavefronts) account for the quantitative differences.

With the stored beam holographic method, a series of low stress level one-dimensional stress experiments were carried out on rods of Westerly granite. In these experiments, a holographic interferometer measured the displacement of the end free surface of the granite rod. Stress pulses of 5 bar amplitude, with strain rates of  $10^{-1}$ /sec, were induced into the rod by a low velocity impact. We found that the dynamic Young's Modulus under these conditions was  $0.53 \pm 0.01$  Mbar. This was slightly higher than the value of  $0.50 \pm .002$  Mbar measured in a separate static compression test. At this stress level, which is low, by shock standards, but considerably higher than those normally induced in ultrasonic measurements ( $\sim 10^{-3}$  dynes/cm<sup>2</sup>) the dry granite behaved as a high Q material. We found a lower bound to the attenuation coefficient of  $3 \times 10^{-4}$  nepers/cm. This corresponds to a Q value greater than 78.



## REFERENCES

1. "Handbook of Physical Constants," published by the Geological Society of America, Inc., S. P. Clark, Jr., Editor, 1966.
2. Pochhammer, L., Journal für Mathematik (Creele) Bd 81, 1876, p. 234.
3. Chree, C., "The Equations of an Isotropic Elastic Solid in Polar and Cylindrical Coordinates, Their Solution and Application," Trans. of Cambridge Phil. Society, Vol. 14, 1889, p. 251-369.
4. Bancroft, D., "The Velocity of Longitudinal Waves in Cylindrical Bars," Phys. Rev., New York, Vol. 59, 1941, p. 588.
5. Jones, O. E. and Norwood, F. R., "Axially Symmetric Crosssectional Strain and Stress Distributions in Suddenly Loaded Cylindrical Elastic Bars," Trans. ASME, J. Appl. Mechanics, Vol. 34, Series E, Sept. 1967.
6. Kennedy, L. W. and Jones, O. E., "Longitudinal Wave Propagation in a Circular Bar Loaded Suddenly by a Radially Distributed End Stress," J. of Appl. Mech., Paper No. 69-QPMW-4.
7. Bertholf, L. D., "Numerical Solution for Two Dimensional Elastic Wave Propagation in Finite Bars," J. Appl. Mech., Vol. 34, Series E, No. 3, p. 725, Sept. 1967.
8. Bertholf, L. D. and Karnes, C. H., "Asymmetric Elastic-Plastic Wave Propagation in 6061-T6 Aluminum Bars of Finite Strength," J. Appl. Mech., Paper No. 69-APMW-18, 1969.
9. Davies, R. M., "A Critical Study of the Hopkinson Pressure Bar," Phil. Trans. of Royal Soc., London, Series A, Vol. 240, 1948, pp 375-457.
10. Cristescu, N., "Dynamic Plasticity," North Holland Publishing Company (1967), p. 119.

11. Bell, J. R., "Physics of Large Deformation of Crystalline Solids," Springer Tracts in Natural Philosophy, Vol. 14, 1968.
12. Grine, D. R., "Dynamic Strength of Rocks," 29th Symposium on Shock, Vibration and Associated Environments, Nov. 15-17 (1960), p. 136.
13. Ito, I. and Terada, M., "Stress Waves and Dynamic Characteristics of Rocks Under Detonators Attack," Symposium on the Behavior of Solids Under High Dynamic Pressure, Proc. Paris, 11-15 Sept. 1967.
14. Courant, R. and Friedrichs, K. O., "Supersonic Flow and Shock Waves," Interscience Publishers, Inc. (1948).
15. Coleman, B. D., Gurtin, M. E., Herrera, I., and Truesdell, C., "Wave Propagation in Dissipative Materials," Springer-Verlag, New York (1965).
16. Truesdell, C. and Noll, W., "The Non-Linear Field Theories of Mechanics," Encyclopedia of Physics, Vol. III/3, Springer-Verlag (1965).
17. Truesdell, C. and Toupin, R. A., "The Classical Field Theories," Encyclopedia of Physics, Vol. III/1, Springer-Verlag (1960).
18. Walsh, J. M., Rice, M. H., McQueen, R. G. and Yarger, F. L., "Shock Wave Compression of Twenty-seven Metals, Equations of State of Metals," Phys. Rev. Vol. 108, No. 2 (Oct. 15, 1957).
19. Barker, L.M., "SWAP - A Computer Program for Shock Wave Analysis," Sandia Corporation Report SC-BR-4769 (1963).
20. Cowperthwaite, M. and Ahrens, T. J., "Thermodynamics of the Adiabatic Expansion of a Mixture of Two Phases," Am. J. Phy., 35, 951 (1967).
21. Ahrens, T. J., Anderson, D. L. and Ringwood, A. E., "Equations of State and Crystal Structures of High Pressure Phases at Shocked Silicates and Oxides," Rev. of Geophysics, 7, 667 (1969).

22. Aprahamian, R. and Piechocki, J., "Theoretical Analysis of One-Dimensional Impact Including Elastic/Plastic Effects," LMSC, Hardening Technology Studies, Vol. V, Final Report, LMSC-B130200, 1966.
23. Jones, A. H., Isbell, W. M. and Maiden, C. J., "Measurement of Very High Pressure Properties of Materials Using a Light Gas Gun," Jour. Appl. Phys., Vol. 37, No. 9, Aug. 1966.
24. Fowles, G. R., "Attenuation of the Shock Wave Produced in a Solid by a Flying Plate," J. Appl. Phys., 31(4), 655 (1960).
25. Al'tshuler, L. V., Kormer, S. B., Brazhnik, M. J., et al, "The Isentropic Compressibility of Aluminum, Copper, Lead and Iron at High Pressures," Soc. Phys., JETP 11, 766 (1960).
26. Linde, R. K. and Schmidt, D. N., "Measuring the Submicrosecond Response of Shock Loaded Materials," Rev. Sci. Inst. 37, 1 (1966)
27. Ewing, W. M., Jardetzky, W. S. and Press, F., "Elastic Waves in Layered Media, p. 27 (McGraw-Hill, New York, 1957).
28. Jones, A. H. and Froula, N. H., "Uniaxial Strain Behavior of Four Geological Materials to 50 Kilobars, "DASA-2209-MSL-68-19.
29. Simmons, G. and Brace, W. F., "Comparison of Static and Dynamic Measurements of Compressibility of Rocks," Jour. Geophy. Res. 70, p. 5649 (1965).
30. Tocher, D., "Anisotropy in Rocks Under Simple Compression," Trans. Am. Geophy. Union, 38, 89 (1957).
31. Pastine, D. J. and O'Keefe, D. J., "Theoretical Estimates of Elastic Release Wave Velocities for Metal with Applications to Al and Cu," Jour. App. Phy. 41, 2743 (1970).

## APPENDIX A

### A.0 HOLOGRAPHIC TECHNIQUES

#### A.1 Image Recording and Reconstruction

The recent development of holography has made practical a new type of interferometry. Precise displacement measurements can be made over the surface of an object by holographically recording its complete three-dimensional image. A brief review of the holographic process would be helpful in understanding its capabilities.

Holograms are made using coherent, monochromatic light sources, the best known of which is the laser. The light from the laser serves both to illuminate the object whose image is to be recorded and to provide a reference beam. Figure A.1 shows schematically a typical set-up used to obtain holograms of optically opaque objects.

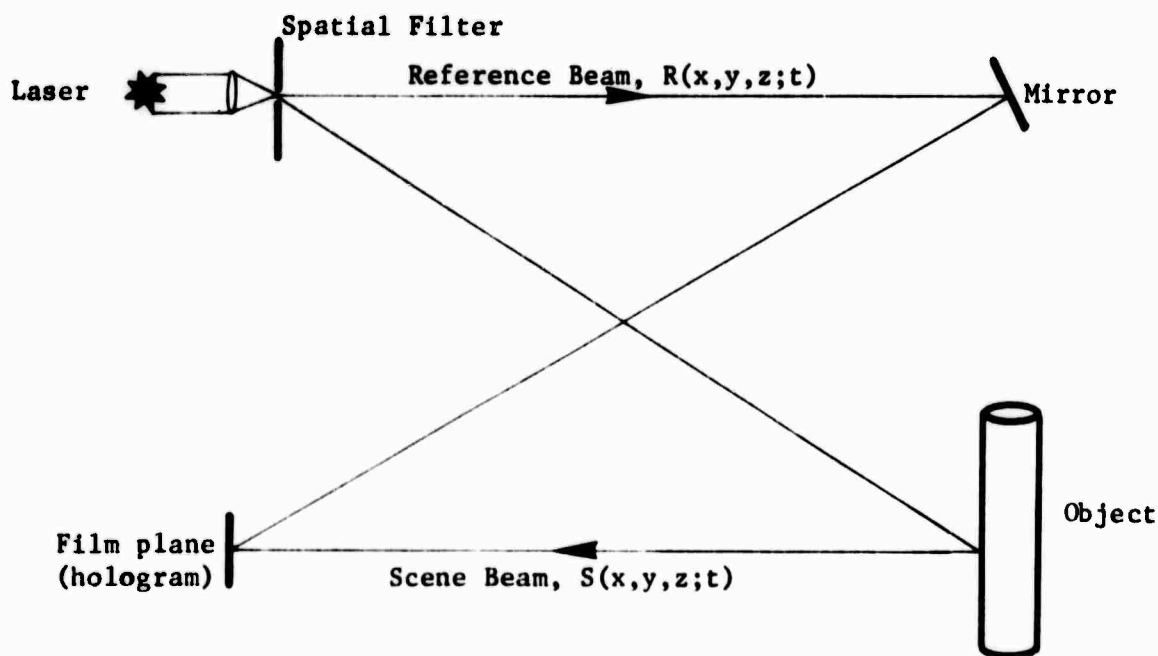


Figure A.1: Typical experimental setup to make holograms of optically opaque objects

Referring to Figure A.1, a narrow pencil of light from the laser enters a spatial filter consisting of a lens and pinhole. The function of the lens is to focus the light in the plane of the pinhole and to diverge the narrow beam. The pinhole spatially filters the light by removing any aberrations caused by the lens. The expanding light illuminates a mirror and the object. Part of the light is reflected by the mirror onto the film plane (reference beam). Light reflected by the object (scene beam) also propagates back to the film plane where it interacts with the reference beam. This interaction is recorded by the film forming a hologram. The interaction of the scene beam with the reference beam is amenable to analysis.

Denote by  $R(x,y,z;t)$  and  $S(x,y,z;t)$  the amplitude of the reference and scene beams, respectively. One may separate these functions into spatial and temporal components

$$R(x,y,z;t) = r(x,y,z)e^{i\omega t}$$

$$S(x,y,z;t) = s(x,y,z)e^{i\omega t}$$

The film responds to the intensity,  $I$ , of light reaching it. The intensity is in turn given by the square of the modulus of the light amplitude, i.e.,

$$I = |A|^2 = |R + S|^2 \quad (A.1)$$

where  $| |$  denotes absolute value. Since the film is exposed to the light for a finite time,  $t_E$ , its exposure,  $E$ , is given by<sup>†</sup>

$$E = \int_0^{t_E} I \, dt$$

---

† Asterisks denote complex conjugates

$$\begin{aligned}
&= \int_0^{t_E} |R + S|^2 dt \\
&= \int_0^{t_E} (RR^* + SS^* + RS^* + R^*S) dt \\
&= \int_0^{t_E} (rr^* + ss^* + rs^* + r^*s) dt \tag{A.2}
\end{aligned}$$

Notice that the integrand is independent of time so that it can be taken outside the integral sign. This would not be true if the object were moving during the exposure time; a case which is discussed in Section A.2.3. Integrating equation (A.2) under the assumption stated above results in

$$E = (rr^* + ss^* + rs^* + r^*s)t_E \tag{A.3}$$

Inspection of equation (A.3) suggests that the film is exposed in a fashion having no immediate resemblance to the object. That this is the case is evidenced by Figure A.2 which shows an area of a hologram magnified 1000 times.

The dark areas are regions where the function

$$(rr^* + ss^* + rs^* + r^*s)t_E$$

attains maximum values (i.e., reference beam and scene beam are in phase and constructively interfere thereby exposing the film). Conversely, the light areas denote positions where the reference beam and scene beam are 180° out of phase. No image of the object can be discerned.

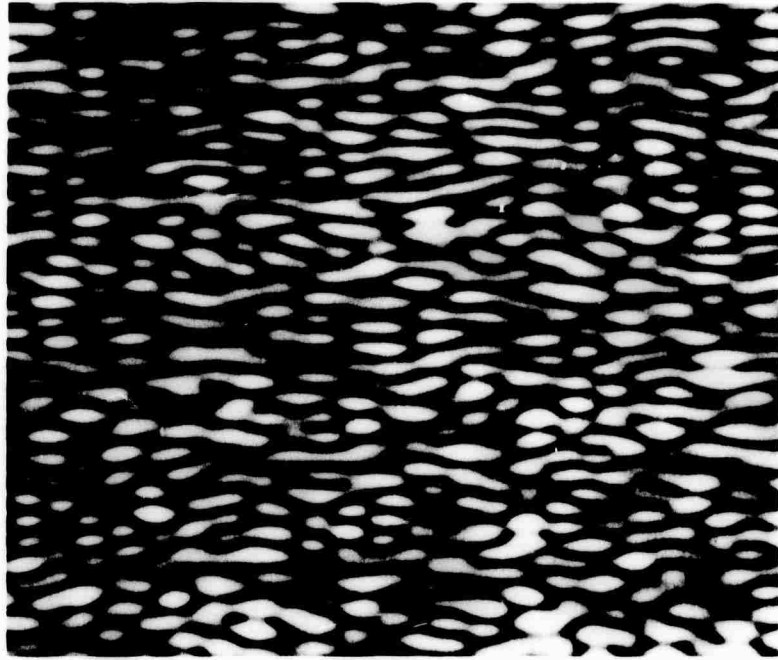


Figure A.2: Photograph of a small area of a hologram magnified 1000 times original

The image is retrieved by illuminating the developed transparency (termed the hologram) with light from a laser at approximately the same angle the reference beam made with the hologram during the recording phase as shown in Figure A.3.

The fraction of light transmitted through the hologram is given by

$$T = (1 - kE)$$

where  $k$  is a constant which depends on the characteristics of the film used. Illuminating the hologram with a reference beam identical to the recording reference beam yields the transmitted amplitude,

$$\begin{aligned} RT &= R(1 - kE) \\ &= R - kRE \end{aligned} \tag{A.4}$$

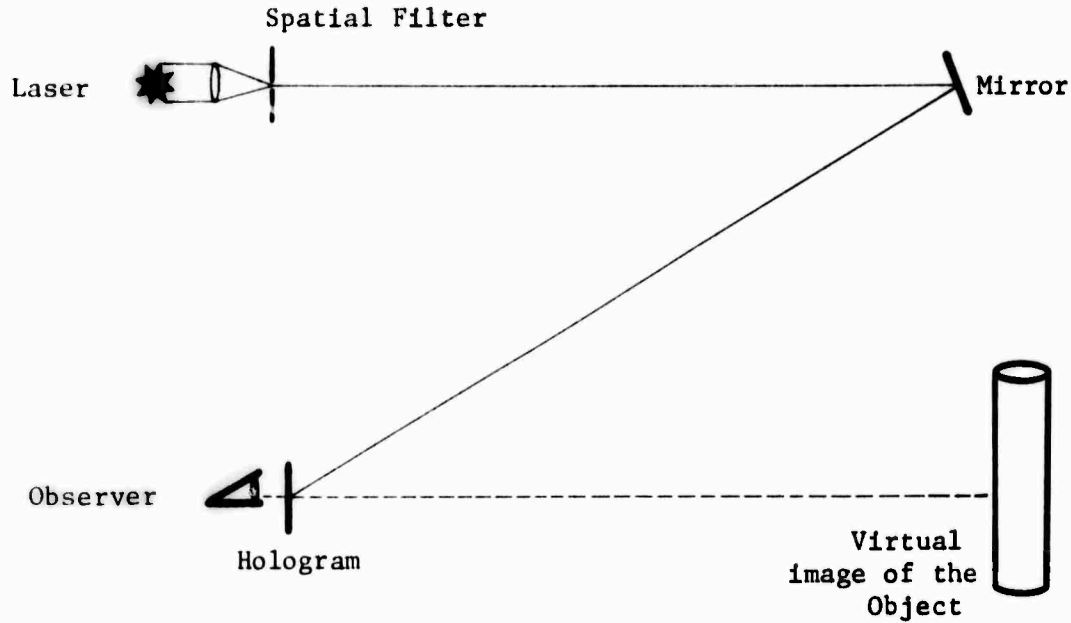


Figure A.3: Image Retrieval Process

For unit exposure time, i.e.,  $t_E = 1$ ,

$$RT = R - k [(rr^* + ss^*)R + rs^*R + Rr^*s]$$

Since the last term  $Rr^*s = re^{i\omega t}r^*s = rr^*se^{i\omega t} = rr^*S$ , we obtain

$$RT = [1 - k(rr^* + ss^*)]R - krs^*R - krr^*S \quad (A.5)$$

For our discussion only the last term,  $-krr^*S$ , is meaningful. Careful inspection of this term shows that it represents the original amplitude of the scene beam,  $S$ , altered in amplitude and phase by the multiplicative factor  $-krr^*$ . This suggests that the three-dimensionality of the image is preserved. The intensity of this reconstructed image is then given by

$$I_o = |-krr^*S|^2 \quad (A.6)$$

or 
$$I_o = k^2 |r|^4 |s|^2 \quad (A.7)$$



The other two terms  $[1 - k(rr^* + ss^*)]R$  and  $-krs^*R$  represent in the first case a transmitted reference beam and in the second a conjugate object beam which comprises the real image of the object.

#### A.2.2 Holographic Interferometry

A holographic interferogram is made by superimposing the three-dimensional recorded image with either a second image recorded on the same film or the actual object. If the object has been slightly deformed for the second image, a pattern of fringes will appear which will map out the contour of the deformation. There are numerous techniques for employing holography to measure displacements. Three techniques which have been used during this program are discussed below.

##### A.2.2.1 Double-Exposure Interferometry

Suppose a hologram was made of an object having a scene beam amplitude,  $S_1$ . If the object is strained and a second exposure made corresponding to scene beam amplitude,  $S_2$ , on the same (yet undeveloped) hologram, then upon reconstruction, two virtual images will be seen when viewing through the hologram. Their composite amplitude is given by

$$A = -krr^* (S_1 + S_2) \quad (A.8)$$

These two scene beams will interfere with one another constructively or destructively, depending on their relative phase. Areas of destructive interference will cause fringes (absence of light). The intensity of the composite image,  $I_r$ , is given by

$$\begin{aligned} I_r &= |-krr^*(S_1 + S_2)|^2 \\ &= (krr^*)^2 (S_1 + S_2)(S_1^* + S_2^*) \end{aligned} \quad (A.9)$$

The two scene beam amplitudes,  $S_1$  and  $S_2$ , can be related by simple geometry. Let  $\ell_1 + \ell_2$  be the path length of light taken by the scene beam when exposing the film to the unstrained object. Similarly,  $\ell'_1 + \ell'_2$  is the path length of the scene beam when the second exposure is made. Then, referring to the following Figure A.4,

$$\ell'^2_1 = \ell^2_1 + m^2 - 2m\ell_1 \cos \theta_1$$

$$\ell'^2_2 = \ell^2_2 + m^2 - 2m\ell_2 \cos \theta_2$$

Solving for  $\ell'_1$  and  $\ell'_2$ ,

$$\ell'_1 = \ell_1 \left[ 1 + \left( \frac{m}{\ell_1} \right)^2 - \frac{2m}{\ell_1} \cos \theta_1 \right]^{1/2} \simeq \ell_1 \left( 1 - \frac{m}{\ell_1} \cos \theta_1 \right) \quad \text{for } \frac{m}{\ell_1} \ll 1$$

$$\ell'_2 = \ell_2 \left[ 1 + \left( \frac{m}{\ell_2} \right)^2 - \frac{2m}{\ell_2} \cos \theta_2 \right]^{1/2} \simeq \ell_2 \left( 1 - \frac{m}{\ell_2} \cos \theta_2 \right) \quad \text{for } \frac{m}{\ell_2} \ll 1$$

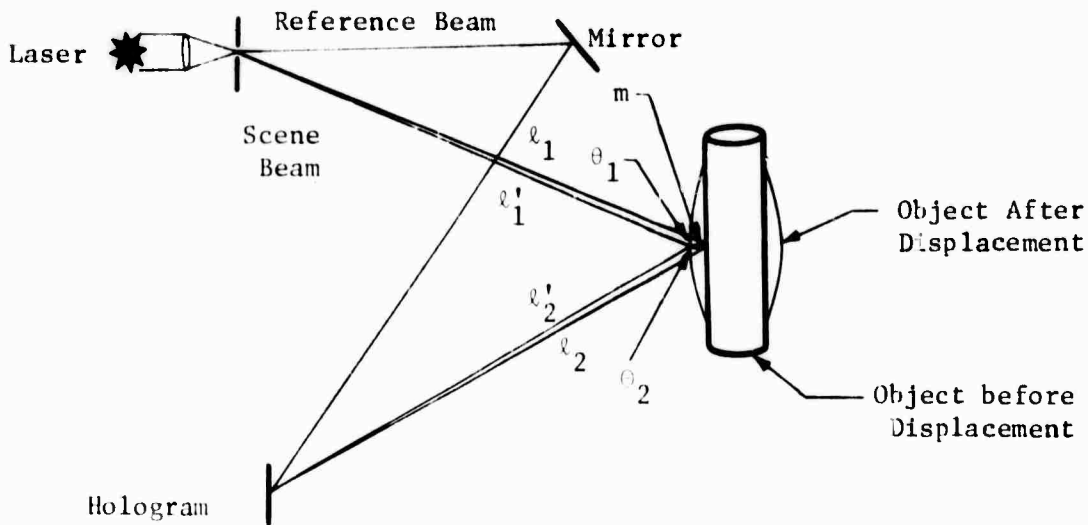


Figure A.4: Phase change of light due to the motion of the object

Solving for pathlength change due to motion results in

$$\ell'_1 - \ell_1 = -m \cos \theta_1 \quad \text{or} \quad \ell_1 - \ell'_1 = m \cos \theta_1$$

$$\ell'_2 - \ell_2 = -m \cos \theta_2 \quad \ell_2 - \ell'_2 = m \cos \theta_2$$

$$\begin{aligned} \text{Total pathlength change } \Delta L &= (\ell_1 + \ell_2) - (\ell'_1 + \ell'_2) \\ &= m(\cos \theta_1 + \cos \theta_2) \end{aligned}$$

The difference in phase is given by

$$\Delta\phi = \frac{2\pi}{\lambda} \Delta L = \frac{2\pi}{\lambda} m(\cos \theta_1 + \cos \theta_2) \quad (\text{A.10})$$

The scene beam,  $S_1$ , during the first exposure is given by

$$S_1 = s e^{i\phi}$$

and the scene beam,  $S_2$ , during the second exposure is given by

$$S_2 = s e^{i(\phi + \Delta\phi)} \quad (\text{A.11})$$

$$S_2 = S_1 e^{\frac{2\pi i}{\lambda} m(\cos \theta_1 + \cos \theta_2)} \quad (\text{A.12})$$

Then equation (A.9) becomes

$$\begin{aligned} I_r &= (krr^*)^2 S_1 S_1^* \left| 1 + e^{\frac{2\pi i}{\lambda} m(\cos \theta_1 + \cos \theta_2)} \right|^2 \\ &= (krr^*)^2 |s|^2 \left[ 2 + 2 \cos \left( \frac{2\pi}{\lambda} m(\cos \theta_1 + \cos \theta_2) \right) \right] \\ &= 2k^2 |r|^4 |s|^2 \left[ 1 + \cos \left( \frac{2\pi}{\lambda} m(\cos \theta_1 + \cos \theta_2) \right) \right] \quad (\text{A.13}) \end{aligned}$$

Note that the intensity given by equation (A.13) has zeros indicating the presence of fringes, namely, when

$$1 + \cos \left( \frac{2\pi}{\lambda} m (\cos \theta_1 + \cos \theta_2) \right) = 0 \quad (\text{A.14})$$

or

$$\frac{2\pi}{\lambda} (\cos \theta_1 + \cos \theta_2) m = (2n - 1)\pi \quad n = 1, 2, 3, \dots$$

or

$$m = \frac{2n - 1}{2(\cos \theta_1 + \cos \theta_2)} \lambda \quad (\text{A.15})$$

If  $\theta_1 = \theta_2 = 0$ , that is, normal incidence and reflection of the illuminating light and normal displacement, then

$$m = \frac{2n - 1}{4} \lambda \quad (\text{A.16})$$

This says that a fringe will be formed whenever the body moves an odd number of quarter wavelengths between exposures.

The first exposure (reference exposure) of a double-exposure hologram is usually made with the object at rest. The second exposure is made after the object has been disturbed. The timing of the second exposure is adjusted according to the particular experiment. As the object should not move more than  $\lambda/2$  during the exposure, most experiments require that the exposure be very short. The pulsed ruby laser is ideal for this purpose producing a light pulse having a duration on the order of 50 nanoseconds, fast enough to "stop" most events. The developed hologram is a frozen fringe interferogram which can be viewed by reconstructing with a continuous wave laser.

Figure A.5 shows an experimental arrangement to measure the propagation of transverse bending waves in an aluminum beam. The beam was loaded by impact with a spherical pendulum on the back (unexposed) surface. The

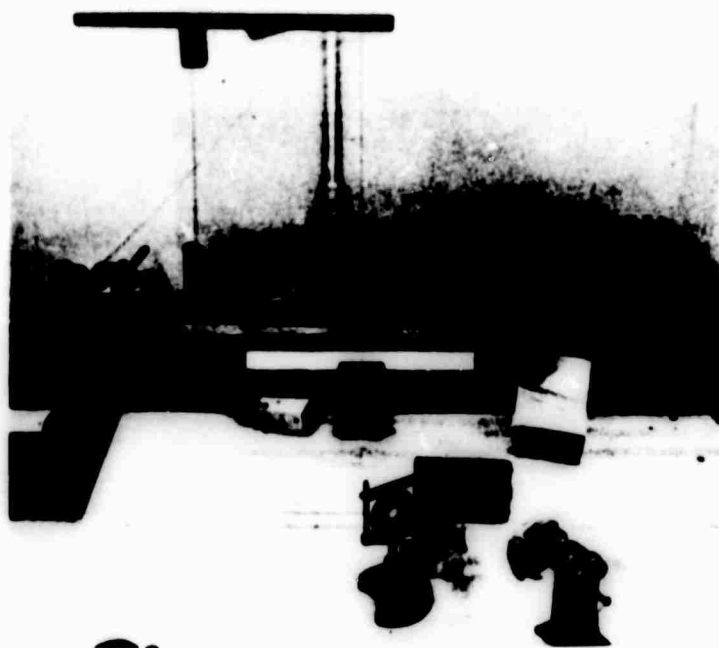
laser triggering circuit was timed to make the second exposure at various times after the initial impact. Figure A.5 also shows the resulting interference pattern at 12.5, 25.0 and 50.0  $\mu\text{sec}$  after impact. The displacement after each of the times is shown on the right of Figure A.5. The measured displacements are in good agreement with those calculated from beam theory.

#### A.2.2.2 Stored Beam Interferometry

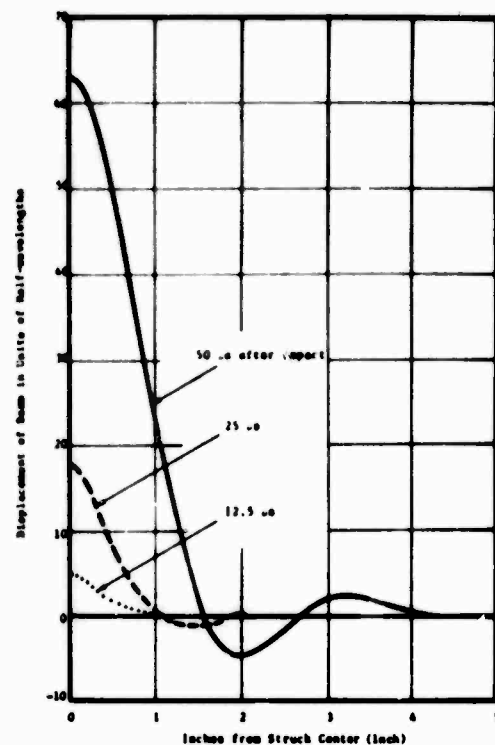
A single exposure of the undisturbed object is made for a stored beam interferogram. After developing the photographic plate containing the hologram, it is carefully replaced into the same position it assumed during the exposure. When looking through the hologram at the object, an observer will see two images superimposed. One is due to the interaction of the reference beam with the hologram forming the reconstructed image and the second being the object itself. These two images interfere with one another producing fringes. The mathematical discussion is essentially the same as that given in Section A.2.2.2. This stored beam method differs from the double-exposure method in that the displacement fringes are produced in real-time. Dynamic events can be observed or recorded as they occur provided that they are slow enough to be detected.

#### A.2.2.3 Time Averaged Holographic Interferometry

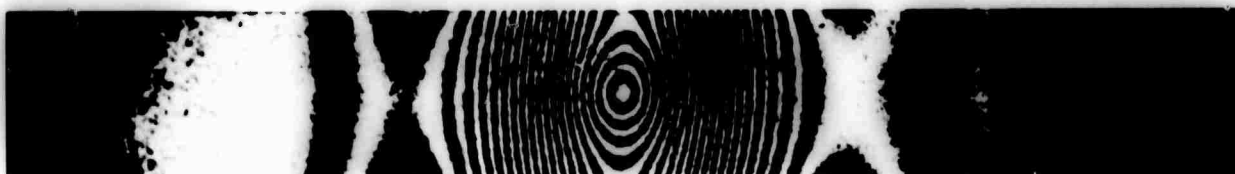
A time averaged interferogram is made when the surface of the object moves a significant amount ( $\gg \lambda/2$ ) during the exposure of the hologram. This may be considered a generalization of multiple-exposure interferometry to the case where the moving object is continuously exposed, i.e., the film gets exposed to light from the object in each position the object assumes during the exposure. Referring back to Section A.1, the film is exposed according to equation A.2.



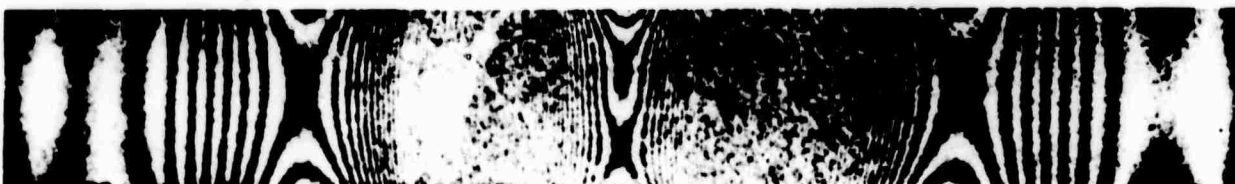
EXPERIMENTAL SET-UP



12.5 microseconds



25.0 microseconds



50.0 microseconds

Figure A5: Three double exposure holographic interferograms of a transverse wave propagating in a prismatic beam

$$E = \int_0^{t_E} (RR^* + SS^* + RS^* + R^*S) dt$$

Considering only the last term, since it alone contributes to the holographic virtual image, we get

$$\begin{aligned} E &= r^*s \int_0^{t_E} e^{-i\omega t + i\omega t + i\Delta\phi} dt \\ &= r^*s \int_0^{t_E} e^{i\Delta\phi} dt \end{aligned} \quad (A.17)$$

where  $\Delta\phi$  is the change in phase due to the motion.

Suppose that the velocity of the surface is given by  $v$ . Then, as in equation (A.10),

$$\begin{aligned} \Delta\phi &= \frac{2\pi}{\lambda} L = \frac{2\pi}{\lambda} (\cos\theta_1 + \cos\theta_2)v \\ E &= r^*s \int_0^{t_E} e^{\frac{2\pi i}{\lambda} (\cos\theta_1 + \cos\theta_2)vt} dt \end{aligned}$$

The intensity of the reconstructed image is given by

$$\begin{aligned} I_r &\sim \left| \int_0^{t_E} e^{i \frac{2\pi}{\lambda} (\cos\theta_1 + \cos\theta_2)vt} dt \right|^2 \\ &= \left| \frac{e^{i \frac{2\pi}{\lambda} (\cos\theta_1 + \cos\theta_2)vt}}{i \frac{2\pi}{\lambda} (\cos\theta_1 + \cos\theta_2)v} \right|_0^{t_E} \\ &= \left| \frac{\lambda}{2\pi i (\cos\theta_1 + \cos\theta_2)v} \right|^2 \left| \frac{12\pi}{\lambda} (\cos\theta_1 + \cos\theta_2)vt_{E-1} \right|^2 \end{aligned}$$

$$\begin{aligned}
&= 2 \left| \frac{\lambda}{2\pi i (\cos \theta_1 + \cos \theta_2) v} \right|^2 \left[ 1 - \cos \left( \frac{2\pi}{\lambda} (\cos \theta_1 + \cos \theta_2) v t_E \right) \right] \\
&= \left( \frac{\lambda}{\pi (\cos \theta_1 + \cos \theta_2) v} \right)^2 \sin^2 \left( \frac{\pi}{\lambda} (\cos \theta_1 + \cos \theta_2) v t_E \right) \quad (A.18)
\end{aligned}$$

Note that this function has zeros (an indication of fringes) whenever

$$\frac{\pi}{\lambda} (\cos \theta_1 + \cos \theta_2) v t_E = n\pi \quad n = 1, 2, \dots$$

This suggests that areas of the object which move with a velocity

$$v = \frac{n\lambda}{(\cos \theta_1 + \cos \theta_2) t_E}$$

will be covered with a fringe. To get a feeling for the velocities, assume a ruby laser ( $\lambda = 6943\text{\AA}$ ) is used to expose the subject for 50 nsec, and  $\theta_1 \approx \theta_2 \approx 0$ .

Then

$$v = \frac{n \cdot 6943 \times 10^{-8}}{2 \times 50 \times 10^{-9}} = 694.3 \text{ n } \frac{\text{cm}}{\text{sec}}$$

$$v \approx .0007 \text{ n cm}/\mu\text{sec} \quad n = 1, 2, 3, \dots$$

A more convenient way of expressing this condition may be in terms of displacement during the exposure, (ie) resulting in

$$\begin{aligned}
v t_E &= \frac{n\lambda}{\cos \theta_1 + \cos \theta_2} \\
&= \frac{n\lambda}{2} \quad \text{for } \theta_1 \approx \theta_2 \approx 0.
\end{aligned}$$



This equation says that if a particle moves at constant velocity an integral number of half-wavelengths during an exposure, it will be covered by a fringe. The general relationship between the intensity,  $I_r$ , versus the velocity is shown schematically in Figure A.6 below.

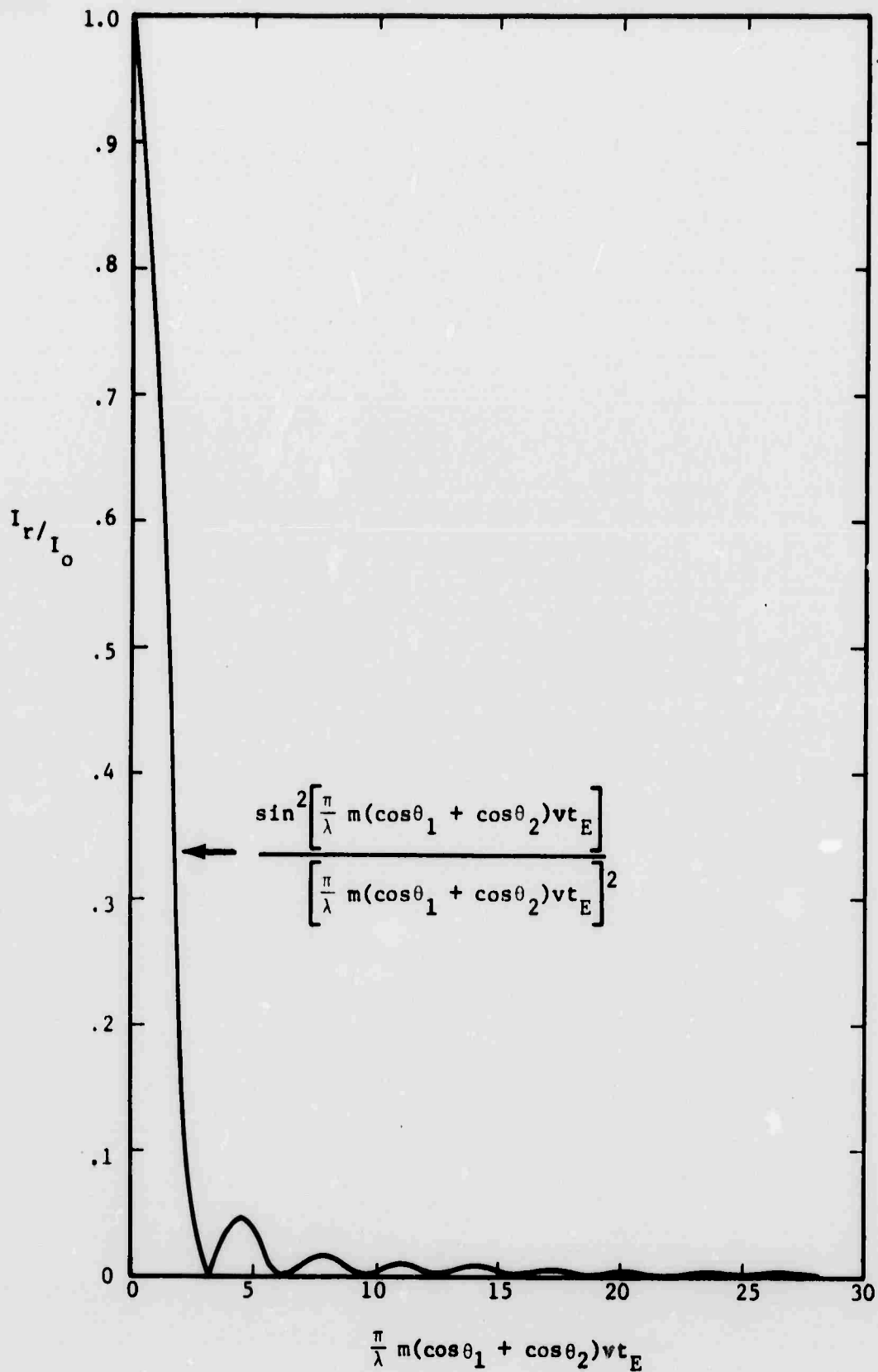


Figure A.6: Intensity of the Holographically Reconstructed Image taken of a Moving object

## APPENDIX B

### B.0 Multiframe Recording Technique

TRW Systems has developed a multiframe recording technique which can be used to measure dynamic strain fields in rock samples at a series of closely spaced time intervals using a multipulse ruby laser. The ruby laser used in this technique has the capability of producing up to four coherent pulses with variable time spacings. The use of electro-optic beam switching eliminates the need for mechanically moving or shuttering the film and thus makes it practical to make several holograms or interferograms in rapid succession. One property of a hologram is that image reconstruction is possible only when it is illuminated by a coherent light source at nearly the same angle assumed by the reference beam during the recording process. (See Appendix A for a discussion of holography). This property allows multiple holograms or interferograms to be recorded on a single piece of film simply by using a different reference beam angle for each one.

To produce reference beams at different angles and in rapid succession, use is made of Pockels Cells, calcite prisms and the intrinsic polarization of light from the ruby laser. A Pockels cell is a device which rotates the plane of polarization of transmitted light when a voltage is applied to it. The light is transmitted without alteration when no voltage is applied. A calcite prism changes the direction of transmitted light according to its polarization, i.e., light of vertical polarization is transmitted undisturbed whereas light of horizontal polarization is deflected by some angle  $\alpha$ . An illustration of these concepts is shown in Figure B.1.

Using conventional equipment, the switching required for this operation can be accomplished in nanoseconds, between two successive laser pulses. Figure B.2 shows schematically an experimental arrangement by which two interferograms can be made in rapid succession of a single dynamic event.

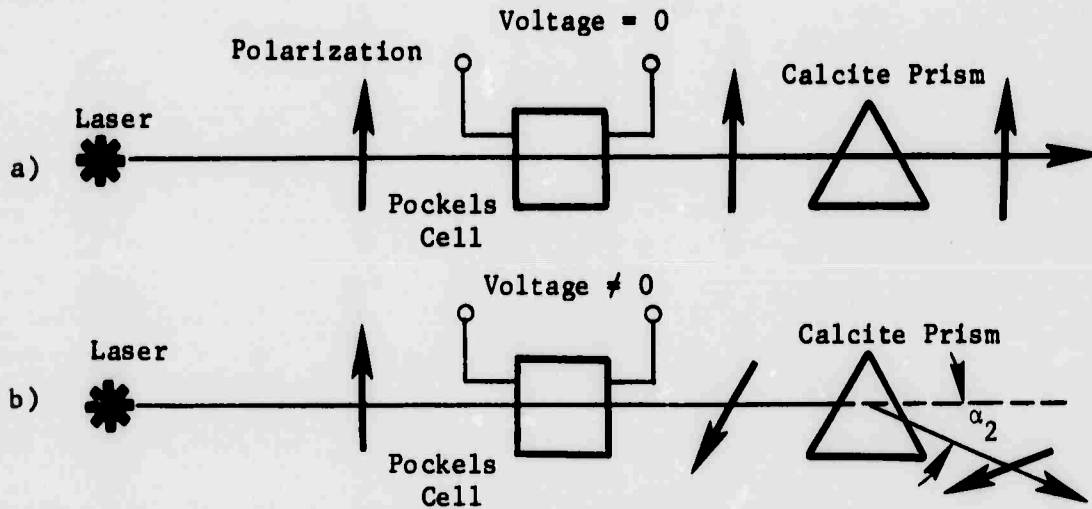


Figure B.1: Changing the Direction of a Light Beam with a Pockels Cell - Calcite Prism Combination  
(a) No voltage across Pockels Cell  
(b) Voltage applied across Pockels Cell

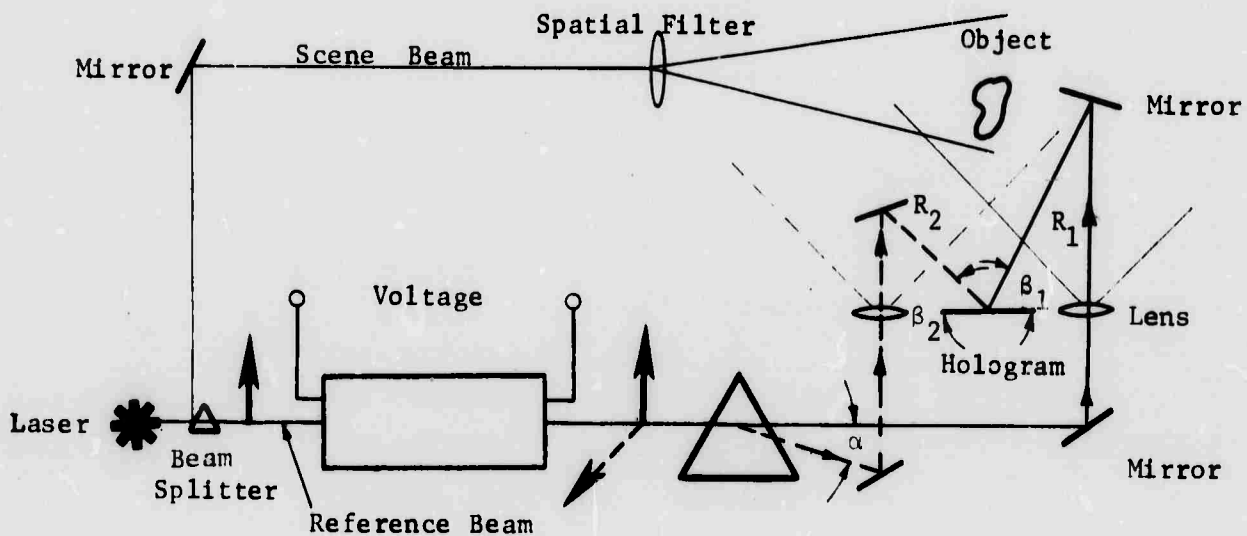


Figure B.2: One Possible Arrangement to Make Two Interferograms of an Event in Rapid Succession

The hologram exposed in this way can be developed and viewed with conventional continuous wave lasers as shown schematically in Figure B3.

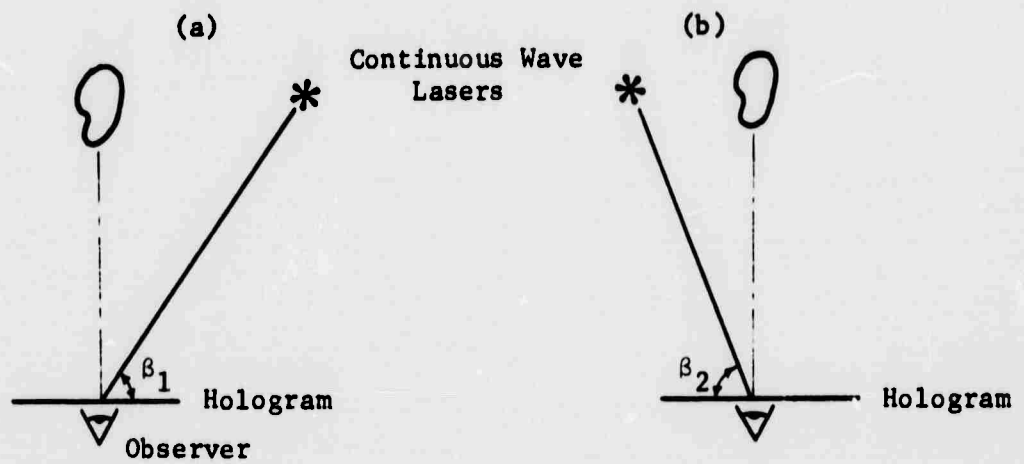


Figure B3: Reconstruction of Two Interferograms Made on the Same Hologram.

- (a) First interferogram reconstruction
- (b) Second interferogram reconstruction